Spin-Dependent Processes in Organic Devices

Dissertation to obtain the academic degree

Dr. rer. nat.

submitted to the Departement of Physics of Freie Universität Berlin by:

Sebastian Schaefer

Berlin, 2010

Betreuer: Dr. Wolfgang Harneit

1. Gutachter: Prof. Dr. R. Bittl

2. Gutachterin: Prof. Dr. M. Ch. Lux-Steiner

Tag der Disputation: 2. Juni 2010

Abstract

By bringing together a systematic IV-characterization and EDMR experiments, transport and degradation processes were studied in organic devices. In a first step, two Zinc phthalocyanine (ZnPc) single layer devices with different electrodes were investigated, a coplanar Au/ZnPc/Au sample and a sandwich type ITO/ZnPc/Al device. They served as a testbed for the correlation of IV- and EDMR measurements. The insights gained in this study were then applied to more complex bilayer ZnPc/C_{60}-heterojunction solar cells.

A transport study at low voltages shows that bulk transport with Ohmic IV characteristics is dominant in the coplanar ZnPc, whereas the transport in the sandwich device is controled by a Schottky barrier at the aluminum contact. Both samples show SCL-currents with exponential trap distribution in the high voltage limit, characteristic for ZnPc. The degradation analysis indicate that the ITO/ZnPc/Al - device suffers from oxidation of the aluminum electrode, exhibiting a pronounced Schottky emission IV-behavior. This degradation could be prevented by an effective encapsulation, using a glass cover and UV-glue. The results of the solar cells also indicate an oxygen-induced degradation. This degradation is related to an increase of the resistivity in the C_{60} layer, due to oxygen impurities.

The EDMR measurements indicate that polaron recombination is the dominant process in the organic devices investigated in this work. However the recombination process shows distinct impact on the electric transport in the individual devices. Whereas the EDMR signal is photocurrent quenching in the coplanar sample it reverses sign in the sandwich device. The results of the transport measurements indicate a charge accumulation at the oxidized ZnPc/Al contact. As a consequence a model was proposed in which recombination involving these accumulated carriers can lead to a current enhancement. This model was verified by voltage dependent EDMR measurements, where it consistently explains a sign reversal when changing from negative to positive bias.

In degraded solar cells a similar charge accumulation as in the ZnPc-layer is suspected. This charge accumulation manifests itself in an EDMR signal with identical properties to the one in ZnPc and is assumed to happen at the ZnPc/C_{60}- interface, during degradation. Furthermore, EDMR studies indicate that spin-dependent recombination happens during the exciton dissociation process at the ZnPc/C_{60} - interface, in the charged transfer complex ($ZnPc^{+}$, C_{60}^{-}). This process is observed to quench the photocurrent in the solar cells.

In further spin studies Rabi beat oscillations under spin-locking conditions were observed for the first time in the EDMR of ZnPc and solar cells. This phenomenon exhibits a signal oscillation at twice the Rabi-frequency that appears only when two pair spins are excited at the same time. The impact of this beat oscillation on EDMR lineshapes as well as its microwave power dependence were studied in detail. The effect of exchange coupling in the spin-pair was analyzed in the context of the beat oscillations and a lock in phase analysis.

Contents

1 Theoretical Background **11**
- 1.1 Charge Transport in Organic Materials . . . 11
  - 1.1.1 Space Charge Limited Currents (SCLC) . . . 12
  - 1.1.2 SCLC in the Presence of Defect States . . . 13
- 1.2 Metal-Semiconductor Contacts . . . 14
  - 1.2.1 Schottky Contact . . . 14
  - 1.2.2 Fermi-Level Pinning . . . 16
- 1.3 Electron Spin Resonance (ESR) . . . 17
- 1.4 Electrically Detected Magnetic Resonance (EDMR) . . . 18
  - 1.4.1 EDMR in Organic Semiconductor Devices . . . 19
  - 1.4.2 Exchange Coupling in EDMR . . . 20
- 1.5 Pulsed Electrically Detected Magnetic Resonance . . . 22
  - 1.5.1 Transient EDMR Signal . . . 22
  - 1.5.2 Rabi Oscillation . . . 26

2 Experimental Background **33**
- 2.1 Organic Materials . . . 33
  - 2.1.1 Fullerene C_{60} . . . 33
  - 2.1.2 Phthalocyanine . . . 36
- 2.2 EPR in ZnPc . . . 39
  - 2.2.1 ZnPc Radical Cation g-Value determined by EPR . . . 39
- 2.3 Device Fabrication . . . 41
  - 2.3.1 Coplanar Au/ZnPc/Au Samples . . . 42
  - 2.3.2 Sandwich Devices for EDMR . . . 43
  - 2.3.3 Sandwich Devices for IV-Characteristics . . . 44
- 2.4 Experimental Setup . . . 45
  - 2.4.1 IV-Glovebox-Setup . . . 45
  - 2.4.2 EDMR Setup . . . 45

3 Charge Transport in Phthalocyanine Devices 47
3.1 Bulk Transport in Au/ZnPc/Au Coplanar Devices 47
3.1.1 IV-Temperature Dependency 48
3.2 ITO/ZnPc/AL Schottky-Solar Cells 50
3.2.1 IV-Characteristics (injection vs bulk properties) 50
3.2.2 Degradation of the Al Contact Interface 56
3.2.3 Encapsulation Revisited 60
3.2.4 Discussion and Conclusions 62

4 Spin Dependent Transport in ZnPc 65
4.1 Bulk Transport vs. Injection Limited Transport 65
4.1.1 EDMR in Coplanar Au/ZnPc/Au Devices 65
4.1.2 EDMR in ITO/ZnPc/Al Sandwich Devices 67
4.2 EDMR Signal Saturation 70
4.3 EDMR at Different Voltages 70
4.4 The Role of Exchange Coupling in ZnPc 72
4.4.1 Discussion of The Lineshapes 73
4.4.2 Lock-In Phase Analysis 75
4.5 Magnetoresistance in ZnPc 78

5 Spin Dynamics in ZnPc 83
5.1 Pulsed EDMR in ZnPc Layers 83
5.2 The Phenomenon of Spin-Locking 86
5.2.1 Line Shapes Under Spin-Locking Conditions 89
5.2.2 Beat Oscillations at different MW-Powers 89
5.3 Pulsed EDMR in Au/ZnPc/Au Coplanar Devices 90
5.3.1 Decoherence in Au/ZnPc/Au devices 92
5.4 Discussion and Conclusions 94

6 Spin-Dependent Transport in ZnPc/C_{60} Solar Cells 95
6.1 IV-Characteristics of Solar1new 95
6.2 Spin Dependent Processes in Bilayer Cells 98
6.2.1 Continuous Wave EDMR 98
6.2.2 Discussion 99
6.2.3 Pulsed EDMR in ZnPc/C_{60}-Solar Cells 100
6.2.4 Discussion 101
6.3 Signal Decomposition by Light Intensity Control 102
6.3.1 IV-Characteristic of Solar2new 102
6.3.2 Pulsed EDMR Results for Solar2new 103

6.3.3 EDMR Light Intensity Dependence 106
6.4 Rabi Beat Oscillations 108
6.5 Rabi Beat Oscillations of the Quenching Signal 112

7 Summary and Outlook 115

Preface

In past years the potential of organic materials for optoelectronic devices and spintronic applications has gained more and more attention. The extremely high absorption coefficients of some organic molecules facilitate the fabrication of low cost thin film photo-detectors and solar cells, whereas organic light emitting diodes (OLEDs) are already used in commercial displays and illuminants. Preparation methods of organic materials like spin coating and vapor jet printing pave the way for flexible devices like roll up displays.

Beside applications in conventional electronics, the observation of a giant magneto resistance (GMR) effect in organic spin valves [1] provides a route to organic spintronics. The underlying mechanism of the magnetoresistance effect in organic materials differs significantly from the classical picture and is a highly debated topic in current research. Although much efforts have been done in this field, the microscopic mechanisms in organic magnetoresistance as well as in magnetic resonance related methods (EDMR, ODMR, ELDMR, ...) are still unclear. A better understanding of these microscopic processes would not only have impact on the field of spintronics and their applications, but could also help to identify current limiting processes and degradation mechanisms in conventional organic devices. Since the most serious drawbacks in organic solar cells are still the low efficiency and the long term stability, the analysis of degradation and transport limitations is crucial for gaining a better device performance.

As a consequence, this work concentrates on the identification of transport limitations in organic thin film devices by a continuous wave and pulsed EDMR study. The approach combines a fundamental current voltage study with a detailed EDMR analysis in zinc phthalocyanine (ZnPc) and ZnPc/C_{60}-solar cells. The enhanced sensitivity of EDMR in comparison to the conventional EPR makes this method an appropriate tool for the characterization of spin-dependent processes in thin film devices under realistic conditions such as white light illumination and room temperature. Since the limiting processes in organic samples are very complex, the study starts with simple one layer devices and progresses to more sophisticated bilayer solar cells. This approach offers the possibility to apply the results from the single layers ZnPc and from previous EDMR experiments on C_{60} [2, 3, 4] to the bilayer solar cell, which facilitates the identification of the EDMR signals significantly.

Beside the influences of interfaces and electrode materials, also the effect of degradation on the device performance and the EDMR signal is examined. In the detailed pulsed EDMR analysis Rabi beat oscillations of non selectively excited spin pairs will be presented for the first time in EDMR of organics. This effect manifests itself in a signal oscillation at twice the Rabi frequency, when the two spins of a pair are excited at the same time. This phenomenon was previously observed in the reaction yield detected magnetic resonance (RYDMR) of radical pairs. Furthermore the influence of exchange coupling will be investigated with the help of a phase analysis in cw EDMR .

Chapter 1 introduces the main transport mechanisms and semiconductor-metal-interface models which are needed in this work. This is followed by an overview of continuous wave and pulsed EDMR theory, which will be discussed in the frame of spin-dependent recombination. The EDMR section contains also the influence of exchange coupling on the cw-spectrum and the consequences of selective and non selective excitation in pulsed experiments.

Chapter 2 gives a short review about the electrical and optical properties of the organic materials ZnPc and C_{60}. The results from previous EDMR measurements on C_{60} will be discussed and for ZnPc the g-value of the radical cation is determined by ESR measurements of iodine doped material which is helpful for the following EDMR study. Futhermore experimental details about device fabrication and measurement setups are given.

Chapter 3 is a transport and degradation analysis on ZnPc single layer devices. The effect of different contact materials and geometries on the transport is studied in ZnPc thin film structures. The results obtained on two representative device structures are discussed throughout the next chapters, a coplanar Au/ZnPc/Au device and an ITO/ZnPc/Al sandwich device. With the help of a current voltage analysis it can be shown which contacts provide bulk- or injection limited transport in ZnPc. The temperature and thickness dependence of the IV-measurements is used to characterize the influence of bulk transport and metal-semiconductor interfaces on the charge transport. Further experiments concentrate on degradation mechanisms in the sandwich device and how this degradation can be prevented by an effective encapsulation.

Chapter 4 presents continuous wave EDMR experiments on coplanar and sandwich type devices. Whereas the EDMR signal is first analyzed in the coplanar device, further studies on the sandwich type ITO/ZnPc/Al sample treat the influence of the electrodes and the degradation on the EDMR signal. The spin-dependent processes is embedded in the transport model developed in chapter 3 to give a complete picture of the working device including loss mechanisms. This transport model is further supported by saturation and voltage dependent EDMR measurements, providing a more detailed view of the spin-dependent process. The influence of exchange coupling on the EDMR spectrum is discussed in the coplanar ZnPc device and analyzed with a lock-in phase analysis. The last section is concerned with magnetoresitance observed in the coplanar ZnPc sample. The results were interpreted in terms of the spin-dependent recombination model used in the EDMR, bridging the gap between magnetoresistance and EDMR.

Chapter 5 treats the spin dynamics in the ZnPc single layer devices by means of a pulsed EDMR study. In the first section the pulsed EDMR spectrum is analyzed and compared to cw EDMR spectra. Beside this analysis, Rabi oscillations in the case of selective and non selective excitation are discussed in the following sections and compared to theoretical predictions. This treatment includes the microwave power dependence of the Rabi beat oscillations and a lineshape analysis of pulsed EDMR spectra at pulse lengths shorter than the dephasing time. Furthermore the spin-dynamics are compared to the spin-locking phenomenon observed in radical pairs.

Chapter 6 presents results obtained on ZnPc/C_{60} bilayer solar cells. Including a brief IV-characterization, the chapter begins with the analysis of the continuous wave and pulsed EDMR spectra at different voltages in the context of the previous measurements on the single layer ZnPc and C_{60} devices [2, 3, 4]. This part of the chapter deals with the identification of the EDMR signals and discusses possible loss mechanisms and degradation in these devices. Further pulsed studies demonstrate how EDMR signals can be extracted by their distinct photocurrent response on the light intensity. This is followed by a detailed analysis of spectrally resolved Rabi oscillations and a comparison between the spin dynamics of the signals.

Chapter 1

Theoretical Background

The following sections are intended to give the reader a short introduction into the theoretical framework of this work. The main transport mechanisms in organic semiconductors and the most important semiconductor-metal-interface models are presented in first sections. Since it provides the basics for the EDMR, the principles of Electron spin resonance (ESR) will be illustrated shortly afterwards. The following EDMR section treats the influence of exchange coupling on the spin level transitions and thus the cw-spectrum, whereas the last part of this chapter is concerned with the coherent spin motion in pulsed EDMR. This part explains how selective and non selective excitation influence the Rabi-oscillation of the spin pair ensemble.

1.1 Charge Transport in Organic Materials

Whereas charge transport pathways in inorganic semiconductors are provided by a bandstructure due to strong exchange interactions of atomic orbitals in the crystal structure, organic solids are bound together by relatively weak Van der Waals - or π - π - interactions, which is rather inappropriate for electron transport. The weak bonding forces lead to intermolecular separations that are large compared to the separation of atoms and ions in inorganic crystal lattices. Consequently, the overlap of the molecular orbitals is rather weak, which leads to lower mobilities than in inorganic semiconductors. However, since many organic molecules consist of delocalized electrons, the intramolecular electron exchange can be still substantial, especially in aromatic ring structures. As a result, the mobility of an electron residing on an individual molecule is very large compared to the mobility of electrons that move from one molecule to another, while traversing the molecular crystal. Another consequence of the weak intermolecular forces is that the properties of a molecular crystal are primarily determined by the electronic properties of the molecules itself, which is in contrast to inorganic semiconductors. The small overlap of the molecular orbitals inhibits the formation of extended energy bands. The energy band width depends on the spacing of the molecules, in which a large molecular spacing leads to narrow energy bands. If the energy band width is smaller or in the range of k$_B$T, the molecular distances become too large for the electrons to tunnel from one molecule to another. In this case charge transport is often described by a hopping process, where the electrons have to overcome the potential barrier ΔE_J between the molecules. The hopping propability is [5]:

$$W_H = \nu_J exp\left(-\frac{\Delta E_J}{k_B T}\right) \tag{1.1}$$

The attempt frequency ν_J of the hopping depends on the exchange energy J, which can be determined from EPR measurements. As condition for hopping transport, the carrier mobility should be smaller than $\mu \approx 1 cm^2 V^{-1} s^{-1}$[5, 6]. However, since in many organic solids the mobilities are in the order of $\mu \approx 1 cm^2 V^{-1} s^{-1}$ it is difficult to decide a priori which transport model is appropriate. The low conductivities in organic materials can be overcome by doping, which was first demonstrated by Shikarawa et al. [7]. They showed that the conductivity of polyacetylene increased by several orders of magnitude upon doping by halogen (seven orders in the case of iodine doping). Furthermore extremely high absorption coefficients allow the production of very thin absorber layers in organic photodetectors and solar cells.

1.1.1 Space Charge Limited Currents (SCLC)

Space charge limited currents (SCLC) appear when the concentration of injected charge carriers exceeds the concentration of thermally generated carriers. Efficient carrier injection requires at least one ohmic contact to the organic layer, which provides a reservoir of charges. At low voltages, the concentration of injected carriers is rather low and the current is usually dominated by thermally generated carriers. This results in an Ohmic current density-voltage behavior:

$$J = p_0 e \mu \frac{V}{d} \tag{1.2}$$

where p_0 is the concentration of thermally generated holes (assuming a hole conductor), e is the elementary charge and d is the spacing of the electrodes. When higher voltages are applied, in a way that the concentration of injected carriers becomes higher than the thermally generated ones, SCL currents will dominate the device. The organic layer is now treated as a perfect insulator between two electrodes, a situation similar to a parallel plate capacitor with charge Q given by:

$$Q = CV \qquad \text{with} \qquad C = \varepsilon_0 \varepsilon_r \frac{A}{d} \tag{1.3}$$

where ε_0 is the vacuum permittivity, ε_r the dielectric constant of the organic layer and C is the capacitance with plate area A and plate spacing d. Since in the case of carrier injection the charges do not reside on the plates, but distribute in the organic layer, the effective separation of the charge is not the plate distance d but a smaller value. The correct value of d will be included in the exact formula, calculated by Mark and Lampert [8]. If the injected space charge Q drifts through the insulator with a transit time t_{trans} this leads to a current density:

$$J_{SCLC} \propto \frac{Q}{At_{trans}} \tag{1.4}$$

Inserting Eq.1.3 into Eq.1.4 leads to the following expression for the current density:

$$J_{SCLC} \propto \frac{\varepsilon_0 \varepsilon_r V}{dt_{trans}} \tag{1.5}$$

The transit time is given by $t_{trans} = d/v$, where v is the speed of the carriers, which depends on their drift mobility μ and the external voltage V as: $v = \mu V/d$. Plugging the transit time $t_{trans} = d^2/\mu V$ into Eq.1.5 yields:

$$J_{SCLC} \propto \varepsilon_0 \varepsilon_r \mu \frac{V^2}{d^3} \tag{1.6}$$

The exact formula for the space charge limited currents including the correct charge distribution in the insulator is given by [8]:

$$J_{SCLC} = \frac{9}{8} \varepsilon_0 \varepsilon_r \mu \frac{V^2}{d^3} \tag{1.7}$$

The formula is called Child's law and was derived for ideal trap free insulators.

1.1.2 SCLC in the Presence of Defect States

When traps are present in the organic layer only a part of the injected carriers may contribute to the current, whereas the other carriers are trapped. Consequently, Eq.1.7 has to be modified. However, the modification depends on the distribution of the trap states in the band gap. In several organic materials the traps exhibit an exponential distribution $N_t(E)$ with respect to the valence band edge:

$$N_t(E) = N_0 exp\left(-\frac{E}{k_B T_C}\right) \tag{1.8}$$

where $N_t(E)$ is the trap density per unit energy and unit volume, which decreases with the distance E from the valence band edge. N_0 is the trap density at the valence band edge and T_C is a parameter that characterizes the width of the distribution (usually $T_C > T$ at room temperature). If the traps in a sample show such a distribution, the current density can be expressed by a power law of the form:

$$J_{SCLC} = e\mu N_v \left(\frac{\varepsilon_o \varepsilon_r}{eN_0 k_B T_C}\right)^l \frac{V^{l+1}}{d^{2l+1}} \tag{1.9}$$

where N_v is the effective density of states in the valence band and l is a parameter that is given by:

$$l = \frac{T_C}{T} \tag{1.10}$$

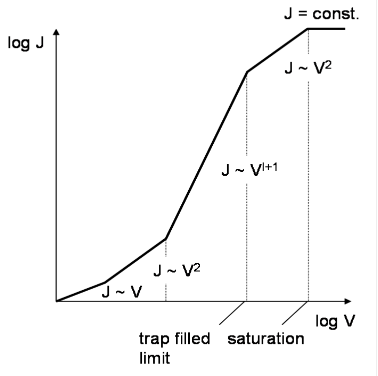

Figure 1.1: *SCL current voltage characteristics of devices with exponential trap distribution.*

The IV-characteristics in a device with exponential trap distribution is illustrated in Fig.1.1. At low voltages, where thermally generated carriers dominate the device current, an Ohmic IV-dependence is observed. As soon as the concentration of injected carriers exceeds that of thermally generated ones the current depends quadratically on the voltage. If the voltage is further increased, the Fermi-level shifts far into the trap band and the IV-characteristics become superquadratic. In the limiting case where all traps are filled, the IV-relation returns to the quadratic behavior until finally the current may saturate.

1.2 Metal-Semiconductor Contacts

1.2.1 Schottky Contact

If a p- or n-type semiconductor is brought into contact with a metal, either an Ohmic or a rectifying contact is formed. Which of the two contacts is observed in an ideal metal-semiconductor junction depends on the workfunction of the metal and the semiconductor. A rectifying contact is known as a Schottky barrier and arises when the workfunction ϕ_S of a p-type semiconductor is larger than the workfunction ϕ_M of the metal, see Fig.1.2 a). If the materials are brought into contact, electrons flow from the metal into the semiconductor until the Fermi-levels of the metal E_F^M and the semiconductor E_F^S equalize each other. As the electrons move from the metal into the semiconductor, they recombine with free holes in the valence band of the semiconductor. As a result, the interface region of the semiconductor gets depleted of free holes leaving behind the negatively charged ionized acceptors. On the metal side, a thin layer of positive charges is formed within the Thomas-Fermi screening distance ($\approx$ 0.5 Å) from the interface. The low concentration of free holes in the semiconductor leads to an increased distance between the Fermi level E_F^S and the valence band E_V^S near the interface. Since in thermal equilibrium the Fermi level remains constant throughout the semiconductor, the valence band edge bends down at the interface as shown in Fig.1.2 b). However, in the bulk of the semiconductor distant from the metal contact the Fermi level position does not

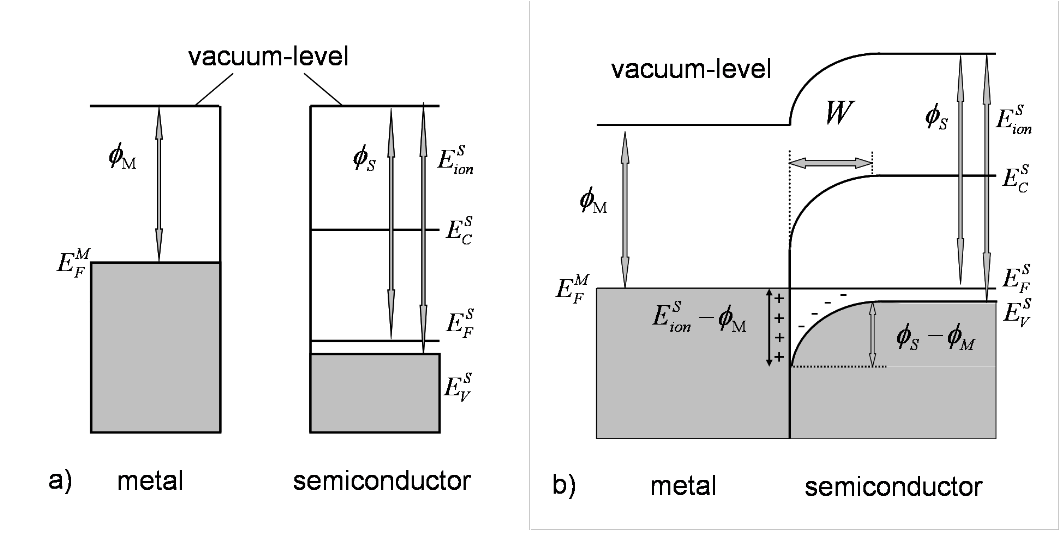

Figure 1.2: *Formation of a Schottky barrier between a metal and a p-type semiconductor. a) before contact b) in contact.*

change and the band diagram is the same as in Fig.1.2 a). The amount of bend-bending is given by the difference in the workfunctions of the metal and the semiconductor and is also known as the built in potential or the contact potential:

$$eV_{bi} = \phi_S - \phi_M \tag{1.11}$$

The contact potential has to be surpassed when holes enter the metal from the semiconductor side. On the other hand, when holes move from the metal into the semiconductor they have to surpass the Schottky barrier given by:

$$eV_B = E^S_{ion} - \phi_M \tag{1.12}$$

where E^S_{ion} is the ionization energy of the semiconductor, defined by the distance of the valence band edge to the vacuum energy. The shape of the barrier is determined by the acceptor distribution in the semiconductor. A uniform acceptor distribution gives rise to a parabolic barrier, known as the Schottky barrier, whereas the concentration of acceptors in the semiconductor N_A controls the width of the depletion zone:

$$W = \sqrt{\frac{2\varepsilon_0\varepsilon_r V_{bi}}{eN_A}} \tag{1.13}$$

If a voltage is applied to the Schottky junction with the metal positively biased (reverse bias), hole injection from the metal into the semiconductor is hindered by the Schottky barrier V_B. The situation is illustrated in Fig.1.3 a) and shows that under these conditions the width of the depletion zone in the semiconductor increases. The resulting current flow is very weak. In

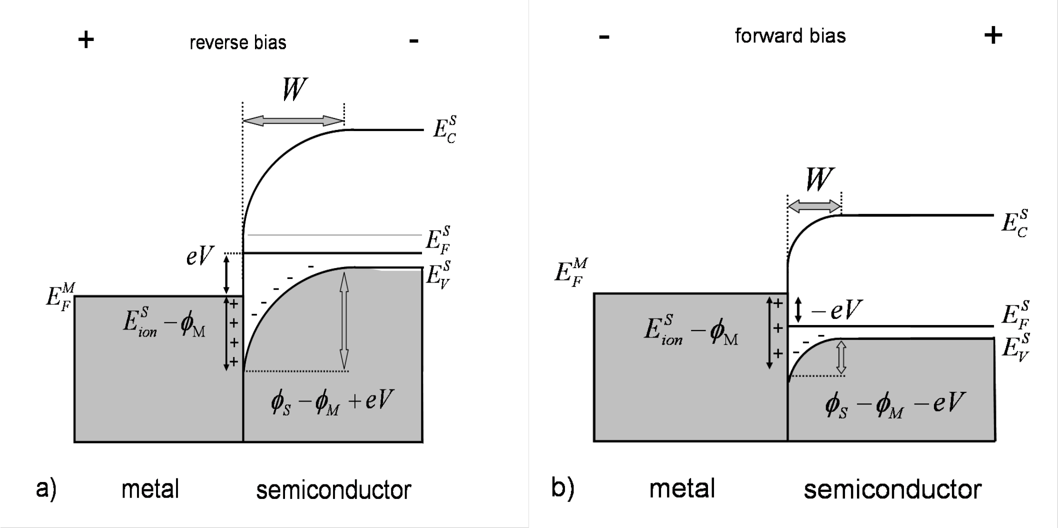

Figure 1.3: *Schottky barrier under reverse a) and forward bias conditions b)*

forward bias, the holes moving from the semiconductor into the metal have to surpass only the reduced contact potential $V_{bi} - V$. Fig.1.3 b) shows that the width of the depletion zone decreases in forward bias, which promotes current flow in this direction. Different mechanisms like tunneling and recombination can control the current across a Schottky barrier in forward bias. However the most important one is thermionic emission over the barrier, where only those holes that have an energy greater than $e(V_{bi} - V)$ may surpass the barrier. The current flow controlled by thermionic emission over the barrier is given by the Shockley equation:

$$J = J_0 \left[exp\left(\frac{eV}{nk_BT} \right) - 1 \right] \tag{1.14}$$

$$J_0 = A^* T^2 exp\left[-\frac{eV_B}{k_BT} \right] \tag{1.15}$$

where $A^* = 4\pi e m^* k_B^2 / h$ is the effective Richardson constant, m^* is the effective mass and h is Planck's constant. The diode quality factor n describes the deviation from the ideal thermionic emission current and indicates that other transport mechanisms are present in the sample.

1.2.2 Fermi-Level Pinning

Practical experience shows that barriers at semiconductor-metal junctions often show weaker dependence on the metal workfunction ϕ_M than predicted by the Schottky theory. This weak correlation between the barrier height and the metal workfunction may arise when localized surface states are present in the semiconductor. These surface states can stem from imperfections at the surface of the crystal structure, especially in covalently bounded semiconductors, were dangling bond give rise to defect levels in the band gap. However Fermi-level pinning was suggested also for C_{60} fullerene -layers [9]. After a model of Bardeen [10] the surface

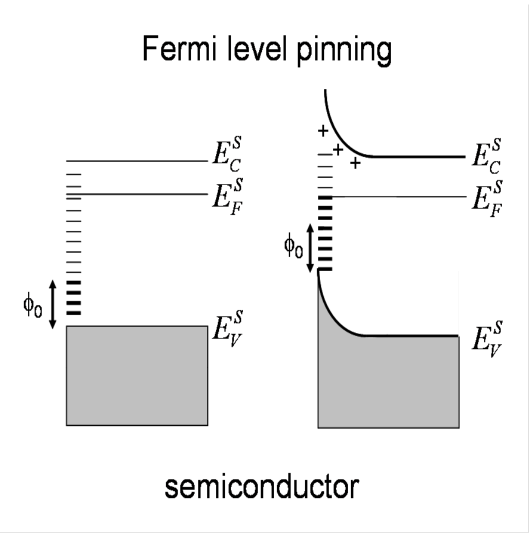

Figure 1.4: *Fermi-level pinning scheme.*

states are distributed continuously in the bandgap and have neutral level ϕ_0, see Fig.1.4. All surface levels below ϕ_0 are occupied and act like donor levels, which means that they are neutral when occupied but positive when empty. The surface levels above the neutral level are acceptor like and become negative when they are occupied. In order to reach equilibrium, electrons move from the semiconductor into the surface states until the Fermi-level at the surface and in the bulk material are aligned. The result is a positively charged depletion zone in the semiconductor and a negatively charged surface. The band bending leads to the formation of a surface barrier even without contact to a metal. If the semiconductor is brought into contact with a metal, carriers are exchanged between the metal and the surface states without strongly effecting the barrier. In this case the Fermi level is said to be pinned.

1.3 Electron Spin Resonance (ESR)

Transitions between electronic states with different quantum numbers m_s can be detected by electron spin resonance. Since the quantum number m_s determines the orientation of the electron spin with respect to an external magnetic field B_0, a change in m_s is equivalent to a change in the direction of the spin. In order to describe the interaction of the spin with the external magnetic field it is necessary to introduce the magnetic moment of the electron spin:

$$\mu_s = \sqrt{s(s+1)}\mu_B g \tag{1.16}$$

where s is the spin quantum number, μ_B is the Bohr magneton and g is the Landé factor. In the presence of a magnetic field B_0 the component of the magnetic moment parallel (antiparallel) to this field is given by:

$$\mu_{sz} = \mp \frac{1}{2} g \mu_B \tag{1.17}$$

Since the potential energy of the magnetic moment in the external field is $E = -\overrightarrow{\mu} \cdot \overrightarrow{B}$ the transition energy between the corresponding sublevels is:

$$\Delta E = g \mu_B B_0 \tag{1.18}$$

If the paramagnetic sample is exposed to radiation with a frequency ν, transitions between the spin sublevels may be induced if the condition:

$$h\nu = g \mu_B B_0 \tag{1.19}$$

is fulfilled. In ESR the absorption of radiation by the sample is detected. Experimental practice shows that in most cases it is convenient to use a constant microwave frequency and measure the absorption as a function of the magnetic field B_0.

1.4 Electrically Detected Magnetic Resonance (EDMR)

Introduction

Electron spin resonance (ESR) is a well known method to characterize charge carriers, defects and impurities in solids. This has been demonstrated for example in amorphous silicon (a-Si:H) where the silicon dangling bond defect was identified by means of ESR [11, 12]. However, the sensitivity of conventional ESR is limited to a number of $\sim 10^{11}$ spins per Gauss line width [13], which is too low to investigate for example interfaces in thin film devices. An appropriate experimental method for detailed studies of microscopic transport and loss mechanisms should be able to identify transport processes with a sensitivity many orders of magnitude higher than ESR. This can be achieved by replacing the conventional detection of the microwave absorption by an electrical detection setup. As a result, not only the sensitivity is enhanced but also the object of investigation changes. In an EDMR experiment the conductivity of a device changes, while sweeping the magnetic field through resonance in the presence of microwave irradiation. The reason for the conductivity changes are spin-dependent processes like recombination, hopping or tunneling. This is in contrast to ESR which is not sensitive to processes but to paramagnetic species. Consequently EDMR is able to identify microscopic transport mechanisms as long as they depend on spin selection rules. Most of the early models describing the conductivity changes under ESR rely on spin-dependent recombination mechanism investigated in silicon devices [14, 15, 16, 17, 18]. Basically the recombination of two charge carriers depends on their relative spin orientation and is only permitted when the spins point in opposite directions, also called singlet configuration (S = 0). This follows from the conservation of the angular momentum, if the ground state of the recombining pair is also assumed to be a singlet state. Magnetic resonance increases the number of singlet spin pairs in the sample and therefore leads to an enhancement of the recombination rate. The early theory of spin-dependent recombination, introduced by D. J. Lépine [14] is based on the polarization of the spin ensemble. In this model free carriers recombine at recombination centers. The spin lattice relaxation is assumed to be faster than the recombination and in thermal equilibrium there will be an enhanced population of triplet states due to the polarization. Applying electron paramagnetic resonance to the sample tends to equalize the population of all spin sublevels which leads to a ratio of 1/4 : 3/4 for singlet to triplet states. Since the polarization is rather weak at room temperature $p \approx g\mu_B B_0/k_B T \approx 10^{-3}$ the expected EDMR signal strength is also very weak $\Delta\sigma/\sigma \approx p^2 \approx 10^{-6}$. This is in contrast to various experimental results, that show larger EDMR signals [19, 20, 21], and therefore cannot hold for those systems. The Kaplan-Solomon-Mott (KSM) model [15] is based on the assumption that localized electrons and holes form an intermediate pair state with considerable lifetime before they dissociate or recombine spin-dependently. In contrast to the model of Lépine it requires the recombination to be faster than the spin lattice relaxation. As a result the system cannot get into thermal equilibrium and a high amount of pairs with triplet spin configuration will accumulate in the sample. Since this model is not based on the weak thermal polarization at room temperature, higher signal strength are predicted that are in agreement with the experimental results. Further investigations in silicon based semiconductors revealed various other spin-dependent mechanisms, such as hopping and tunneling, summarized in a survey of M. Stutzmann et. al [13].

1.4.1 EDMR in Organic Semiconductor Devices

Reports about EDMR measurements with continuous microwave irradiation can be found for small molecules [20, 21, 22, 23, 24] as well as for polymer devices [24, 25, 26, 27]. The most frequently used models to explain the EDMR signals in organic materials are spin-dependent polaron recombination and bipolaron formation. Bipolarons are assumed to be spinless particles (S = 0) that consist of two like charged polarons. The binding energy of the bipolarons is assumed to stem from the polarization of the lattice [28]. If the attractive interaction of the two polarons with the polarized dielectric medium exceeds the repulsive coulomb interaction this may lead to a bound bipolaron. Furthermore, the formation of bipolarons is possible only when the precursor polarons have a singlet spin configuration and is therefore spin-dependent. As far as polaron pair recombination is concerned, we want to follow the polaron reencounter model, introduced by T. Eickelkamp et al. [21]. This model derives from the radical pair recombination model and considers different g-factors for the negative and positive polarons as well as spin-spin-interactions within the pair. After light excitation excitons are generated in organic semiconductor that dissociate into free polarons. These polarons may reencounter in the organic semiconductor and form non geminate polaron pairs with random spin configuration. As in the KSM model it is assumes that the polarons form a long living intermediate pair state prior to the recombination process. In general the outcome of recombination and bipolaron formation is a current quenching, but for different reasons. The result of enhanced recombination under magnetic resonance is the annihilation of an electron and a hole. Since both carriers can in principle contribute to the current if the spin pair dissociates, the elimination of them leads to a reduction of charge carrier concentration and the current decreases. The enhanced formation of bipolarons in magnetic resonance is also assumed to decrease the current since bipolarons are less mobile carriers than polarons. However under specific circumstances both mechanisms may lead also to a current enhancement, this will be discussed in the experimental section.

1.4.2 Exchange Coupling in EDMR

In the absence of spin-spin-coupling an EDMR-spectrum is assumed to comprise the two spectral features of the precursor spin pair. However, exchange coupling within the pair leads to four energy level with four allowed transitions. The effect of the exchange coupling to the spectral lines becomes apparent from the Spin-Hamiltonian containing the Zeeman interaction of both spins and an expression for the exchange interaction between them:

$$\frac{\hat{H}}{\hbar} = \frac{\hat{H}^Z + \hat{H}^J}{\hbar} = \omega_a S_{az} + \omega_b S_{bz} - J \mathbf{S_a} \cdot \mathbf{S_b} \tag{1.20}$$

where $\omega_{a,b}$ are the Larmor frequencies of spins a and b of the pair, $S_{az,bz}$ are the z-components of the spinoperators $\mathbf{S_{a,b}}$ and J is the exchange coupling constant. In this analysis, the dipolar coupling within the spin pair and hyperfine interactions are neglected. The spin eigenstates in the pure Zeeman basis according to $\hat{H}^Z$ can be denoted as: $|\uparrow\uparrow\rangle, |\uparrow\downarrow\rangle, |\downarrow\uparrow\rangle, |\downarrow\downarrow\rangle$ in the product space of the spins a and b: $|\uparrow\uparrow\rangle = |\uparrow\rangle_a \otimes |\uparrow\rangle_b$. The corresponding energy level are given by:

$$\begin{aligned} E_1^Z &= \frac{\hbar}{2}(\omega_a + \omega_b) \\ E_2^Z &= \frac{\hbar}{2}(\omega_a - \omega_b) \\ E_3^Z &= -\frac{\hbar}{2}(\omega_a - \omega_b) \\ E_4^Z &= -\frac{\hbar}{2}(\omega_a + \omega_b) \end{aligned} \tag{1.21}$$

and the transitions are simply the Larmor frequencies of the two spins, see also Fig.1.5 b). However, in the Zeeman basis the Hamiltonian in Eq.1.20 is not diagonal and thus the spin basis has to be transformed to diagonalize the Hamiltonian. The transformed spin basis reads:

$$\begin{aligned}|1\rangle &= |\uparrow\uparrow\rangle\\ |2\rangle &= \cos\varphi\,|\uparrow\downarrow\rangle-\sin\varphi\,|\downarrow\uparrow\rangle\\ |3\rangle &= \sin\varphi\,|\uparrow\downarrow\rangle+\cos\varphi\,|\downarrow\uparrow\rangle\\ |4\rangle &= |\downarrow\downarrow\rangle\end{aligned} \tag{1.22}$$

with $\tan(2\varphi) = {}^{J}/_{\delta\omega}$ and $\delta\omega = \omega_a - \omega_b$. The states $|2\rangle$ and $|3\rangle$ are mixed states with singlet content, where recombination is partially allowed, whereas the pure triplet level $|1\rangle$ and $|4\rangle$, also denoted by $|T_+\rangle$ and $|T_-\rangle$ respectively, inhibit recombination. In the case of strong coupling $J \gg \delta\omega$ ($\varphi = \pi/4$) eigenstate $|2\rangle$ becomes a pure singlet state $|S\rangle = \frac{1}{\sqrt{2}}(|\uparrow\downarrow\rangle - |\downarrow\uparrow\rangle)$, whereas eigenstate $|3\rangle$ becomes a triplet state $|T_0\rangle = \frac{1}{\sqrt{2}}(|\uparrow\downarrow\rangle + |\downarrow\uparrow\rangle)$. The energy levels according to the new spin states are now a function of the exchange coupling constant:

$$\begin{aligned}E_1 &= \hbar(\omega_0-\frac{J}{4})\\ E_2 &= \hbar(\frac{J}{4}+\frac{\Omega_J}{2})\\ E_3 &= \hbar(\frac{J}{4}-\frac{\Omega_J}{2})\\ E_4 &= \hbar(-\omega_0-\frac{J}{4})\end{aligned} \tag{1.23}$$

where $\omega_0 = (\omega_a + \omega_b)/2$, and $\Omega_J = \sqrt{\delta\omega^2 + J^2}$. As a result of the shifted energy levels the partial degeneracy of the four transition lines is lifted and the corresponding transitions between these four spin states are given by:

$$\begin{aligned}\Delta E_{1-2} &= E_1-E_2=\hbar(\omega_0-\frac{J}{2}-\frac{\Omega_J}{2})\\ \Delta E_{1-3} &= E_1-E_3=\hbar(\omega_0-\frac{J}{2}+\frac{\Omega_J}{2})\\ \Delta E_{2-4} &= E_2-E_4=\hbar(\omega_0+\frac{J}{2}+\frac{\Omega_J}{2})\\ \Delta E_{3-4} &= E_3-E_4=\hbar(\omega_0+\frac{J}{2}-\frac{\Omega_J}{2})\end{aligned} \tag{1.24}$$

In general four lines will appear in the spectrum. However, if the coupling constant J becomes significantly larger than the Larmor separation $\delta\omega$, the transitions ΔE_{1-3} and ΔE_{3-4} (indicated by the grey arrows in the level scheme of Fig.1.5 a)) tend towards each other. For $J \gg \delta\omega$ and $\Omega_J \approx J$ the transitions become one center line and two satellites separated by J:

$$\Delta E_{1-3} = \Delta E_{3-4} = \hbar\omega_0, \qquad \Delta E_{1-2} = \hbar(\omega_0 - J), \qquad \Delta E_{2-4} = \hbar(\omega_0 + J) \tag{1.25}$$

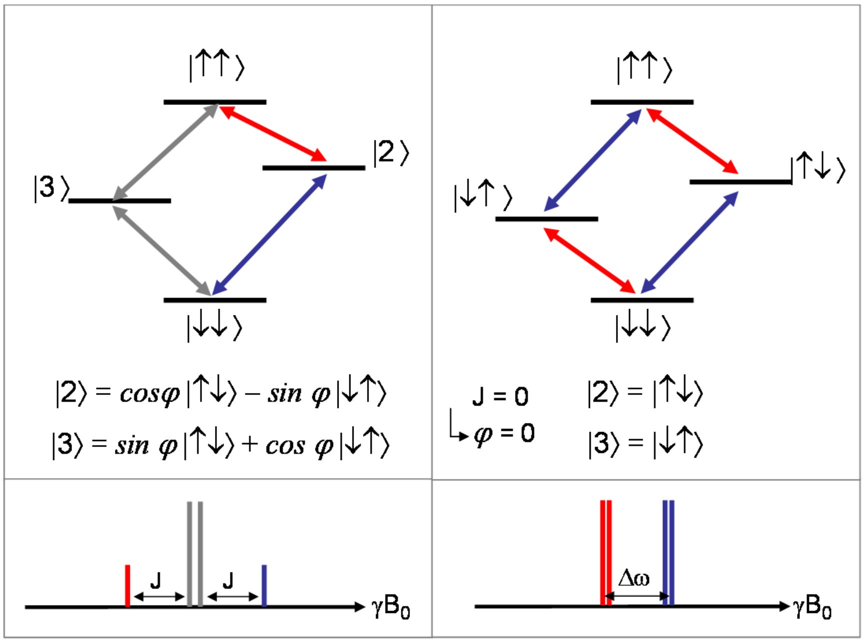

Figure 1.5: *Energy level and spin-states in the exchange coupled spin pair (left) and without exchange coupling (right) with the correlated stick spectra indicated below.*

The transition probability of the center lines increase relative to the satellites with increasing J, which becomes apparent from the expression for the transition strength $\omega_1^{jk} = |\langle j|H_1/\hbar|k\rangle|$:

$$\begin{aligned} \omega_1^{(12)} &= \omega_1^{(24)} = \omega_1\sqrt{1-sin2\varphi} \\ \omega_1^{(13)} &= \omega_1^{(34)} = \omega_1\sqrt{1+sin2\varphi} \end{aligned} \tag{1.26}$$

where $H_1/\hbar = \omega_1(S_{xa}+S_{xb})$ is the microwave Hamiltonian in the rotating frame in angular frequency units. In Fig.1.5 the energy levels and transitions (arrows) of the spin pair are illustrated in the case of exchange coupling a) and without b). The resulting spectral features are shown in the stick spectrum below. In general, strong exchange coupling leads the triplet system $|T_+\rangle, |T_0\rangle, |T_-\rangle$ to decouple from the singlet state $|S\rangle$. As aresult the transition rate between the triplet and the singlet system is very weak, resulting in a weak or even absent EDMR signal. The effect of exchange coupling on the EDMR spectrum will be discussed in § 4.4.

1.5 Pulsed Electrically Detected Magnetic Resonance

1.5.1 Transient EDMR Signal

The theoretical treatment of pulsed EDMR will be discussed in the framework of spin-dependent recombination, as proposed by C. Boehme and K. Lips [29, 30]. The recombination mechanism assumed by Boehme and Lips includes trapped electrons in a deep lying level center in the bandgap of a semiconductor, whereas this work will focus on spin-dependent recombination of oppositely charged polaron pairs as assumed in the polaron reencounter model, introduced by T. Eickelkamp [21]. As mentioned in the previous sections the recombination rate r depends on the spin configuration of the spin pair and is assumed to be much higher for a singlet state, than for a triplet configuration ($r_S \gg r_T$). In general the spin pair is in one of the the four spin states given in Eq.1.22. Whereas states $|1\rangle$ and $|4\rangle$ are pure triplet states that decay with r_T , the recombination rate of the mixed spin states $|2\rangle$ and $|3\rangle$ can be determined by taking into account the singlet and triplet content of the states:

$$r_i = r_S \left|\langle i|S\rangle\right|^2 + r_T \left|\langle i|T_0\rangle\right|^2, \quad i = 2,3 \tag{1.27}$$

where the singlet and the triplet states have been defined previously as $\frac{1}{\sqrt{2}}\left(|\uparrow\downarrow\rangle \mp |\downarrow\uparrow\rangle\right)$. The recombination rates r_{1-4} can be evaluated by plugging the four eigenstates into Eq.1.28 and using the definition $tan(2\varphi) = {}^{J}/_{\delta\omega}$, which yields:

$$\begin{aligned} r_{1,4} &= r_T \\ r_2 &= \frac{r_S}{2}\left(1+\frac{J}{\Omega_J}\right)+\frac{r_T}{2}\left(1-\frac{J}{\Omega_J}\right) \\ r_3 &= \frac{r_S}{2}\left(1-\frac{J}{\Omega_J}\right)+\frac{r_T}{2}\left(1+\frac{J}{\Omega_J}\right) \end{aligned} \tag{1.28}$$

After a pulsed resonant microwave excitation the spin pair ensemble will show a change in the recombination rate with respect to the situation before excitation. This is a result of the change in spin state occupation, due to the microwave induced transitions. In the following the spin state occupation of the pair ensemble is expressed in the density matrix formalism [31], where the diagonal matrix elements $\rho_{ii} = p_i |i\rangle\langle i|$ represent the occupation density in the spin states $|i\rangle$. This is equivalent to the probability p_i to find the ensemble in the state $|i\rangle$. The occupation differences between the diagonal elements characterize the polarization of the ensemble. The off diagonal elements ρ_{ij} of the the density matrix represent the coherence on the transition between state $|i\rangle$ and $|j\rangle$. Applying a pulsed microwave excitation of pulse length τ to the spin ensemble changes the density matrix entries. As a result the total recombination rate is altered which leads to a change in the density of the electrons $\Delta n_e(t,\tau)$ and holes $\Delta n_h(t,\tau)$ in the sample. The conductivity change , given by:

$$\Delta\sigma(t,\tau) = e\left(\Delta n_e(t,\tau)\mu_e + \Delta n_h(t,\tau)\mu_h\right) \tag{1.29}$$

where μ_e and μ_h are the mobilities of the electrons and the holes respectively. If the mobilities of the charge carriers are assumed to be constant the conductivity change originates only from the variation of the electron and hole densities which are influenced by the decay and generation of the precursor spin pairs. Under constant illumination the spin pairs are generated

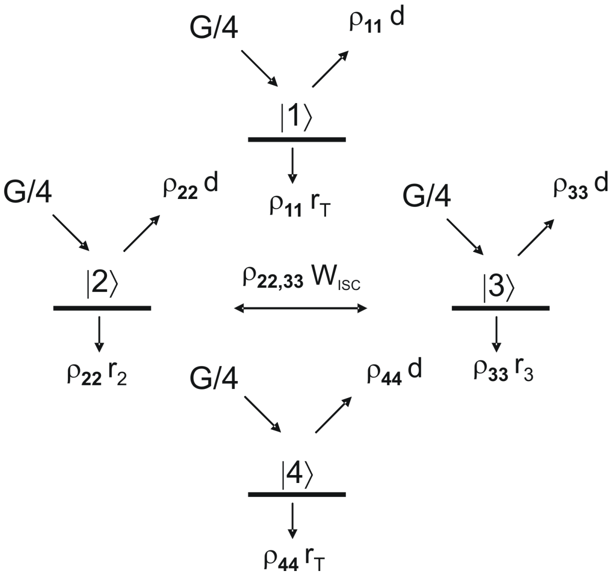

Figure 1.6: *Generation, dissociation, recombination and relaxation rates within the spin pair ensemble in an EDMR experiment.*

by light excitation and it can be assumed that all four spin levels are populated uniformly by the generation rate G/4, as illustrated in Fig.1.6. However, the spin level will be depopulated by recombination and dissociation rates. Since the polaron pairs are localized carriers, the only way they can contribute to the current is by dissociation into free polarons. If we assume a common dissociation rate d for all spin level the charge carrier density change can be expressed by:

$$\Delta n_e(t,\tau) = \Delta n_h(t,\tau) = \tau_L d \sum_{i=1}^{4} (\hat{\rho}_{ii}(t,\tau) - \hat{\rho}_{ii}(\tau)) \tag{1.30}$$

where $\hat{\rho}_{ii}(t,\tau)$ are the diagonal density matrix elements at time t after the state at the end of the microwave pulse $\hat{\rho}_{ii}(\tau)$ and τ_L is the lifetime of the carriers. For simplicity τ_L is assumed the same for electrons and holes. The term $\hat{\rho}_{ii}(t,\tau) - \hat{\rho}_{ii}(\tau)$ represents the transient density matrix changes in the spin pair ensemble due to recombination and dissociation after the pulsed excitation of length τ. Since the coherent density changes during the microwave pulse are much faster than the recombination processes, they will be discussed separately in the following section. Plugging Eq.1.30 into Eq.1.29 yields an expression for the conductivity change:

$$\Delta\sigma(t,\tau) = e\tau_L(\mu_e + \mu_h) d \sum_{i=1,\ldots,4} (\hat{\rho}_{ii}(t,\tau) - \hat{\rho}_{ii}(\tau)) \tag{1.31}$$

Since the time dependency of $\Delta\sigma(t,\tau)$ has its origin in the population changes of the density matrix elements, the time dependency of $(\hat{\rho}_{ii}(t,\tau) - \hat{\rho}_{ii}(\tau))$ has to be expressed in a rate model. This rate model manifests itself in a set of differential equations, according to the rate picture given in Fig.1.6. Each of the four spin pair level will be populated by $\frac{1}{4}$ of the generation rate G and depopulated by the appropriate dissociation and recombination rates, leading to the following expression:

$$\begin{pmatrix} \dot{\rho}_{11} \\ \dot{\rho}_{22} \\ \dot{\rho}_{33} \\ \dot{\rho}_{44} \end{pmatrix} = \begin{pmatrix} -d-r_T & 0 & 0 & 0 \\ 0 & -d-r_2 & 0 & 0 \\ 0 & 0 & -d-r_3 & 0 \\ 0 & 0 & 0 & -d-r_T \end{pmatrix} \begin{pmatrix} \rho_{11} \\ \rho_{22} \\ \rho_{33} \\ \rho_{44} \end{pmatrix} + \frac{G}{4} \begin{pmatrix} 1 \\ 1 \\ 1 \\ 1 \end{pmatrix} \tag{1.32}$$

where the intersystem crossing rate W$_{ISC}$ is neglected here for simplicity. The equilibrium solutions $\dot{\rho}_{ii} = 0$ of this equation yield:

$$\begin{aligned} \rho^{eq}_{11,44} &= \frac{G}{4(d+r_T)} \\ \rho^{eq}_{22,33} &= \frac{G}{4(d+r_{2,3})} \end{aligned} \tag{1.33}$$

The general solutions of the homogeneous part of Eq.1.32 are exponential functions of the form:

$$\begin{aligned} \rho_{11,44}(t,\tau) &= Tr\{\hat{\rho}^{eq}\}\Delta_{11,44}(\tau)e^{-(d+r_T)t} \\ \rho_{22,33}(t,\tau) &= Tr\{\hat{\rho}^{eq}\}\Delta_{22,33}(\tau)e^{-(d+r_{2,3})t} \end{aligned} \tag{1.34}$$

where the amplitudes $\Delta_{ii}(\tau)$ are the microwave induced density changes during a pulsed excitation of length τ. These density changes read:

$$\begin{aligned} \Delta_{11,44}(\tau) &= \frac{\rho_{11,44}(\tau) - \rho^{eq}_{11,44}}{Tr\{\hat{\rho}^{eq}\}} \\ \Delta_{22,33}(\tau) &= \frac{\rho_{22,33}(\tau) - \rho^{eq}_{22,33}}{Tr\{\hat{\rho}^{eq}\}} \end{aligned} \tag{1.35}$$

$$\text{with} \quad \sum_{i=1,\ldots,4} \Delta_{ii}(\tau) = 0 \quad \text{since } Tr\hat{\rho} = Tr\hat{\rho}^{eq}$$

In general the recombination rates r_2 and r_3 are much stronger than the triplet recombination rate r_T and the dissociation rate d. This leads to an overpopulation of the triplet level in the steady state prior to the microwave pulse, which can be expressed by:

$$\hat{\rho}^{eq} \simeq \begin{pmatrix} \frac{G}{4(d+r_T)} & 0 & 0 & 0 \\ 0 & 0 & 0 & 0 \\ 0 & 0 & 0 & 0 \\ 0 & 0 & 0 & \frac{G}{4(d+r_T)} \end{pmatrix} \tag{1.36}$$

As a result the density changes in Eq.1.35 are negative for the triplet states which are depopulated during microwave excitation and positive for the mixed states with singlet content, since their population increases. The density changes are normalized by the trace of $\hat{\rho}^{eq}$: $Tr\{\hat{\rho}^{eq}\} = G/2(d + r_T)$. With these results the general expression for the conductivity changes given in Eq.1.31 can be rewritten in the form:

$$\Delta\sigma(t,\tau) = \frac{e\tau_L(\mu_e + \mu_h)dG}{2(d + r_T)} \left[\Delta_{22}(\tau)e^{-(d+r_2)t} + \Delta_{33}(\tau)e^{-(d+r_3)t} + (\Delta_{11}(\tau) + \Delta_{44}(\tau))e^{-(d+r_T)t}\right] \tag{1.37}$$

In principle $\Delta\sigma(t,\tau)$ is a multi exponential decay with positive components for the singlet states and a negative component for the triplets. The large singlet recombination rates $r_{2,3} \gg r_T$ lead to very fast decay of the positive signal components. In the case where the response time of the setup or the sample is longer than $1/r_{2,3}$, the positive contributions cannot be observed, which is also discussed in the work of Hiromitsu et al [32]. If exchange coupling is weak Eq.1.28 shows that the recombination rates become $r_2 = r_3 = (r_S + r_T)/2$, and Eq.1.35 and 1.37 simplify. In this case the equation for the conductivity change becomes:

$$\Delta\sigma(t,\tau) = \frac{e\tau_L(\mu_e + \mu_h)dG}{2(d + r_T)}(\Delta_{11}(\tau) + \Delta_{44}(\tau)) \left[e^{-(\frac{r_S - r_T}{2})t} - 1\right] e^{-(d+r_T)t} \tag{1.38}$$

Although this expression contains only three parameters (r_S, r_T, d) that determine the transient rise and decay of the signal, in real devices impedances from the electrical setup and the device will be superimposed on the signal. Consequently, the determination of the rate constants is a rather difficult task.

1.5.2 Rabi Oscillation

The previous section treated the impact of the density changes $\hat{\rho}_{ii}(t,\tau) - \hat{\rho}_{ii}(t,\tau)$ after a pulsed microwave excitation on the conductivity of the sample. The density changes result from generation-, recombination- and dissociation rates, that control the population of the spin states of the spin pair ensemble. However, these rates are assumed to have time constants much longer than the microwave pulse length, and therefore play a minor role during the pulsed excitation. The density changes during the pulse $\Delta_{ii}(\tau)$ are the result of microwave induced transitions between the spin states and reflect the coherent spin nutations of the spin ensemble. The following analysis neglects any incoherent processes as relaxational processes and spin-spin interactions during the microwave pulse. This simplification can be made, because in general the spin-spin interaction is weak with respect to the Zeeman interaction and since high microwave powers are used in the pulsed measurements, the spin-spin interaction is also weak compared to the microwave field. The spin relaxation times were found to be rather long (10^{-7}-10^{-3} s) [33, 34, 35] in organic materials due to the weak spin-orbit coupling and therefore can be neglected during the very short (10^{-7}s) microwave pulses. The theoretical description of the spin nutation will follow the density operator formalism [30, 31] where the pulsed microwave excitation is treated as a time dependent external perturbation.

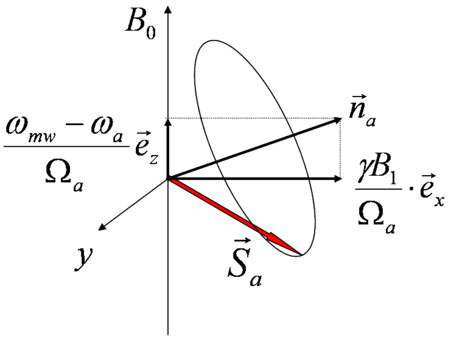

Figure 1.7: *Illustration of the spin motion under the influence of a static magnetic field B_0 and an oscillating microwave magnetic field B_1. In the rotating frame the oscillating field B_1becomes fixed and the static field is compensated when the resonance condition is fulfilled. The spin precesses around the vector $\vec{n}_a$ which becomes parallel to B_1 at resonance.*

In a constant magnetic field B_0 the spin $\vec{S}_a$ precesses aound the axis parallel to B_0 with the Larmor frequency $\omega_a = g_a\mu_B B_0/\hbar$. When the microwave is turned on during an EPR or EDMR experiment, the microwave magnetic field B_1 in the resonator has a component that precesses around B_0 with the frequency ω_{mw} in the same direction as the spin. If the microwave frequency ω_{mw} matches the Larmor frequency exactly the spin will be fixed relative to B_1 in the rotating frame, this situation is illustrated in Fig.1.7. In the rotating frame the static magnetic field B_0 is compensated and the spin starts to precess around the remaining field B_1, inducing transitions between the spin up and down states. However, when the resonance condition is not exactly fulfilled, B_0 is not fully compensated and the spin will precess around a effective field that points along the vector $\vec{n}_a$, given by:

$$\vec{n}_a = \frac{\omega_{mw}-\omega_a}{\Omega_a}\overrightarrow{e_z} + \frac{\gamma B_1}{\Omega_a}\overrightarrow{e_x} \tag{1.39}$$

where $\Omega_a = \sqrt{(\gamma B_1) + (\omega_{mw}-\omega_a)}$ is the Rabi frequency of spin $\vec{S}_a$. The precession of the spin around the axis $\vec{n}_a$ during the microwave excitation of pulse length τ can be expressed by the operator:

$$\hat{D}_{an}(\Omega_a\tau) = exp\left[-\frac{i}{\hbar}\vec{S}_a\cdot\vec{n}_a\Omega_a\tau\right] = 1\!\!1\,cos\left(\frac{1}{2}\Omega_a\tau\right) - i\vec{\sigma}\cdot\vec{n}_a\,sin\left(\frac{1}{2}\Omega_a\tau\right) \tag{1.40}$$

where $\vec{\sigma} = (\sigma_x, \sigma_y, \sigma_z)$ are the Pauli matrices and $1\!\!1$ is the unit matrix. This operator represents represents the spin oscillation in the rotating frame. For a complete description of the spin motion the transformation into the rotating frame has to be included by :

$$\hat{D}_{anz}(\Omega_a, \omega_{mw}, \tau) = \hat{D}_z(\omega_{mw}\tau)\hat{D}_{an}(\Omega_a\tau)\hat{D}_z(\omega_{mw}\tau) \tag{1.41}$$

Since EDMR is always concerned with a pair of spins $\vec{S}_a$ and $\vec{S}_b$ the operator $\hat{D}_{anz}(\Omega_a, \omega_{mw}, \tau)$ has to be expressed in the product space of the the two spins, which yields:

$$\hat{D}_{pair}(\Omega_a, \Omega_b, \omega_{mw}\tau) = \hat{D}_{anz}(\Omega_a, \omega_{mw}, \tau)\otimes\hat{D}_{bnz}(\Omega_b, \omega_{mw}, \tau) \tag{1.42}$$

where $\hat{D}_{bnz}(\Omega_b, \omega_{mw}, \tau)$ is the operator associated with the precession of spin $\vec{S}_b$ around the axis $\vec{n}_b$. Since the operator $\hat{D}_{pair}(\Omega_a, \Omega_b, \omega_{mw}\tau)$ describes the spin precession of both spins during the microwave pulse, the evolution of spin pair ensemble starting from the steady state density matrix given in Eq.1.36 is given by:

$$\hat{\rho}(\tau) = \hat{D}_{pair}(\Omega_a, \Omega_b, \omega_{mw}\tau)\hat{\rho}^{eq}\hat{D}^{\dagger}_{pair}(\Omega_a, \Omega_b, \omega_{mw}\tau) \tag{1.43}$$

The results for $\hat{\rho}(\tau)$ can be plugged directly in Eq.1.35 for the microwave induced density changes which yield for the triplet state densities:

$$\begin{aligned}\Delta_{11,44}(\tau) &= \frac{\rho_{11,44}(\tau) - \rho^{eq}_{11,44}}{Tr\{\hat{\rho}^{eq}\}} = \left[cos^2\left(\frac{1}{2}\Omega_a\tau\right) + \left(\frac{\omega_{mw} - \omega_a}{\Omega_a}\right)^2 sin^2\left(\frac{1}{2}\Omega_a\tau\right)\right] \\ & \times \left[cos^2\left(\frac{1}{2}\Omega_b\tau\right) + \left(\frac{\omega_{mw} - \omega_b}{\Omega_b}\right)^2 sin^2\left(\frac{1}{2}\Omega_b\tau\right)\right] \\ & + sin^2\left(\frac{1}{2}\Omega_a\tau\right) sin^2\left(\frac{1}{2}\Omega_b\tau\right)\left(\frac{\gamma B_1}{\Omega_a}\right)^2\left(\frac{\gamma B_1}{\Omega_b}\right)^2 - 1\end{aligned} \tag{1.44}$$

This formula is a general expression for the density changes of the triplet states and is rather lengthy but it can by simplified by taking into account a few assumptions concerning selective and not selective excitations. The density changes of the mixed states have a similar time dependence as the triplet states and can be found in [30].

Selective Excitation ($\delta\omega \gg \gamma B_1$)

If the Larmor frequencies $\omega_{a,b}$ of spin $\vec{S}_a$ and $\vec{S}_b$ are well separated, the spins can be addressed individually by the microwave field. In the case were the microwave field is resonant with spin $\vec{S}_a$, spin $\vec{S}_b$ will be far off resonant $\omega_{mw} - \omega_b \gg \gamma B_1$. This situation allows selective excitation of both spins and is observed when the condition for large Larmor separation ($\delta\omega \gg \gamma B_1$) is fulfilled. This case makes the following approximations reasonable:

$$\frac{\omega_{mw} - \omega_b}{\Omega_b} \approx 1, \qquad \frac{\gamma B_1}{\Omega_b} \approx 0 \tag{1.45}$$

With these assumptions Eq.1.44 simplifies to:

$$\Delta_{11,44}(\tau) = -\frac{\gamma^2 B_1^2}{\Omega_a^2} sin^2\left(\frac{1}{2}\Omega_a\tau\right) = -\frac{1}{2}\frac{\gamma^2 B_1^2}{\Omega_a^2}\left[1 - cos\left(\Omega_a\tau\right)\right] \tag{1.46}$$

which reflects the Rabi-oscillations of the resonant spin $\vec{S}_a$ with the frequency Ω_a whereas spin $\vec{S}_b$ is offresonant at the same time. The situation is totally symmetric when spin $\vec{S}_b$ becomes resonant with the microwave and spin $\vec{S}_a$ is off resonant. In the case of selective excitation, in general two resonance lines according to the two spins of the pair are expected in the EDMR spectrum.

Non Selective Excitation ($\delta\omega \ll \gamma B_1$)

If the Larmor frequencies $\omega_{a,b}$ of spin $\vec{S}_a$ and $\vec{S}_b$ are very close, both spins will be excited at the same time by the microwave field, which makes a selective excitation of the individual spins impossible. As a result the Larmor frequencies $\omega_{a,b}$ of the individual spins can be expressed by the average Larmor frequency of the spin pair $\omega_0 = (\omega_a + \omega_b)/2$. This leads to the following approximations:

$$\left(\frac{\omega_{mw}-\omega_a}{\Omega_a}\right)^2 \approx \left(\frac{\omega_{mw}-\omega_b}{\Omega_b}\right)^2 \approx \left(\frac{\omega_{mw}-\omega_0}{\Omega_0}\right)^2 \tag{1.47}$$

$$\text{and} \quad \Omega_a \approx \Omega_b \approx \Omega_0 = \sqrt{\gamma^2 B_1^2 + (\omega_{mw}-\omega_0)} \tag{1.48}$$

As a result Eq.1.44 simplifies to the following expression:

$$\Delta_{11,44}(\tau) = -\frac{1}{2}\frac{\gamma^2 B_1^2}{\Omega_0^2} sin^2(\Omega_0\tau) - \frac{1}{2}\frac{\gamma^2 B_1^2(\omega_{mw}-\omega_0)^2}{\Omega_0^4} sin^4\left(\frac{1}{2}\Omega_0\tau\right) \tag{1.49}$$

where the second term becomes zero under resonance conditions $\omega_{mw} - \omega_0$. Neglecting the second term yields for the density changes:

$$\Delta_{11,44}(\tau) = -\frac{1}{2}\frac{\gamma^2 B_1^2}{\Omega_0^2} sin^2(\Omega_0\tau) = -\frac{1}{4}\frac{\gamma^2 B_1^2}{\Omega_0^2}\left[1 - cos(2\Omega_0\tau)\right] \tag{1.50}$$

This result states that in the case of small Larmor separation ($\delta\omega \ll \gamma B_1$) the state density oscillates with twice the Rabi-frequency $2\Omega_0$. This phenomenon will be investigated in § 5.2, where it is compared to the spin locking effect in reaction yield detected magnetic resonance in radical pairs. In general spin $\vec{S}_a$ and $\vec{S}_b$ often exhibit Larmor distributions that have an overlap region were the doubled Rabi frequency observed. This is frequently accompanied by spin pairs that have large Larmor separation and show only the regular Rabi-frequency.

The Function T(α)

The solutions gained for selective and non selective excitation in Eq.1.46 and 1.50 do not include Larmor distribution of the spins $\vec{S}_a$ and $\vec{S}_b$ of the pair. Since such distributions are often observed in radical pairs [36, 37], they should be added for a complete description. This can be achieved by introducing functions of the Larmor frequencies $\Phi(\omega_a)$ and $\Phi(\omega_b)$ for both spins in the pair, which are usually of the Gaussian type. The density changes of the whole spin pair ensemble can be expressed by the integral:

$$\Delta_{eff}(\tau) = \int_{-\infty}^{\infty}\int_{-\infty}^{\infty} \Phi(\omega_a)\Phi(\omega_b)\Delta_{11,44}(\tau)d\omega_a d\omega_b \tag{1.51}$$

Considering the two cases of selective and nonselective excitation once more, the two integrals in Eq.1.51 can be simplified to a single one. During selective Excitation only one of the spins has to be considered, whereas the other one is off resonant. In the case of non selective excitation a common Larmor distribution $\Phi(\omega_0)$ for both spins can be assumed. A general equation for the effective density changes can be given by:

$$\Delta_{eff}(\tau,\omega_{mw}) = \int_{-\infty}^{+\infty} \phi(\omega_L)\frac{1}{2\kappa}\frac{\gamma^2 B_1^2}{(\gamma B_1)^2+(\omega_{mw}-\omega_L)^2} sin^2\left(\kappa\sqrt{(\gamma B_1)^2+(\omega_{mw}-\omega_L)^2}\tau\right)d\omega_L \tag{1.52}$$

where ω_L and κ are parameters that depend on the type of excitation

$$\begin{array}{lllll} \text{1. Selective excitation:} & (\delta\omega \gg \gamma B_1): & \Longrightarrow & \omega_L = \omega_a \quad \text{and} & \kappa = \frac{1}{2} \\ \text{2. Non selective excitation:} & (\delta\omega \ll \gamma B_1): & \Longrightarrow & \omega_L = \omega_0 \quad \text{and} & \kappa = 1 \end{array} \tag{1.53}$$

Eq.1.52 reflects the coherent Rabi-oscillation of a spin pair ensemble during the microwave pulse for the cases of selective or non selective excitation. Although Larmor distributions are included, the formula describes only the extreme cases of complete selective or complete non selective excitation. Since in general only a part of the spin pair ensemble is non selectively excited, the complete ensemble has to be described by a superposition of different density functions $\Delta_{eff}(\tau,\omega_{mw})$, as demonstrated in § 6.4. Eq.1.52 can be simplified when the Larmor distribution is set to a constant value $\phi(\omega_L) = const.$. This can be profitable when only the

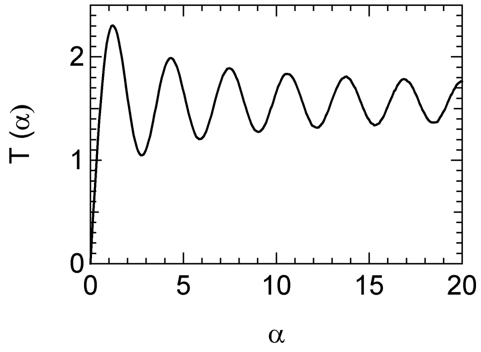

Figure 1.8: *The transient function $T(\alpha)$ reflects the Rabi oscillation of the spin ensemble during the microwave pulse. The turning angle $\alpha = \Omega\tau$ depends on the pulse length. The data for $T(\alpha)$ were obtained from numerical integration.*

time dependence of $\Delta_{eff}(\tau,\omega_{mw})$ is of interest. In this case Eq.1.52 can be simplified to:

$$T(\alpha)=\int_{-\infty}^{+\infty}\frac{sin^2\left(\alpha\sqrt{1+x^2}\right)}{1+x^2}dx \tag{1.54}$$

where $\alpha=\kappa\gamma B_1\tau$ is the turning angle and $x=(\omega_{mw}-\omega_L)/\gamma B_1$. It can be shown that the transient function T(α) is related to the Bessel function of the first kind J_0:

$$T(\alpha)=\pi\int_0^{\alpha}J_0(2x)dx \tag{1.55}$$

Neither Eq.1.52 nor $T(\alpha)$ can be integrated analytically, which makes fitting procedures rather complicated. However, it is possible to fit the derivative of the data by the integrand of $T(\alpha)$ or $\Delta_{eff}(\tau,\omega_{mw})$ and carry out a numerical integration afterwards. The result of an numerical integration of $T(\alpha)$ is displayed in Fig.1.8.

Chapter 2

Experimental Background

This chapter provides informations about the organic materials and their preparation as well as the experimental foundations used in this work. It begins with the electrical and optical properties of the organic materials ZnPc and C_{60}. Whereas the section on fullerenes also reviews the results from previous EDMR measurements on C_{60} the part concerning the phthalocyanines contains a discussion about the the g-values of the ZnPc radicals. Since it will be useful for the interpretation of the EDMR spectra the ZnPc radical cation g-factor will be determined by ESR measurements of iodine doped material. The last part of this chapter contains information about the device fabrication and the experimental setup.

2.1 Organic Materials

2.1.1 Fullerene C_{60}

The Fullerenes were discovered experimentally in 1985 by H. W. Kroto, J. R. Heath, S. C. O´Brian, R. F. Curl, and R. E. Smalley during experiments on carbon clusters [38]. However, the existence of C_{60} was already predicted by Eiji Osawa in 1970 [39] in a Japanese magazine. The structure of C_{60} containing 12 pentagons and 20 hexagons of carbon atoms arranged in an I_h-symmetry is spherical and resembles a football. Besides diamond, graphite and coal, the fullerenes are a new form of carbon, with outstanding properties. The spherical symmetry makes the molecule very stable and enables thermal deposition from the vapor phase. In solid bulk material fullerenes are bound by weak Van der Waals interaction showing an fcc-structure. Thin films are often polycrystalline with grain sizes dependent on the substrate temperature during vacuum evaporation. At room temperature the grains are approximately 50 nm in diameter [4] with increasing grain size for higher substrate temperatures. A review of the electronic and conductive properties are given in [40, 41].

Conductivity and electronic structure

Fullerene thin films are n-type semiconductors with a room temperature conductivity ranging between $\sigma = 10^{-8}\Omega^{-1}cm^{-1}$ [40] and $\sigma = 10^{-6}\Omega^{-1}cm^{-1}$ [42]. The semiconducting properties are a result of the electronic energy level in C_{60} which show a gap between the fully occupied HOMO and the LUMO of approximately E_{Gap}= 2.3 eV, see Fig.2.1 a). This value was determined by Lof et al. [43] using photo electron spectroscopy (PES) and inverse PES. Additional optical excitations at 1.6eV and 1.8 eV were attributed to Frenkel type excitons with singlet and triplet character, respectively. C_{60} thin films are assumed to have a band structure similar to disordered semiconductors with band tail states and deep levels in the band gap. The width of the electronic bands is about 0.4 eV.

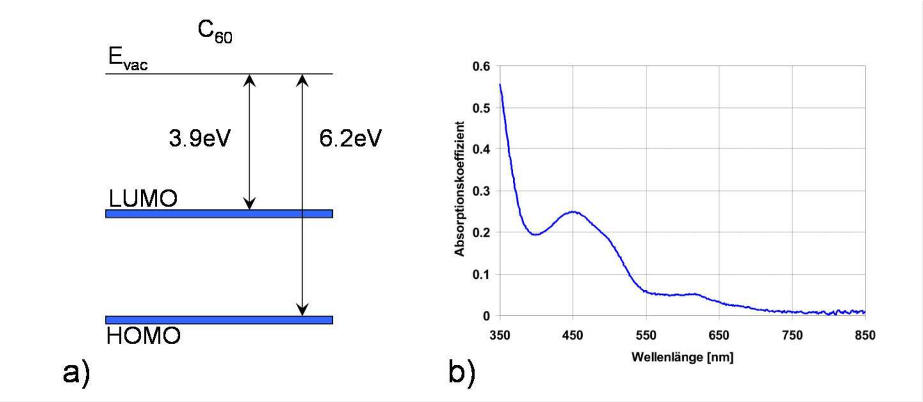

Figure 2.1: *a) C_{60} bandgap, b) absorption spectrum of C_{60} -thin film, taken from[44]*

Sensitivity to Gases

C_{60} thin films are extremely sensitive to oxygen exposure. The conductivity decreases by many orders of magnitude under oxygen atmosphere to values down to $\sigma = 10^{-14}\Omega^{-1}cm^{-1}$ [41, 42]. It is assumed that oxygen induces impurity states in the bandgap which can act as trapping or recombination centers. Other gases like nitrogen or argon have no effect on the conductivity of C_{60}.

Mobility

The majority charge carriers in C_{60} are electrons with a mobility of $\mu_e = 1\frac{cm^2}{Vs}$ [45], whereas mobility of the holes is much smaller $\mu_h = 10^{-4}\frac{cm^2}{Vs}$. The conduction mechanism at moderate temperatures can be described by hopping via band tail states and changes only at very high temperatures (near sublimation temp.) to band transport [41].

Photoconductivity and Optical Absorption

The absorption spectrum of a C_{60} thin film is shown in Fig.2.1 b). The direct HOMO- LUMO transition ($h_u \Rightarrow t_{1u}$, 2.3 eV, $\lambda \approx 540$ nm) is optically forbidden and therefore the strong absorption peaks are due to higher excitations. In general, illumination of C_{60} leads to generation of excitons that can dissociate in the bulk or at interfaces, which leads to free charge carriers (polarons). The spectral photoconductance follows roughly the absorption spectrum, however most features are rather due to excitonic than interband transitions. Upon illumination, C_{60} also shows some special properties like photopolymerization and persistent photoconductivity. The former is the spontaneous formation of dimers and oligomers upon illumination with UV- or white light. The polymerization was found to have rather weak influence on the electronic levels of C_{60} [40] and is reversible upon heating over 100°C. Persistant photoconductivity is a phenomenon where the dark current is increased after illumination of the sample. The increased dark conductivity can persist for seconds, hours or days, until the primary conductivity is reached again.

EDMR in C_{60}

Continuous wave EDMR measurements in C_{60} have been reported by Brandt [19], Eickelkamp [21] and Hiromitsu [46]. All authors found a photocurrent quenching signal at g-values in the range of g = 2.0017 - 2.0020 with similar linewidth (0.3 - 0.65 mT). While the details of the spectral features of these EDMR signals differ considerably, the origin of the signals was consistently interpreted as spin-dependent recombination of oppositely charged carriers. Brandt and Eickelkamp used a model where photogenerated non-geminate positive and negative polarons form an exchange coupled pair, before they recombine spin dependently. In contrast to that Hiromitsu assumes an electron hole recombination at impurity centers in the C_{60} material. This is supported by the observation of spin-flip satellites from impurity protons in his sample.

Furthermore, ESR measurements of C_{60} layers also show an impurity signal [47], with a similar linewidth and g-factor (g = 2.0023, ΔB = 0.25 mT) as the EDMR signal, and was previously assigned to different forms of negative C_{60} radicals [48, 49]. These impurities are also discussed in photo luminescence detected magnetic resonance (PLDMR) [50, 51] and light induced magnetic resonance (LESR) [52] of C_{60} films. Reed and Bolskar [53] assume C_{120} or $C_{120}O$ impurities as a possible origin of the ESR signal. Pulsed EDMR measurements, which we carried out in a previous work [2, 3], show that the major feature of the EDMR resonance is a narrow spin 1/2 peak consistent with the impurity signal mentioned by Reed and Bolskar. Additional Raman measurements could also reveal pronounced polymerization of the C_{60} sample [3], which supports the presence of C_{120} species. However, a final proof for the correct assignment of the EDMR signal in C_{60} cannot be provided so far.

2.1.2 Phthalocyanine

Phthalocyanine is a synthetic blue dye that was mentioned for the first time by A. Braun and J. Tcherniac [54] in 1907, when they worked with phthalamide. Nowadays it is used as pigment for plastics and paints, or as photoconducting material in laser printers. A review of the structure and electrical conduction properties of phthalocyanine thin films was given by R. D. Gould [6].

Morphology

The chemical formula of metalfree phthalocyanine H_2Pc is shown in Fig.2.2 a). The central ring of this planar organic molecule consists of a system of 18 delocalized π-electrons and bears resemblance to the porphyrins [55]. In metal-phthalocyanines, such as ZnPc (Fig.2.2 b), the two central hydrogen atoms are replaced by a single metal atom. With a diameter of $\varnothing = 1.5\,nm$ [56] ZnPc is small and stable enough to be thermally evaporated. J. M. Robertson [57], who investigated metalfree, nickel, copper and platinum phthalocyanines with X-ray reflection techniques pointed out, that the crystal structures of the parent phthalocyanine and many of the metallic derivatives are dimensionally very similar, therefore the following structural properties are assumed to apply also for ZnPc. The phthalocyanine solid exhibits a monoclinic lattice structure ($a \neq b \neq c, \alpha = \gamma = 90°, \beta \geq 90°$) with two molecules per unit cell, where the molecules are stacked in columns in the b-dimension. Fig.2.3 b) shows two kinds of arrangements of CuPc molecules, the α and the β phase of the crystal lattice. The in plane distance of the molecules is the same for both modifications, but the inclination changes. Physical vapor deposited CuPc films were investigated by M. Ashida et al [58]. Sublimation at room temperature on a muscovite substrate yields polycrystalline material in α-phase with small fractions of the β-phase. Heating the sample up to T = 300° generates more and more β-phase fractions. It was also found by H. Peisert et al [59] that on a rough surface like indium tin oxide (ITO) the inclination is much higher due to less interaction of the molecules with the

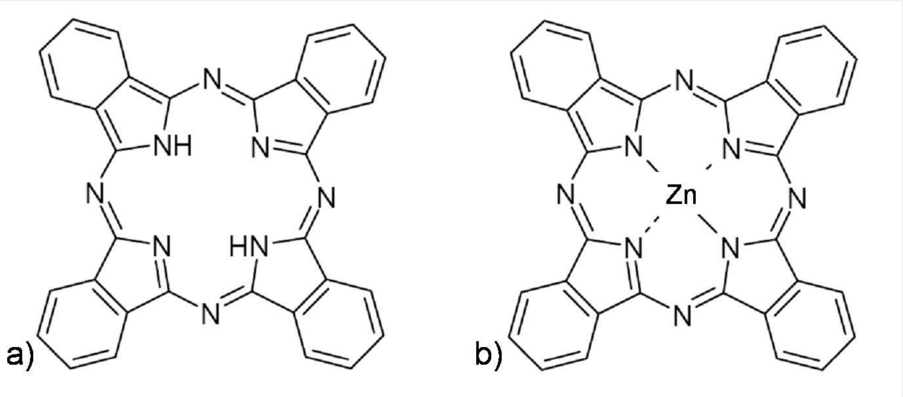

Figure 2.2: *a) metal free phthalocyanine structure, b) zinc phthalocyanine (ZnPc) structure*

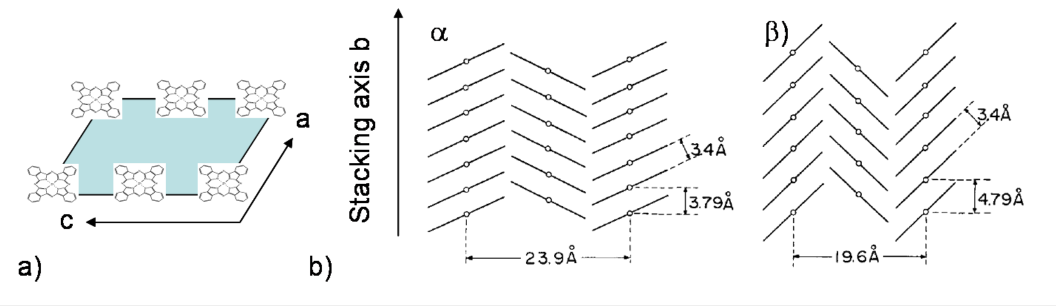

Figure 2.3: *a) lattice structure dimensions a and c, b) stacking angle of CuPc in lattice direction b. taken from [58]*

substrate, therefore the phthalocyanine molecules are rather standing on the ITO-surface.

This has also influence on the conductivity of phthalocyanine thin films, since the π-orbital overlap is much stronger along the stacking axis b, the conductivity is higher in this direction, this was analyzed by J. M. Assour [60]. It also becomes plausible from this argument that the conductivity must be lower for β-phthalocyanines, since the stacking distance b is larger, as confirmed by Kanemitsu et al for H_2Pc [61]

Conductivity

The values for the Conductivity of α-ZnPc given in the literature ranges between $\sigma = 10^{-7}\Omega^{-1}\text{cm}^{-1}$ [5] and $\sigma = 10^{-8}\text{-}10^{-13}\Omega^{-1}\text{cm}^{-1}$ [62].

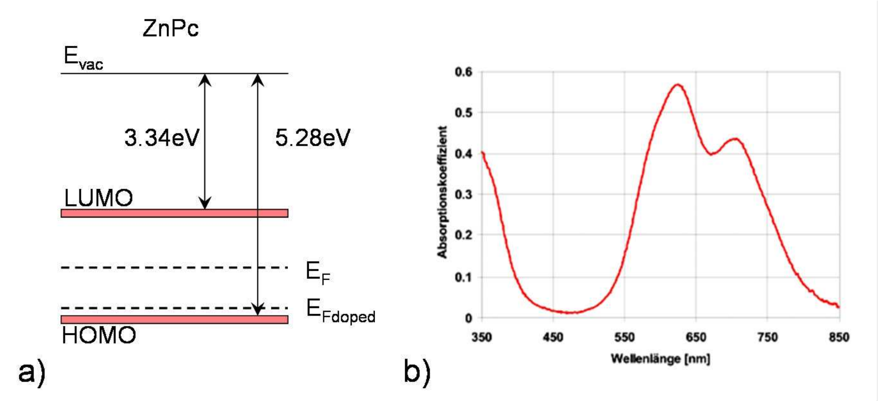

Figure 2.4: *a) ZnPc bandgap, b) absorption spectrum of phthalocyanine, taken from [44]*

Electronic Structure

The ionization energy $E_{ion} = 5.28eV$ and the electron affinity $e\chi = 3.34eV$ of ZnPc evaporated thin films were determined by W. Gao and A. Kahn [63] using UPS and IPES techniques. The resulting direct bandgap between HOMO and LUMO is $1.94eV$ with these values, as illustrated in Fig.2.4 a). They state that the Fermi-level position is near midgap in the undoped case, however upon doping with electronegative tetrafluorotetracyanoquinodimethane (F4-TCNQ) the Fermi-level drops down to $0.18eV$ above the HOMO. Similar results were found by J. Blochwitz et al [64], who investigated ITO/ZnPc Interfaces with UPS and XPS.

Sensitivity To Gases

Many authors report on doping phthalocyanine films or crystals by oxygen gas [65, 66, 60], which enhances the conductivity by a factor of appr.1.5 when the partial oxygen content is increased threefold from atmospheric pressure [65], but also other gases have effects on the conductivity of phthalocyanine. The conductivity is enhanced by dry air and oxygen, but reduced by NH_3 [66] and water vapor [67] with respect to vacuum conditions.

Mobility

The values for hole mobilities of α-ZnPc vary between $\mu = 7.6 \times 10^{-5} cm^2/Vs$ (G. D. Sharma [68]) and $\mu = 1.9 \times 10^{-2} cm^2/Vs$ (A. M. Saleh[69]), Sharma also finds a higher mobility in iodine doped ZnPc ($\mu_{doped} = 3.2 \times 10^{-3} cm^2/Vs$). This large variety of mobilities is the consequence of many properties that influence the electrical conduction in phthalocyanine thin films, such as the morphology, the atmosphere and the purity, that are in turn severely influenced by the fabrication conditions. The electron mobility is assumed to be lower than the mobility of the holes [70], therefore ZnPc and other phthalocyanines act as p-type conductors. There is a common rule of thumb, that charge carrier transport with a mobility less than $\mu = 1\, cm^2/Vs$ is regarded as hopping transport, whereas higher mobilities can be treated as band transport. Although in phthalocyanines the mobility is below this value, transport phenomena are often discussed in the band model [63, 71, 6]. However, the bands are assumed to be rather narrow from $1/100$ eV up to $1/10$ eV [62].

Optical Absorption

The absorption spectrum of ZnPc is shown in Fig.2.4 b). In the visible spectrum phthalocyanine has two absorption bands, the B-band (~350nm) and the Q-band (~650nm). The latter refers to the HOMO-LUMO transition, where the absorbency can reach in this spectral region values up to $\alpha = 1.5 \times 10^5 cm^{-1}$ for CuPc [72]. The contribution of CuPc to the external quantum efficiency of CuPc/PTCBI- solar cells was modeled by Peumans and follows roughly the absorption spectrum.

Photoconductivity

Generation of photocurrent is assumed to proceed via splitting of photoinduced excitons. However, there are different statements about the process of the splitting itself. Loutfy et al. who investigated Al/H_2Pc Schottky-barrier solar cells, assume exciton splitting in the electric field of the Schottky-barrier [73]. Pankow et al. [74] use coplanar gold electrodes that form ohmic contacts to the phthalocyanine and therefore the Schottky-barrier model cannot apply for these devices. Nevertheless, there is an enhanced photoconductivity that can be explained by a model where exciton splitting is assisted by defect and impurity sites. In this context, oxygen is frequently discussed to be essential for Schottky-barrier formation at metal-phthalocyanine interfaces [75, 76]. The authors report on space charge layers that are formed at the organic metal interface under the influence of oxygen, which in turn has also an effect on the photocurrents of these devices.

Table 2.1: *Table of properties (ZnPc, CuPc, C_{60})*

material	el. mobility μ_e ($\frac{cm^2}{Vs}$)	hole mobility μ_h ($\frac{cm^2}{Vs}$)	conductivity σ ($\frac{1}{\Omega cm}$)	gap ΔE (eV)
α-ZnPc	-	$10^{-5} - 10^{-2}$ [68, 69]	$10^{-13} - 10^{-7}$ [62, 5]	1.94 [63]
α-CuPc	3.4×10^{-4} [77]	1.8×10^{-3} [77]	10^{-6} [5]	2.3 [77]
C_{60}	1 [45]	10^{-4} [45]	$10^{-8} - 10^{-6}$ [40, 42]	2.3 [43]

2.2 EPR in ZnPc

In this section the g-factor of the radical cation in ZnPc is determined by EPR. The knowledge of the exact g-value can be useful in the following discussion about the EDMR-signals.

2.2.1 ZnPc Radical Cation g-Value determined by EPR

Electron paramagnetic resonance measurements of phthalocyanines have been reported by several authors. The results for g-factors with the corresponding interpretations are summarized in Table 2.2. Most interpretations involve anions or cations, but also the role of oxygen for the EPR-signal generation was discussed [78, 79], but later refused by others [80, 81]. Some authors also report on defects or impurities [80, 81, 82] as origin for the spin signal, involving the morphology of the material. Finally, chemical reduction and oxidation with different reaction agents were performed [83, 84, 85] in order to determine the radical anion and cation EPR-signals. In this context also the generation of biradicals was mentioned [85, 86]. Summarizing the data of Table 2.2, the g-factor for the cation seems to be somewhat smaller than the one of the anion. However, since it is crucial for the discussion of spin dependent processes to distinguish between electron- and hole-spins, we determined the g-value of cations in our ZnPc material with the help of iodine doping. Sharma et al. [68] investigated the influence of iodine on the electrical properties of ITO/ZnPc/Al devices and found iodine to be an effective p-type doping material for phthalocyanine. Since the iodine acts as an electron

Table 2.2: EPR data for phthalocyanine radicals

Material	interpretation	g-value	Reference
H_2Pc powder	cation	2.003	[79]
ZnPc powder	cation	2.002	[79]
ZnPc (solution)	cation	2.002	[84]
ZnPc powder	cation	2.0026	this work
H_2Pc	cation	2.0024	[85]
H_2Pc	anion	2.0030	[85]
H_2Pc (solution)	anion	2.0031	[83]
H_2Pc film	anion + cation	2.0026	CIDEP[88]
H_2Pc powder	electrons + holes	2.003	[80]
H_2Pc -crystals	unpaired electron	2.0026	[78]
H_2Pc crystal	unpaired electron	2.0030	[81]
ZnPc crystal	unpaired electron	2.0030	[81]
H_2Pc (solid)	decomposition	2.003	[82]
ZnPc (solid)	impurities	2.003	[82]
ZnPc powder	unknown	2.0	[87]

acceptor in contact with phthalocyanine, ZnPc cations will accumulate in the sample during the doping process.

Powder Sample

Phthalocyanine material was purchased from Alpha Aesar and twice sublimed for purity. Electron paramagnetic resonance was performed on the pure ZnPc powder using a commercial Magnettech Miniscope ms100 spectrometer. P-type doping was achieved by adding a small amount of iodine (1mm^3) directly to the ZnPc material. As a result, the EPR signal of the sample increased by one order of magnitude, as illustrated in Fig.2.5 a). The slight shift in the resonance position is probably due to observed fluctuations in the microwave frequency. The width of the Lorenz-shaped resonance is ΔH = 1.17 mT. As g-factor standard we used N@C_{60} diluted in C_{60} (N@C_{60}/C_{60} $\approx 10^{-5}$), which was added to the ZnPc material. The g - value of N@C_{60} g = 2.00212(5) was taken from the publication of Murphy [89]. Since the EPR signal of N@C_{60} is very narrow in comparison to the one of ZnPc it had to be strongly overmodulated in order to observe both signals with similar amplitude. The spectrum of N@C_{60} is composed of three equally spaced lines with equal amplitudes which is superimposed by the broad feature of ZnPc and a weak radical signal. To find out exactly the resonance position of ZnPc, the width and the amplitude of the Lorentzian fit in Fig.2.5 a) were taken to fit the composed spectra shown in Fig.2.5 b). The overmodulated peaks of the three N@C_{60} resonance lines could not be fitted, but since it is known that the three lines are equally spaced, the center of the spectrum can be easily determined. The g-value for the ZnPc cation could be determined to g = 2.0026(2) and fits to the lower values in Table 2.2. The residuum of the fit

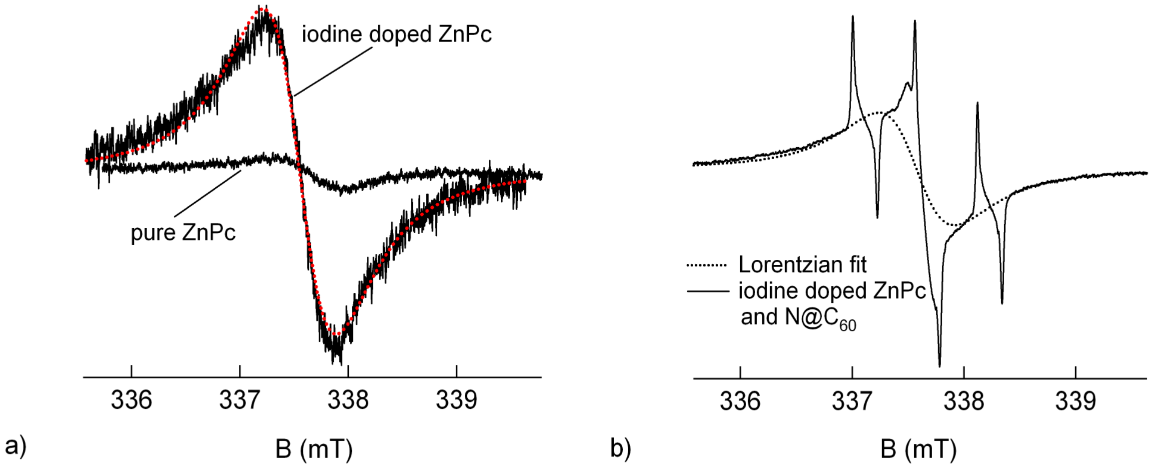

Figure 2.5: *a) EPR-signals of a pure and an iodine doped ZnPc powder sample with Lorentzian fit (red dotted line). b) EPR signal of the iodine doped ZnPc together with a standard sample N@C_{60} (g = 2.0021) for determination of the g-factor of $ZnPc^+$. The spectrum was fitted with a Lorentzian using the width and amplitude of the EPR signal without N@C_{60} in the left graph.*

function consists of the N@C_{60} resonance and the radical signal and is displayed in Fig.2.6 a). Shifting the spectrum by a distance that is equal to the spacing of the three lines and subtracting the result from the unshifted spectrum yields the radical signal, which is displayed in Fig.2.6 b) together with the remaining N@C_{60} spectrum. The radical signal exhibits a Gaussian line shape of ΔH = 0.23 mT width and a g-factor of g = 2.0024(2). Reed and Bolskar [53] summarized g-values for C_{60} radical cations in their review article where most of the values fall in between g = 2.0020 and g = 2.0030 and linewidth of few Gauss (1 G = 0.1 mT). Taking the average of the given g-values yields g = 2.0026(10) which is close to our result. However, there are also reports about oxygen related impurities in C_{60}, that show a similar EPR signal (g = 2.0026(4) [90]).

2.3 Device Fabrication

Since the samples have to meet different requirements for IV-measurements and EDMR measurements, various types of devices were produced for all purposes. The EDMR samples have to fit in small X-Band EPR-tubes of 3 mm inner diameter. They are encapsulated with plugs and shrink tube against atmospheric gases like oxygen and water-vapor. Two types of EDMR samples were fabricated, devices with coplanar contacts (§ 2.3.1) and sandwich devices (§ 2.3.2). Those samples that were used only for IV-measurements in the glovebox could be of larger dimensions (§ 2.3.3).

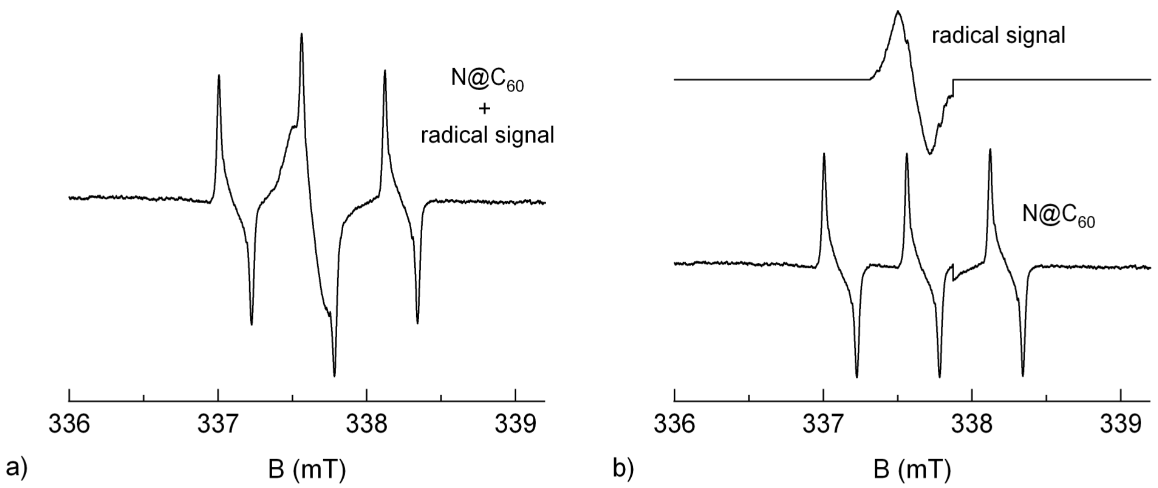

Figure 2.6: *a) residuum of the Lorentzian fit in Fig.3.1 b) containing the N@C_{60} spectrum and a radical signal. b) EPR spectra of the radical peak and N@C_{60} extracted by shifting the spectrum in a) by a distance that is equal to the spacing of the three lines and subtracting the result from the unshifted spectrum.*

2.3.1 Coplanar Au/ZnPc/Au Samples

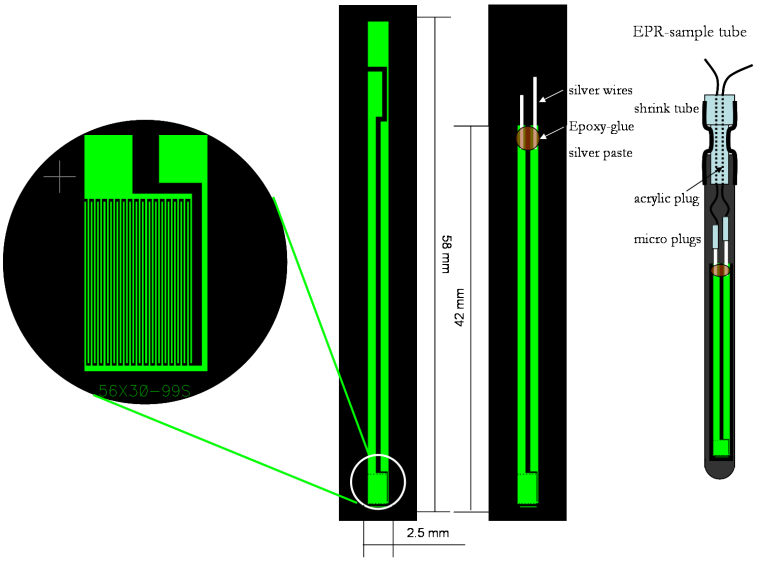

Figure 2.7: *grid samples and encapsulation*

The samples with coplanar gold electrodes are used for IV-measurements as well as for EDMR experiments and thus have to fulfill special constraints for the magnetic resonance. The substrates made from borofloat glas have the dimensions: width x length x height = 2.5 mm x 42 mm x 0.7 mm. The gold contacts were manufactured by photolithography and consist of a 34-finger interdigitated electrode array with a 30 μm gap as shown in Fig.2.7. For effective adhesion of the 100 nm thick gold electrodes on the substrate, a 10 nm chromium layer was used between the glass and the gold. This electrode array acts as a parallel circuit of 33 devices (number of gaps) and therefore reduces the overall resistance of the sample. The current cross section can be estimated by the organic layer thickness x electrode length x number of gaps, assuming that the electron gas spreads out in the whole layer. The samples are rather lengthy in order to keep the contacted wires out of the resonator of the Bruker spectrometer. This was done to avoid disturbance of the microwave modes in the cavity. Since the organic materials C_{60} and ZnPc are both very sensitive to air, encapsulation is crucial for obtaining reproducible results. The encapsulation procedure is shown in Fig.2.7 . After contacting the glued wires of the sample with small plugs, the EPR-tube is sealed with an acrylic plug and a shrink tube. The encapsulation was tested by a simple water bath test. However, this rather primitive encapsulation was enhanced later on in this work, see § 3.2.3.

Prior to the deposition of the organic material, the substrates were cleaned using acetone, ethanol and super Q laboratory water (18,2 MΩ/cm) in a flow box. In order to avoid damages to the microscopic electrode structure on the substrate, no ultrasonic bath was used for the cleaning procedure. After the last cleaning step with water the substrate is dryed with a nitrogen blast. The ZnPc material was purchased from Alpha Aesar and twice sublimed for purity. A shadow mask was used for the deposition process and the sample holder was set in rotation for better homogeneity. A 300 nm thick ZnPc film was grown at a rate of 1 Å/sec under vacuum conditions of typically $p = 10^{-8}$ mbar. The substrate was hold at room temperature.

2.3.2 Sandwich Devices for EDMR

For the ITO/ZnPc/Al samples and the ITO/ZnPc/C_{60}/BCP/Al solar cells, commercial ITO-sputtered glass substrates (width x length x height = 2.5 mm x 58 mm x 0.5 mm) with a sheet resistance of $R_S \leq 5$ Ohm/sq were purchased from PGO. The ITO layer is textured in an L-shape with a laser beam, to provide front and back contacts. In a next step, silver wires are connected to the substrates end with epoxy glue and silver paste, as illustrated in Fig.2.8. Prior

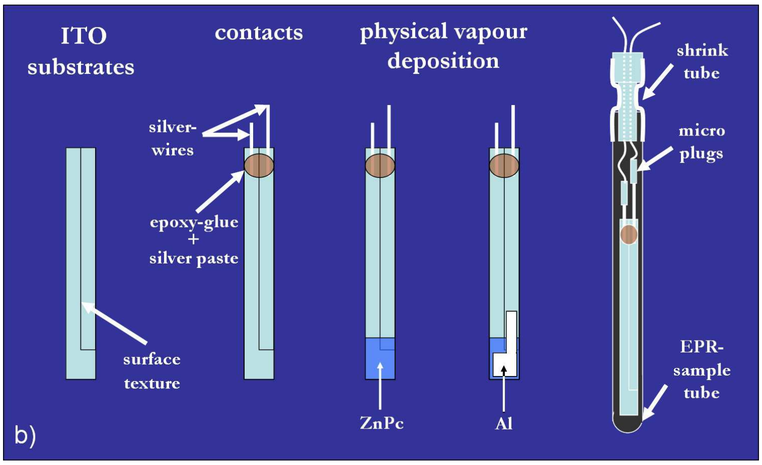

Figure 2.8: *sample preparation and encapsulation ITO/ZnPc/Al*

to the deposition process, a cleaning procedure with different cleaning agents in an ultrasonic bath, is applied to substrate: acetone, ethanol and vector HTR is used together with super Q laboratory water (18,2 MΩ/cm) in a flow box. Each cleaning agent is used for 10 min. in the ultrasonic bath with a sequence of: acetone, water, ethanol, water, vector HTR, water. After the last cleaning step with water, the substrate is dried with nitrogen gas.

The ZnPc layer and the aluminum metallization were added by physical vapor deposition using different evaporation masks. The evaporation conditions are listed in the experimental chapters. We refer to the aluminum electrode as the top contact and denote the layer system as back-contact/organic/top-contact, which is in this case ITO/ZnPc/Al. Illumination is done from the ITO-side. To avoid short circuits due to diffusion of the metal top contact into the organic layer, a thickness of 200 nm was chosen for the ZnPc EDMR-samples. They tended to be more susceptible to short circuits than the samples for the IV-characterization, where 120 nm layer thickness was used. As we found out later, the reason for the short circuits was the broad and very rough laser texture of the ITO substrate. This texture was much narrower in the substrates we used for IV-characterization. The problem could be solved by adding an insulating paint on top of the texturing. The encapsulation method is the same as in the case of the coplanar samples described in § 2.3.1. The device area is equal to the area of the aluminum contact, which was changed during production from A $\approx$ 0.04 cm^2 to A $\approx$ 0.05 cm^2 for new samples.

2.3.3 Sandwich Devices for IV-Characteristics

For the ITO/ZnPc/Al sandwich devices, ITO sputtered glas substrates with a sheet resistance of $R_S \leq 5$ Ohm/sq were purchased from PGO. The contact geometry is provided by laser beam texturing of the ITO layer in a T-shaped fashion (see Fig.2.9). The cleaning procedure applied to the substrates is the same as described in the previous section for the EDMR samples. ZnPc (Alpha Aesar), twice sublimed for purity, was applied to the sample by physical vapor deposition. The metallization followed by the same process technique. The details for the physical vapor process are given in the experimental chapters. The overall device ITO/ZnPc/Al was transferred to a nitrogen glovebox without exposure to air.

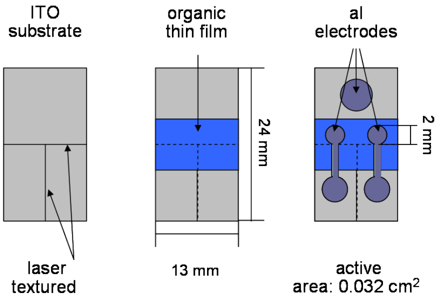

Figure 2.9: *preparation of ITO/ZnPc/Al samples for IV-characterization*

2.4 Experimental Setup

2.4.1 IV-Glovebox-Setup

We used two setups for measurements of the IV-characteristics. The main setup is incorporated into a nitrogen glovebox that is connected to the high vacuum chamber for physical vapor deposition (PVD). This allows fabrication and measurement without intermediate exposure to air. A halogen light source (ELH, P≈100 W) was used for illumination and the IV-characteristics were recorded with a Keithley 2400 sourcemeter. Further current voltage measurements were performed on a Bruker Elexsys 580, which is specified in the following section. In the IV measurements in the Bruker setup different light sources were used for illumination: LOT Oriel (0-200 W) and Schott KL 2500 LCD (0-100 W). Since the viewport of the resonator contains a metal grid to avoid microwave losses, the light intensity is attenuated at the sample location, by passing through this grid. The electrical equipment for the IV-characteristics was a Keithley 237 source measurement unit.

2.4.2 EDMR Setup

The EDMR measurements were carried out on a X-Band Bruker Elexsys 580 spectrometer with a flexline resonator ER4118XMD5RT. In addition to the EPR-setup, a voltage or current source was used together with a current amplifier. For cw-EDMR, the output of the Femto DLPCA-200 current amplifier was connected to the signal input of the Bruker spectrometer. For the pulsed measurements the signal was fed into the transient recorder. Different voltage and current sources were used for the high ohmic coplanar devices and low ohmic sandwich devices. In the pulsed EDMR measurements, a Stanford Research Systems SR 570 current

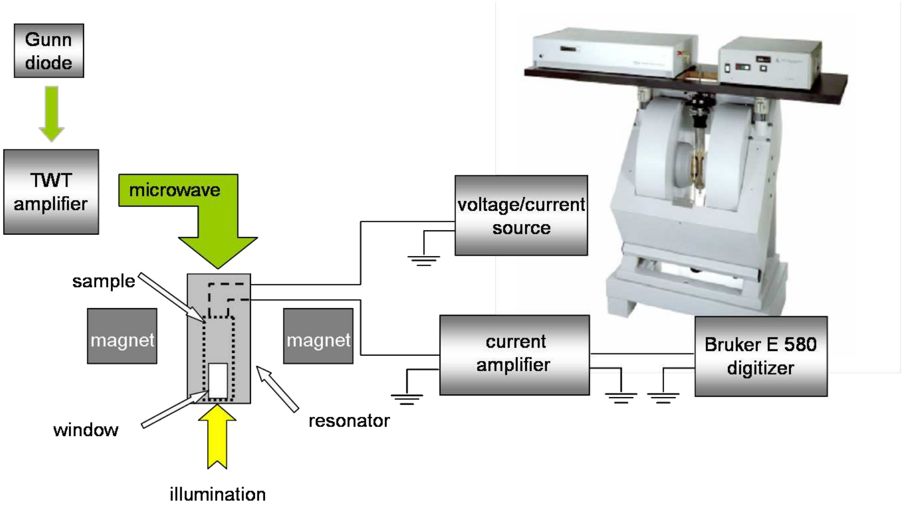

Figure 2.10: *EDMR setup: Bruker Elexsys E580 + electrical detection setup + illumination by Schott KL 2500 LCD (0-100 W) or LOT Oriel (0-200 W).*

Table 2.3: *Electrical detection setup*

EDMR technique/ Device	current/ voltage source	current amplifier	voltage amplifier
cw-EDMR coplanar device	Keithley 230 voltage source	Femto DLPCA-200	-
cw-EDMR sandwich device	SR SIM928 voltage source	Femto DLPCA-200	-
pulsed EDMR coplanar device	Keithley 220 current source	SR 570	Femto DHPVA-200
pulsed EDMR sandwich device	SR SIM928 voltage source	SR 570	Femto DHPVA-200

amplifier worked in line with the Femto DHPVA-200 voltage amplifier to gain better sensitivity. The different setups for the electrical detection are summarized in Table 2.3. The Bruker 8 bit digitizer works in a range from V = -0.5 V to V = + 0.5 V. Since all EDMR signals in this work were observed under illumination, a resonator with an optical viewport was utilized. Two different light sources, Schott KL 2500 LCD (0-100 W) and LOT Oriel (0-200 W), were used for illumination.

Chapter 3

Charge Transport in Phthalocyanine Devices

EDMR offers the possibility to probe defects and loss mechanisms in organic semiconductor devices with high sensitivity. However, the identification of the underlying electronic processes (recombination, hopping, bipolaron formation, triplet-triplet quenching) and their location in the sample is still a matter of current research. Hence, a systematic device characterization is crucial for a better understanding of the spin-dependent transport observed in EDMR measurements. In the following sections, the results of transport studies in two different devices, coplanar Au/ZnPc/Au and vertical ITO/ZnPc/Al samples, will be given. By changing the electrode materials the effect of interface barriers on the transport and the EDMR signals can be evaluated. In the coplanar device where bulk transport dominates, temperature dependent IV-characteristics will be presented, whereas the sandwich device is characterized by a Schottky barrier. Furthermore, the degradation of the ITO/ZnPc/Al sample is studied in detail and the effect of a more efficient encapsulation technique will be discussed.

3.1 Bulk Transport in Au/ZnPc/Au Coplanar Devices

In order to study the bulk transport mechanisms in ZnPc a sample with coplanar gold electrodes was chosen, since gold is known to provide Ohmic contacts to ZnPc [91]. The experimental conditions and the device fabrication can be reviewed in § 2.4.1 and § 2.3.1 respectively. The dark and illuminated IV-characteristics of an Au/ZnPc/Au device are illustrated in Fig.3.1a) and show nearly Ohmic behavior. Under illumination ($P \approx 100$ W) the sample current enhances by a factor of $J_{ill}/ J_{dark} \approx 2.4$, whereas the dark conductivity in the quasi-linear IV regime is $\sigma = 2 \times 10^{-7}\Omega^{-1}\mathrm{cm}^{-1}$, compare to §2.1.2. In Fig.3.1b) the dark current of the sample is plotted over an extended voltage range of 150 V in a double logarithmic presentation. Over a large voltage range (5-50V) the current varies nearly linearly with the voltage ($J \sim V^{1.17}$), but in the high voltage region (50-150V) a power law is observed ($J\sim V^{1.62}$).

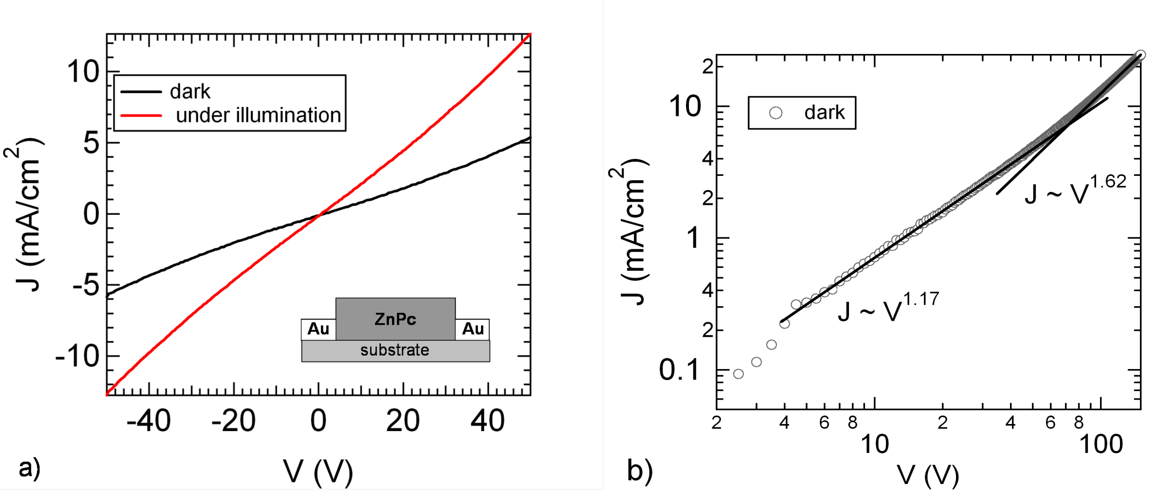

Figure 3.1: *a) IV-characteristics of a coplanar Au/ZnPc/Au device (electrode area: 3x10*$^{-4}$*cm*^{2}*, 30 µm electrode gap) in nitrogen atmosphere with and without illumination (halogen lamp ELH, P ≈ 100 W). b) Log-log-plot of the IV-curve without illumination over an extended voltage range of 150 V. The circles mark the data, whereas the lines indicate the different power laws according to the different transport regimes.*

Ohmic IV-dependency at low voltages combined with a powerlaw behavior at high voltages is characteristic for space charge limited currents. However, in general the power law is at least proportional to J $\sim$ V^2 in the case of monoenergetic shallow traps, as well as in the absence of traps (see § 1.1.1) . The reason for the low power IV-dependence can be explained as follows. Since there is still curvature in the run of the current trace at V = 150 V, one can assume that the regime of SCLC is not fully reached at this voltage. Therefore, only the transition region between these regimes can be observed, and the slopes are not at their maximum value. Since higher voltages may damage the sample, V = 150 V was not exceeded. The ohmic behavior of the electrodes can be explained by the high workfunction of Au (ϕ = 5.2 eV), which provides a good contact for holes since it is close to the HOMO of ZnPc (E_{Ion} = 5.28 eV). Similar results were found by Meissner et al. [91] for Au/ZnPc/Au and by A. Sussman [92] in Au/CuPc/Au devices (both sandwich type).

3.1.1 IV-Temperature Dependency

The temperature dependence of IV-curves can reveal the characteristic behavior of space charge limited currents, which is the expected transport in ZnPc at higher voltages. Therefore this method was applied to the coplanar Au/ZnPc/Au sample. The experiment was carried out in the Bruker setup with (Schott KL 2500 LCD), P ≈ 100 W illumination, for details see § 2.4.2. The first measurement was done at T = 300 K, afterwards the setup was cooled down to T = 200 K and then the temperature was increased step by step up to T = 280 K. Below 200 K, the current was too weak for the sensitivity of the setup. The IV-curves for different temperatures in a double logarithmic plot are given in Fig.3.2 a). The slopes of the fit functions

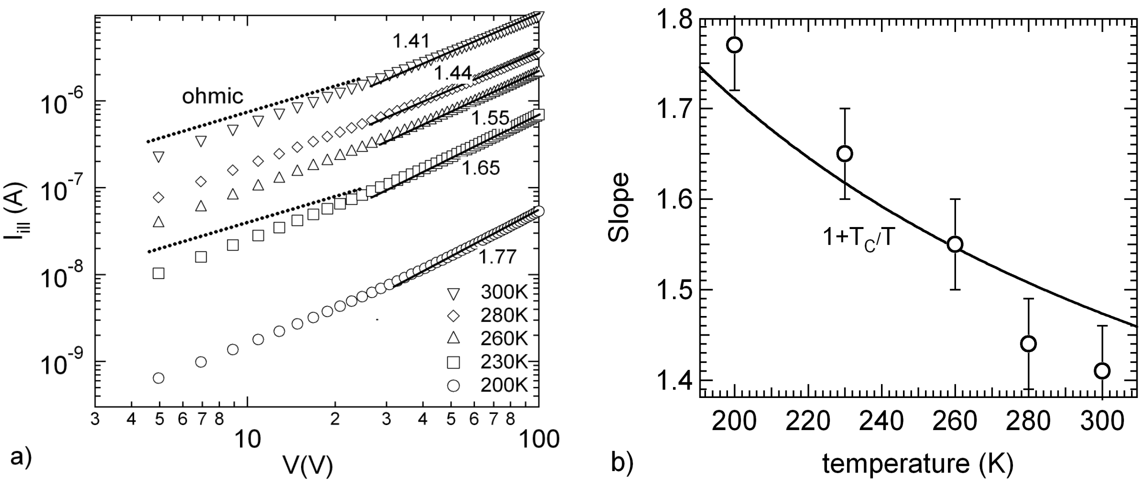

Figure 3.2: *a) IV-curves of a coplanar Au/ZnPc/Au device under Illumination of P ≈ 100 W at different temperatures in double logarithmic presentation, b) slopes in the high voltage regime vs. temperature. The fit function is the expected temperature dependence of the slopes for SCLC with exponential trap distribution.*

(lines) are indicated in the plot, they represent the exponent x of the power law I $\sim$ V^x. In the high voltage regime, the slopes increase with decreasing temperature, which is expected when SCLC with an exponential trap distribution is considered. Although this behavior is primarily expected for the dark IV-characteristics, A. Sussmann has shown [92] that the effect is also present in illuminated CuPc-samples. The temperature dependence of the IV-characteristics is given by (see § 1.1.2),

$$I \sim U^{(T_C/T)+1} \tag{3.1}$$

where T_C is a coefficient, that characterizes the trap distribution in the gap. The relation 3.1 fits roughly the temperature dependence of the slopes with a value of T$_C$ = 142 K, as can be seen in Fig.3.2 b). This value is rather small and indicates that at V = 100 V the sample is still in the transition region between the ohmic and the SCLC-regime. The low voltage regime, where an ohmic IV-dependence (dotted line) is expected, shows slightly superlinear behavior which also increases with decreasing temperature. The origin of this effect is still unclear. An Arrhenius plot of the current for different voltages is shown in Fig.3.3 a). Here it is also expected that the major contribution to the IV-characteristics originates from the dark current. Exponential curve fits, indicated by the lines, show that the slopes which are proportional to the activation energies change continuously from low to high voltages. This effect was also observed by A. Sussman [92], studying the temperature dependence of the dark current in Au/CuPc/Au sandwich devices. It is assumed that the activation energy equals the energy difference between the quasi-Fermi-level and the HOMO of ZnPc. In the low voltage limit V = 0 V the quasi Fermi-level will reach the steady state Fermi energy of the ZnPc film. We can now estimate the activation energy of the ZnPc sample from the slope of the Arrhenius-curves

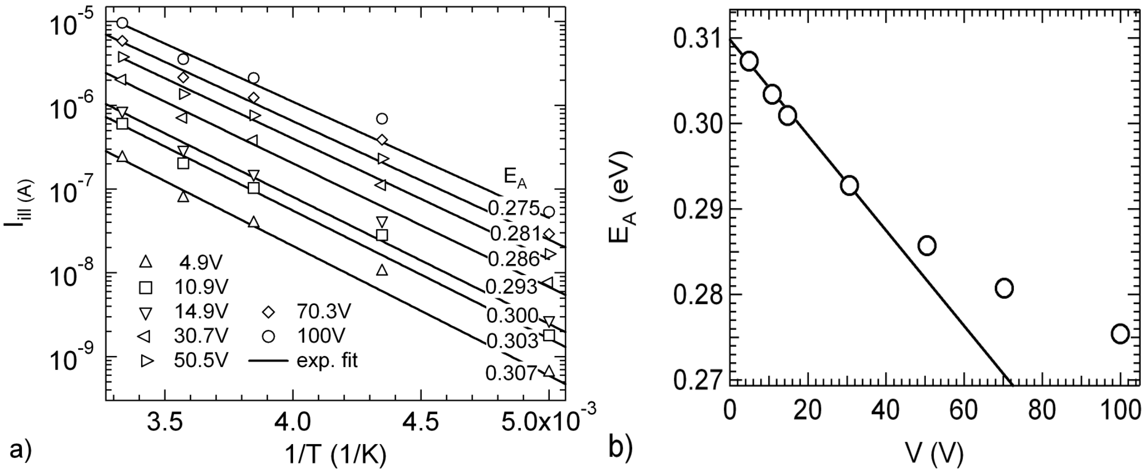

Figure 3.3: *a) Arrhenius plots of the device current under illumination in the coplanar Au/ZnPc/Au sample at different voltages. From the slopes of the exponential fit function indicated in the plot the activation energy can be determined. The slope of the lines is assumed to be proportional to the separation of the Fermi level with the HOMO [92]. b) The activation energy vs. voltage. At V = 0 V the steady state activation energy is reached.*

in the low voltage limit from the relation:

$$I \sim I_0 \, exp\left(-\frac{E_A}{k_B T}\right) \tag{3.2}$$

The result is E_A = 0.31 eV, see Fig.3.3 b). The activation energy gives us an estimate for the distance of the Fermi-level from the HOMO of ZnPc. This result indicates that the ZnPc layer is unintentionally doped, which is not unusual in this material, where especially oxygen impurities have such an effect. Since the sample was illuminated, to gain higher currents, the Fermi-level position might be slightly erroneous. However we will see in the next section that this estimate is quite exact.

3.2 ITO/ZnPc/AL Schottky-Solar Cells

3.2.1 IV-Characteristics (injection vs bulk properties)

The influence of injection barriers on the transport in phthalocyanine will be investigated in sandwich type ITO/ZnPc/Al devices, since the phthalocyanine-aluminum junction is reported to show rectifying behavior [71, 73, 75, 93, 94]. The devices were fabricated by physical vapor deposition on cleaned ITO substrates, the evaporation conditions are summarized in Table 3.1. Further details of the device preparation are given in section 2.3.3.

The current voltage measurements of the ITO/ZnPc(120nm)/Al(100nm) samples was carried out in the glovebox setup described above (§2.4.1). The IV-curves show strong rectifying

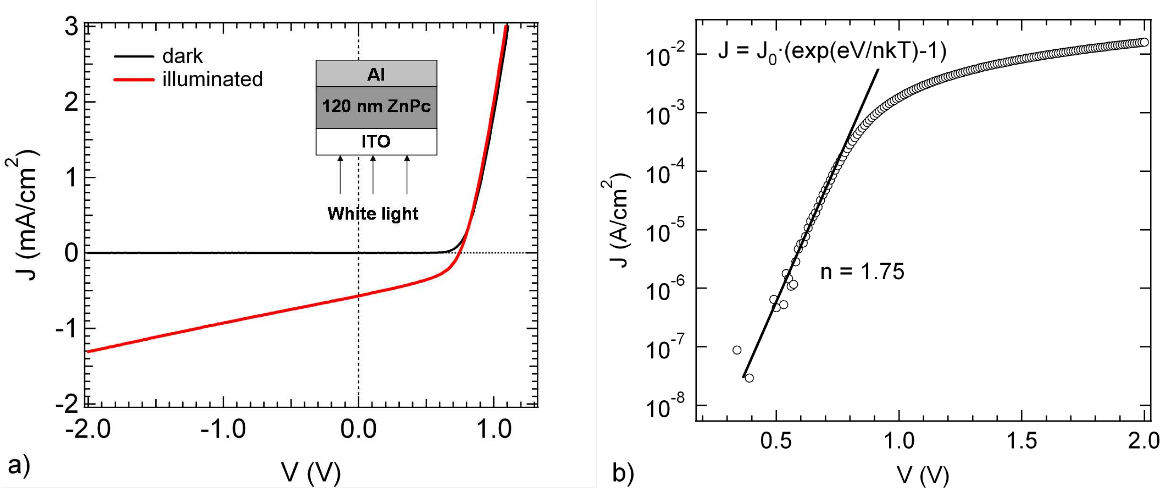

Figure 3.4: *a) IV-characteristics of ITO/ZnPc(120 nm)/Al samples (area = 0.032 cm^2). a) IV-curves in the dark and under white light illumination (P = 100 W), b) semilogarithmic-plot of the dark IV-curve (circles) in a) fitted with the modified Shockley function.*

behavior, where forward bias is achieved with the Al electrode negatively biased, as shown in Fig.3.4 a). A pronounced slope of the photocurrent is observed in the reverse bias regime, which is usually ascribed to a parallel shunt resistance. Since the shunt resistance is not observed in the dark current, the explanation cannot hold for the photocurrent unless the shunt would be photo-induced. A better explanation can be found when a large difference between the mobility of electrons and holes is assumed, which is the case in ZnPc. Whereas the photogenerated holes can reach the electrode regardless of where they were created in the film, a specific number of the less mobile electrons cannot reach the extracting electrode within their lifetime. This would be a limiting factor for the photocurrent. Applying a reverse bias to the sample leads to higher drift velocities of the electrons and consequently more of them can reach the electrode within their lifetime. This would lead to a linear increase of the photocurrent in reverse bias, since the drift velocity is proportional to the electric field. The rectifying behavior can be attributed to a Schottky-barrier at the Al/ZnPc interface, which is also assumed to generate the photocurrent in the device. Since ZnPc is well known to be a p-type semiconductor, the low workfunction of Al (4.2 eV) with respect to the HOMO of ZnPc ($\sim$ 5.3 eV [63]) leads to a barrier for hole injection at this contact. A Schottky barrier at the phthalocyanine/Al junction was observed by different authors [71, 73, 75, 93, 94]. It can be verified by the semilogarithmic plot in Fig.3.4 b) where the dark current could be fitted by the

Table 3.1: *ITO/ZnPc/Al preparation parameters*

Material	thickness (nm)	rate (Å/sec)	source temp. (°C)	p. (mbar)
ZnPc	120	≈1.0	450	2 x 10^{-7}
Al	100	≈0.7	1210	5 x 10^{-7}

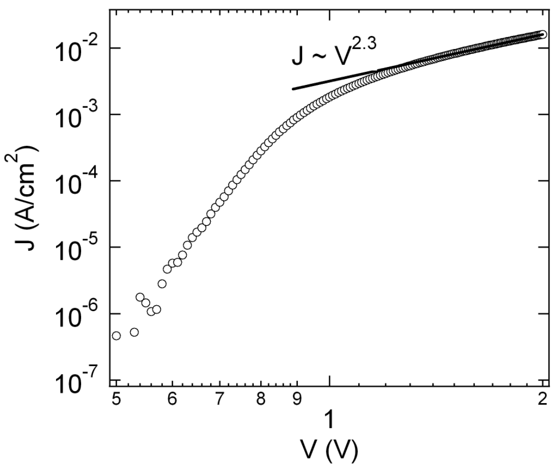

Figure 3.5: *Log-log-plot of the dark IV-curve in Fig.3.4 that shows the power law IV-characteristics at higher voltages.*

modified Shockley equation for thermionic emission over the barrier:

$$J = J_0 \left[exp\left(\frac{eV}{nk_B T} \right) - 1 \right] \tag{3.3}$$

with

$$J_0 = A^* T^2 exp\left[-\frac{eV_B}{k_B T} \right], \tag{3.4}$$

where $A^* = 4\pi e m^* k_B^2 / h$ is the effective Richardson constant. From the fit, which extends over a voltage region from 0.4 V - 0.7 V, we obtain the diode quality factor n = 1.75 and J_0 = 9 x 10^{-12}A/cm^2. Since the Boltzmann constant k_B and the temperature T = 300 K are known, it should be possible to determine the potential barrier height eV_B, if the effective mass m* is known. Because the determination of m* is not possible from the presented data, we assume an effective mass that equals the electron mass m* = m_e. With this assumption eV_B equals 1.1 eV for the barrier height. Remembering that (Eq.1.12)

$$eV_B = E_{ion}^{ZnPc} - \phi_{Al} \tag{3.5}$$

when E_{ion}^{ZnPc} = 5.3 eV and ϕ_{Al} = 4.2 eV are the ionization potential of ZnPc and the workfunction of Al respectively, we exactly obtain the experimental value. For the band-bending or rather the built in voltage V_{bi}, which is given by [94]

$$eV_{bi} = \phi_{ZnPc} - \phi_{Al} \tag{3.6}$$

only a rough estimate can be given here. Since in general $V_{oc} \leq V_{bi}$ [94], the open circuit voltage can serve as a lower limit of the built in voltage. If we assume for simplicity that V_{oc} = 0.74 V $\approx V_{bi}$, the workfunction of ZnPc becomes $\phi_{ZnPc} \approx$ 4.9 eV, which would mean that the Fermi level is 0.4 eV above the HOMO. This result coincides within an error of 0.1 eV with the result of the temperature dependent measurements at the coplanar Au/ZnPc/Au device in § 3.1.1, where the Fermi-level position was determined to be 0.3 eV above the HOMO. The Schottky barrier- and solar cell parameters of the ITO/ZnPc/Al device are listed in Table 3.2. The diode quality factor of n = 1.75 is an indicator for additional processes beside the thermionic emission over the barrier, for instance bias dependence of the barrier height, electron tunneling through the barrier, or carrier recombination in the depletion region [95]. The latter process is an important loss mechanism in solar cells and is assumed to be the most likely candidate for our sample.

Table 3.2: *Schottky barrier- and photovoltaic parameters of the ITO/ZnPc/Al device in the dark and under P ≈ 100 W white light illumination*, where J_{sc} *is the short circuit current ,* η *the external efficiency and ff the fill factor.*

n	V_{oc} (V)	J_{sc} (mA/cm^2)	eV_B (eV)	η (%)	ff (%)
1.75	0.74	0.57	1.1	0.18	42.3

Space Charge Limited Currents (SCLC)

In contrast to the low voltage regime, where the Schottky-diode dominates the IV-curves, in the high voltage regime (1.4 V - 2V) the IV-curve seems to obey a power-law behavior with $J \sim V^x$, as shown in the log-log-plot in Fig.3.5. The exponent x varies between different samples in the range of x = 2.3 - 4.6. As already observed in the coplanar Au/ZnPc/Au samples, this indicates SCLC in the presence of an exponential trap distribution in the bandgap. Since SCLC is a very prominent conduction mechanism in phthalocyanines even in combination with a Schottky-barrier, many authors report on this subject [6, 69, 92, 96, 97]. In this context also trap levels are mentioned that are derived from SCLC measurements, where the trap concentrations vary between (10^{18}-10^{26} m^{-3}) in phthalocyanine sandwich structures [6].

Thickness Dependent IV-Curves (Injection vs. bulk transport)

The IV-analysis of ITO/ZnPc/Al Schottky solar cells shows that two conduction mechanism are present in the device: (i) diode behavior in the low voltage range and (ii) a power law associated with SCLC in the high voltage regime. Whereas the Schottky barrier is a clear indicator for injection limitted currents, in general SCLC requires bulk limited transport. In order to differentiate between these two conduction mechanisms, a thickness dependent current study was attempted. It is generally assumed that in sandwich devices the thickness of the active layer determines the spacing of the electrodes. Since SCL currents exhibit a strong thickness dependence (in particular with exponential trap distribution, as observed in our samples) those should easily be distinguishable from injection limitted currents that are not thickness dependent. In five fabrication runs with eight devices per run the thickness of the ZnPc layer in the ITO/ZnPc/Al device was varied from 40 nm up to 240 nm. To avoid short circuits, the metallization was adjusted to high evaporation rates ∼ 2.5 Å/sec and the thickness was reduced to 50 nm (see Table 3.3): Nevertheless there were always damaged samples that were not included in further investigations. Furthermore, even the IV-curves of devices with the same ZnPc thickness differ significantly from each other resulting in large errors. Fig.3.6 a) displays the forward biased IV-curves for different ZnPc thickness in a double logarithmic plot whereas Fig.3.6 b) shows the averaged current vs. thickness, also in a double logarithmic presentation. From Fig.3.6 it is clear that the 40 nm samples are out of the line, showing very

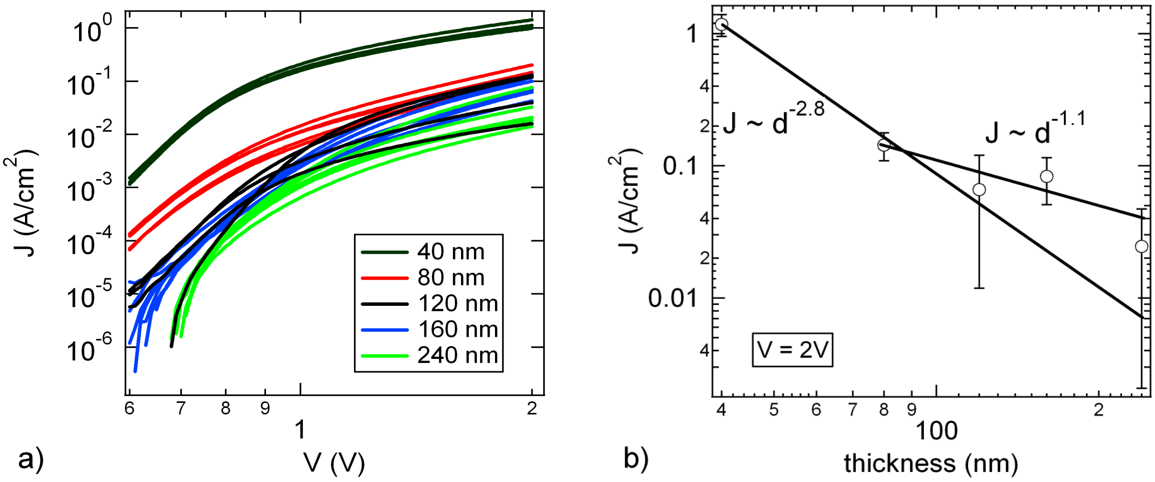

Figure 3.6: *Thickness dependence of the dark current of ITO/ZnPc/Al devices a) IV-characteristics at different temperatures, b) temperature dependence of the current density at V = 2 V.*

Table 3.3: *Preparation parameters of ITO/ZnPc/Al samples with different ZnPc thickness.*

Material	thickness (nm)	rate (Å/sec)	source temp. (°C)	. p. (mbar)
ZnPc	40-240	≈1.0	450	2 x 10^{-7}
Al	50	≈2.5	1350	5 x 10^{-7}

high currents, whereas the rest of the samples show only a weak dependence on the ZnPc thickness. Therefore the thickness dependence of the current (Fig.3.6 b)) was fitted with and without the 40 nm samples. However, neither of these fits shows the expected thickness dependence for SCLC with exponential trap distribution, which should be expressed by:

$$J \sim \frac{V^{l+1}}{d^{2l+1}}, \qquad with \qquad l = \frac{T_C}{T} \tag{3.7}$$

Since the devices show a power dependence of J $\sim$ V$^{2.4\rightarrow 4.6}$ in the high voltage region, the current should vary with thickness as J $\sim$ d$^{-3.8}$, when l = 1.4 is assumed. The weak thickness dependence indicates, that there are additional processes that influence the resistivity of the device. Such a process is metal diffusion into the organic material during the metallization process, which changes the effective ZnPc thickness of the device and is frequently observed in organic devices. Since some of the samples showed short circuits, this process could be one of the reasons for the deviating thickness dependence.

Conclusions

The data extracted from the IV-characteristics can be used to draw a rough picture of the ITO/ZnPc/Al energy level diagram. In Fig.3.7 a) the energy level of ZnPc are shown together with the workfunctions of ITO and Al. The ZnPc HOMO and LUMO levels are taken from Gao and Kahn [63] whereas the workfunction and the indicated trap level distribution were deduced from the IV-experiments in this work. The workfunction of ITO, ϕ_{ITO}, varies in different publications from 4.2 eV [70] to 4.8 eV [98] since it depends strongly on the preparation methods. Although ϕ_{ITO} could not be determined in this work, a rather large value is expected, since the contact at the ITO/ZnPc interface shows ohmic behavior. Ohmic ITO/Pc contacts were also observed by Sharma et al. [68] for ZnPc and by Mahapatro and Ghosh [93] for CuPc. When the materials are brought into contact, a band bending at the ZnPc/Al interface is expected, as depicted in Fig.3.7 b). The Schottky barrier height and the lower limit for the built in voltage indicated in Fig.3.7 were determined from the IV-measurements. The contact is a blocking for hole injection from the Al electrode, as observed in the IV-characteristics

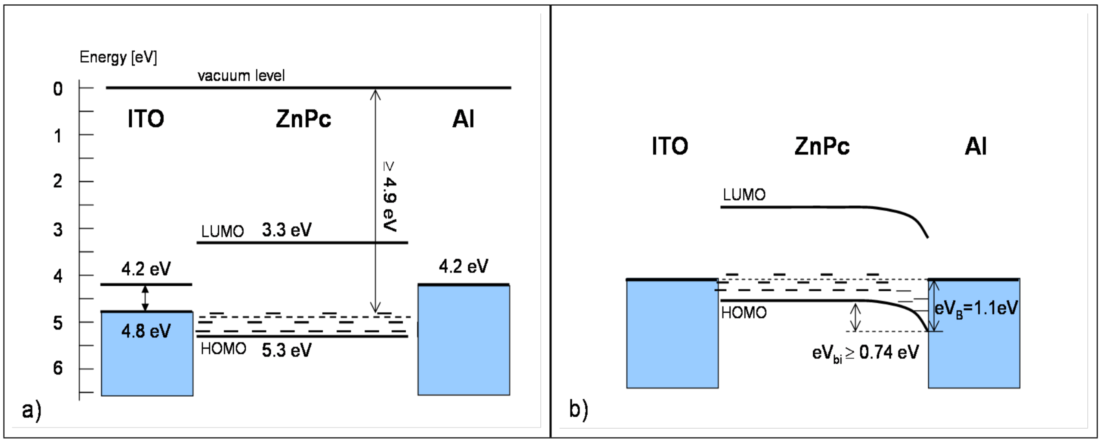

Figure 3.7: *a) Proposed energy level diagram for the ITO/ZnPc/Al Schottky barrier cell, the HOMO and LUMO energy is taken from Gao and Kahn [63], the lower limit for the ZnPc Fermi level is related to the open circuit voltage determined from the IV-characteristics in Fig.3.4. b) materials in contact. The Schottky barrier height was determined from the Shockley fit function in Fig.3.4.*

were reverse bias is attained when Al is positively biased [1].

3.2.2 Degradation of the Al Contact Interface

Although an encapsulation was used in this work most of the devices investigated by EDMR showed more or less degradation. Consequently it is necessary to understand the mechanisms of degradation and to improve encapsulation techniques. This and the following section concentrate on the degradation processes in ITO/ZnPc/Al devices and investigate new encapsulation techniques.

The ZnPc Schottky barrier cells show rather strong degradation in the first hours after production, even under nitrogen atmosphere with an oxygen content of 0.3 ppm. Typically the forward bias dark current decreases with time, as shown in Fig.3.8 for a sample with a 200 nm ZnPc layer. The fabrication details are described in § 2.3.2. The current decrease at V = 2 V is exponential (Fig.3.8 inset) where the time constant varies from sample to sample. For the device in Fig.3.8 the time constant is τ = 27 minutes, which shows that the nitrogen atmosphere cannot sufficiently protect the sample from degradation. In order to enhance the stability of the sample, a 200 nm C_{60} layer was deposited on top of the device as an oxygen getter material. Since the fullerenes are placed on top of the Al contact, neither the current flow nor the illumination from the ITO side is altered by this layer. The fabrication parameters for these cells can be found in Table 3.4. In Fig.3.9 a) the IV-curves of an ITO/ZnPc/Al with a C_{60} protection layer is shown immediately after preparation, one hour later and after four days. The double logarithmic plot shows not only the decrease of the dark current but reveals

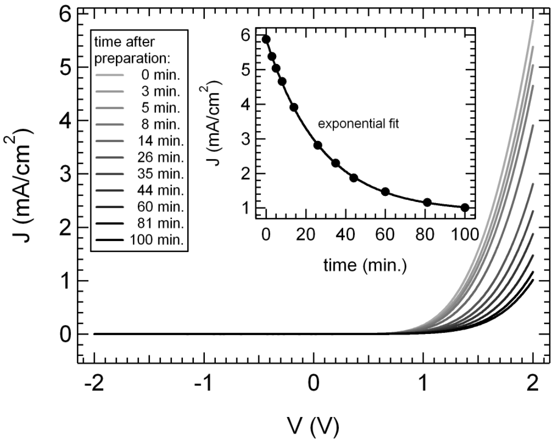

Figure 3.8: *Dark IV-curves of an ITO/ZnPc(200 nm)/Al device as a function of time after preparation recorded in nitrogen atmosphere (0.3 ppm oxygen). The inset shows the device current at V = 2V vs. time fitted with an exponential decay function.*

---

[1] The results were supported by an IV-simulation based on a drift-diffusion model, developed by Wolfgang Tress of the technical University of Dresden. The model is capable to treat thermionic injection at the metals, space charge effects, different expressions for charge carrier mobility, traps, and a spatial generation profile considering thin film optics. The results of these simulations will be published elsewhere.

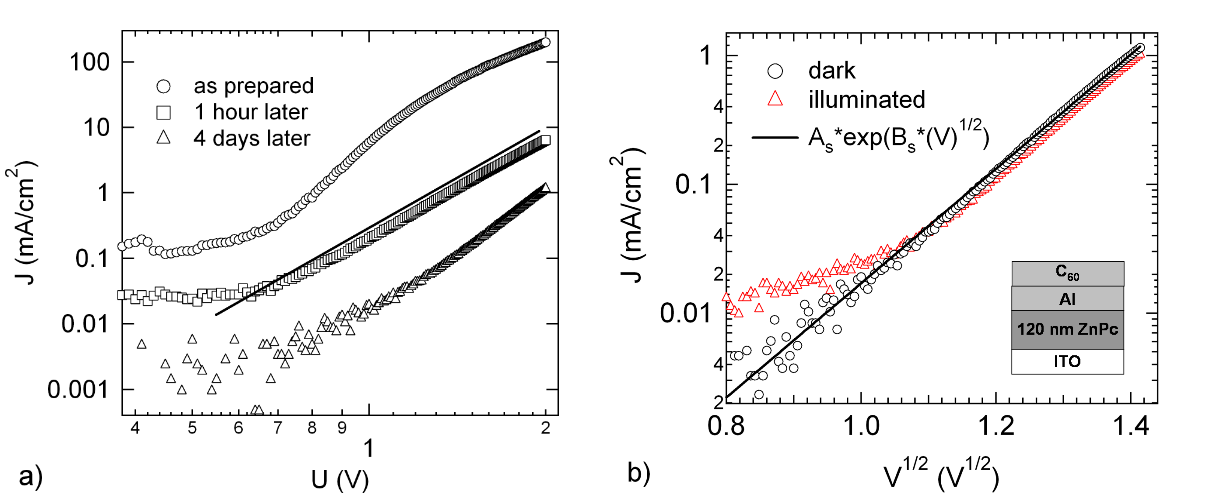

Figure 3.9: *a) Dark IV-characteristics of an ITO/ZnPc(120 nm)/Al cell with a C_{60} protection layer in nitrogen atmosphere (0.3 ppm oxygen) at different times after preparation, b) Schottky emission plot of the IV-curves of the 4 days degraded sample in the dark and illuminated.*

Table 3.4: *Preparation parameters of ITO/ZnPc/Al samples with 200 nm C_{60} protection layer*

Material	thickness [nm]	rate [Å/sec]	temp. [°C]	vacuum p. [mbar]
ZnPc	120	0.9	427	1.4 x 10^{-7}
Al	50	≈ 2.5	1350	1 x 10^{-6}
C_{60}	200	0.9	525	1.4 x 10^{-7}

drastic changes in the transport mechanism. Starting from a Schottky diode with SCLC at high voltages for the as prepared sample, it changes to pure power law behavior (I $\sim$ V^6) after one hour. However after four days in the glovebox the IV-characteristics changes again and deviates from the power law. In Fig.3.9 b) this IV-curve (black circles) is shown in a log I vs $V^{1/2}$ presentation, which is characteristic for Schottky emission usually observed in metal insulator semiconductor (MIS-) devices. Schottky emission transport can expressed as [99, 6]:

$$: J = A_S exp\left(B_S\sqrt{V}\right) \tag{3.8}$$

with

$$A_S = A^* T^2 exp\left(-\frac{\phi_B}{k_B T}\right), \qquad and \qquad B_S = \sqrt{\frac{e^3}{4\pi\varepsilon_r\varepsilon_0 d k_B^2 T^2}} \tag{3.9}$$

where $A^* = 4\pi e m^* k_B^2/h$ is the effective Richardson constant introduced in Eq.3.4, ϕ_B is the barrier height, $\varepsilon_r\varepsilon_0$ are the material- and the vacuum permittivity and d is the film- or insulator thickness. Schottky emission is an injection limitted process that can be observed when emission over a triangular energy barrier takes place. This energy barrier can in principle be a thin insulation layer for example an oxide barrier or a metal insulator barrier. The process takes place when the barrier is lowered by an external electric field. The Schottky emission fit, displayed in Fig.3.9 b), yields for A_S = 6.2 x 10^{-10}A/cm^2 and for B_S = 10.2 V$^{-1/2}$. When again m = m* is assumed for the effective mass in the Richardson constant (in this case: A* = A = 120 A/cm^{2}K^2) we obtain a barrier height of ϕ_B = 0.96 eV. Considering a thin aluminum oxide layer at the Al/ZnPc interface we can calculate from B$_S$ and $\varepsilon_r \approx 3$ (for Al_2O_3 [100]) the value d ≈ 70 Å for the insulation layer thickness , which is a realistic value for an aluminum oxide layer thickness [100]. In conclusion the IV-characteristics can be consistently explained by the formation of an aluminum oxide at the Al/ZnPc interface. The continuous changes of the IV-curves due to the progressive build-up of the oxide barrier can be described qualitatively in an equivalent circuit model using two resistances as reported by Fan and Faulkner [96] for Au/ZnPc/Al Schottky cells. The entire device resistance is composed of the ZnPc bulk resistance and the resistance of the oxide barrier. For the oxide layer they calculate a thickness of 65Å, which is in good agreement with our value (d ≈ 70 Å) and the value of Antula (d = 60 Å [100]), whereas the barrier height is somewhat larger $\phi_B^{Fan\&Faulkner}$= 1.27 eV, (this work: ϕ_B = 0.96 eV). The series resistance model can also explain the time-dependence of the degradation in this work. The current of the freshly prepared samples is controled by a Schottky-barrier at low voltages and by SCLC in the high voltage regime. The degradation increases with the growing of the oxide barrier. If the oxide layer is still thin enough, the carriers will tunnel through barrier and the conduction changes to a more bulk limitted transport, because of the higher series resistance of the ZnPc layer plus the oxide barrier. The IV-curve shows a pure power law behavior, see Fig.3.9 a). With advanced degradation, the oxide layer will grow too thick for relevant tunneling and the carriers have to pass the insulator by Schottky emission over the barrier. With the information of the performed IV-measurements we can now

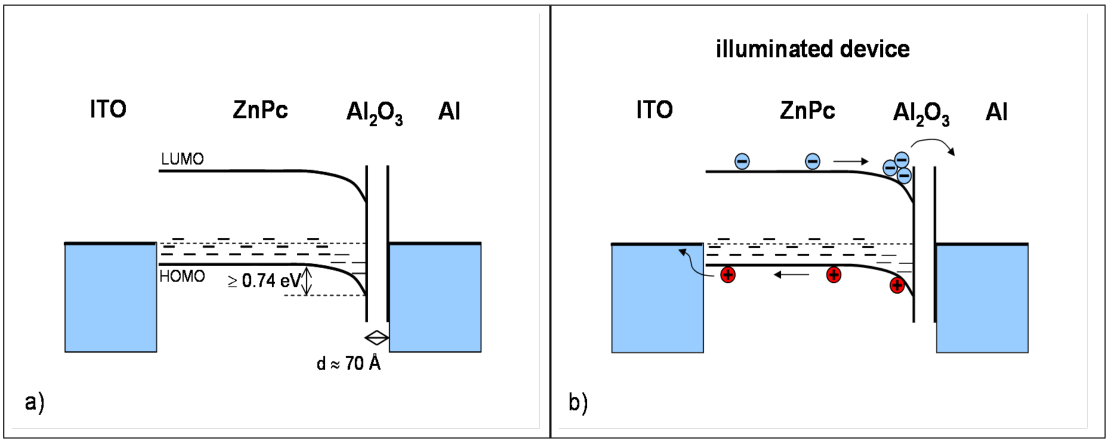

Figure 3.10: *a) Proposed energy level diagram of an ITO/ZnPc/Al_2O_3/Al device. b) Illuminated device in equilibrium. The aluminum oxide barrier causes the electrons to pile up at the ZnPc/Al_2O_3 interface and electron extraction is reduced.*

illustrate the assumed energy level scheme of the degraded device, as shown in Fig.3.10 a). Since there is no information about surface dipoles in the sample, the aluminum oxide layer is indicated by the two bars. A similar energy level diagram is assumed by Hiromitsu et al [71], who investigated Au/ZnPc/Al photovoltaic cells by electroabsorption and photocurrent measurements. The electroabsorption study reveals two inner electric fields, where one of them is attributed by the author to a Schottky-barrier at the Al/ZnPc interface and the second one to a dipole layer at the aluminum electrode. It is further assumed that the electric field of the dipole is directed parallel to the Schottky barrier field and that the origin of this dipole layer might be an oxide layer or a surface dipole. The consequence of such an oxide layer is not only Schottky emission conduction for holes in forward bias, but also a barrier for the electrons in the photovoltaic mode, see Fig.3.10 b). This amounts to a reduction of the photocurrent in the device. In Fig.3.9 b), the photocurrent in forward bias is presented together with the dark current, and obviously shows the same IV-dependence. We now compare the

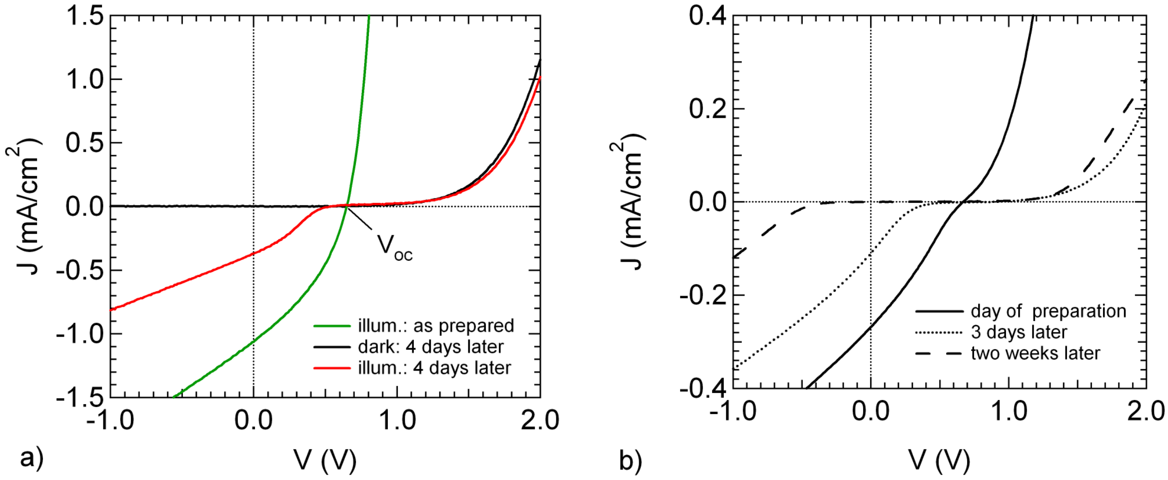

Figure 3.11: *a) IV-characteristics of the ITO/ZnPc(120nm)/Al cell in Fig.3.9 in the dark and under illumination (P ≈ 100 W) as prepared and 4 days later (in nitrogen atmosphere, 0.3 ppm oxygen) , b) IV-curves under illumination in a typical ITO/ZnPc(200 nm)/Al device.*

photocurrents in reverse bias of the as prepared sample with the degraded one (after four days in nitrogen atmosphere, 0.3 ppm oxygen). The degraded IV-curve becomes S-shaped in the fourth quadrant, as can be seen in Fig.3.11 a). This IV-behavior, also called “rollover” or “kink”, is generally explained with the existence of injection barriers at one of the contacts in heterojunction solar cells which can act as backward diodes [101, 102, 103]. However, the ITO/ZnPc/Al device already contains a Schottky contact at the Al/ZnPc interface, which means in order to explain the IV-behavior with a backward diode, we would have to assume a barrier at the ITO/ZnPc interface, that evolves with time. In any case this scenario seems rather unlikely. A straight-forward explanation can be given taking into account the results of the dark current degradation measurements. The build up of an oxide barrier at the aluminum contact can also be the origin for the kink in the photocurrent [2]. This can be explained as follows. The additional energy barrier from the oxide layer decreases significantly the slope

---

[2] The degradation due to an oxide barrier could be reproduced in by the drift and diffusion model of Wolfgang

of the forward dark and photocurrent. Obviously the photocurrent becomes zero when the flat band situation is reached at V $\approx$ V$_{oc}$, but due to the oxide barrier it has to follow the dark current in forward bias, which causes the photocurrent to be very weak between 0.6 V and 1.0 V. Since the oxide layer is a barrier for both types of charge carriers, the extraction of the electrons is hindered under short circuit conditions, as shown in Fig.3.10 b). This explains the reduced short circuit current of the degraded device. A long time degradation study of a similar ITO/ZnPc(200 nm)/Al-device shows that the "kink" in the photocurrent moves towards the negative bias voltages with further degradation. This behavior is illustrated in Fig.3.11 b) and is probably due to the increasing resistance of the growing oxide layer. If the insulation layer prevents the extraction of the electrons at the aluminum contact, the short circuit current would become zero. In the case that the resistance of the oxide exceeds the one of the ZnPc layer, the IV-characteristics would become more and more symmetric, because the oxide insulator has no rectifying character. We can observe this qualitative behavior in in Fig.3.11 b). From this results it can be concluded that the C_{60} protection layer alone cannot prevent a degradation of the sample. That can be satisfactorily explained by the oxidation of the Al contact. Therefore another encapsulation technique will be presented in the next section.

3.2.3 Encapsulation Revisited

Since the ITO/ZnPc/Al Schottky-barrier solar cells degrade even in nitrogen atmosphere (0.3 ppm oxygen) on a timescale of minutes to hours, the development of an effective encapsulation is essential for future experiments on intact devices. The degradation is assumed to result from the oxidation of the aluminum contact as described in the previous section. However, please note that the encapsulation presented in this section was not used in the following EDMR experiments, since it was developed afterwards. S-shaped IV-characteristics under illumination can identify degraded devices. For improved encapsulation a thin glass plate was glued on top of new ITO/ZnPc/Al -devices with a 200 nm C_{60}-protection layer (for details see § 3.2.2). Three different adhesives were tested for their suitability, two epoxy glues [3]:

Table 3.5: *Parameters of ITO/ZnPc/Al samples with 200 nm C_{60} protection layer and NOA 68 encapsulation*

Material	thickness [nm]	rate [Å/sec]	temp. [°C]	vacuum p. [mbar]
ZnPc	120	1.0	425	1.4×10^{-7}
Al	50	$\approx$ 2.5	1350	2.5×10^{-7}
C_{60}	200	0.9	525	0.9×10^{-7}

Tress. The theoretical calculations also show the kink in the photocurrent voltage behavior, when an additional barrier for electrons and holes is assumed at the Al-contact.

[3] The encapsulation study was supported by Nino Hatter

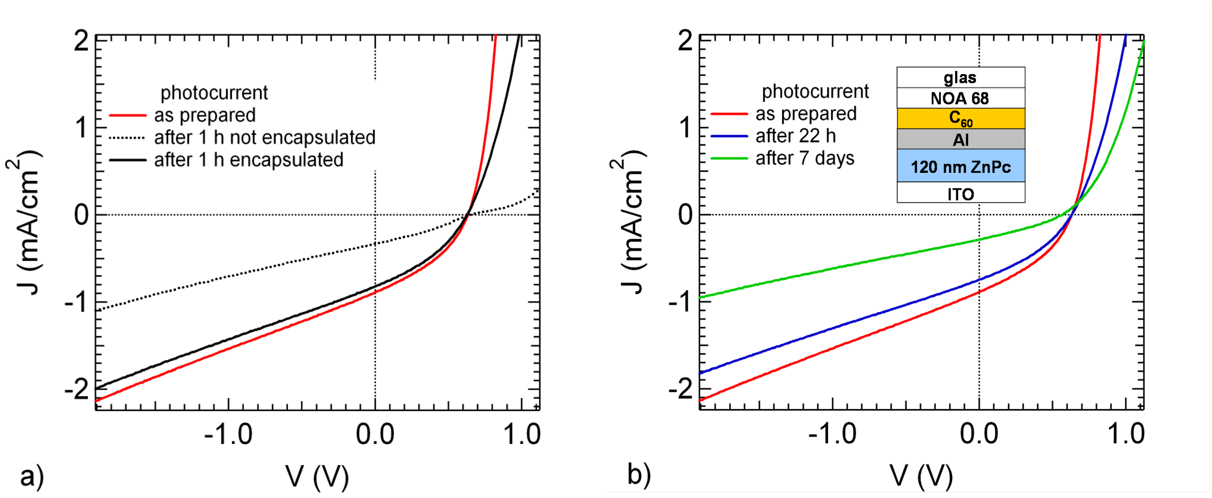

Figure 3.12: *a) Comparison of an ITO/ZnPc/Al - device with and without NOA 68 UV-glue encapsulation (both samples with a 200 nm* C_{60}*-protection layer). The IV-curves were taken in the glovebox setup described in § 2.4.1. b) IV-characteristics of the NOA 68 UV-glue encapsulated device. Illumination by a halogen lamp* (P≈100 W). *Note that the "kink" in the IV-curve under illumination shown in Fig.3.11 is absent in the encapsulated device.*

- Conrad No. 813337 two component glue
- UHU plus sofortfest two component glue

and one UV-glue:

- Norland optical adhesives NOA 68 UV-glue

Whereas the epoxy glues were not effective in sample protection, use of the UV-glue leads to a significant enhancement of the device-stability. The encapsulation was performed in a glovebox (0.3 ppm oxygen), where also the IV-measurements were performed. The preparation parameters are summarized in Table 3.5. In Fig.3.12 a) the photocurrent of the sample is shown immediately after preparation and one hour later. For comparison the photocurrent of another sample from the same production run without encapsulation is added in the plot. Whereas the encapsulated sample loses photocurrent of approximately 7 % (at V = -1 V) after one hour, the photocurrent of the device without encapsulation has already strongly degraded by 54 % and indicates S-shaped behavior. In Fig.3.12 b) a long time degradation study of the encapsulated device is illustrated. The encapsulation can prevent drastic photocurrent losses in the first 22 hours after fabrication, however for time periods of several days the photocurrent decreases by almost 60 %. Despite this current loss the kink in the IV-curve does not appear even after 7 days in the glovebox. This indicates that the main degradation process, associated with oxidation of the Al-contact, could be strongly reduced. The dark current behavior of the encapsulated sample, as shown in Fig.3.13 , confirms that the qualitative behavior of the IV-characteristics stays similar. The dotted lines in Fig.3.13 have the same slope and are a guide

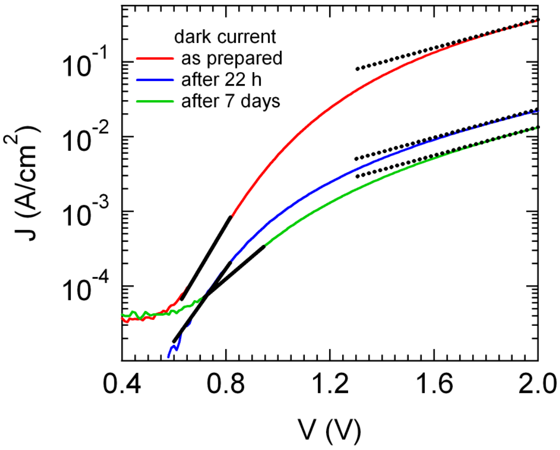

Figure 3.13: *Semilogarithmic plot of the dark IV-characteristics of the encapsulated ITO/ZnPc/Al sample of Fig.*3.12 b).

to the eye for the high voltage regime, whereas the black lines indicate different slopes in the low voltage regime. Neither Schottky emission nor space charge limited behavior is observed over the whole voltage range in the dark current, which is in contrast to the samples without encapsulation (see Fig.3.9). Since there is still a mechanism that leads to a current loss in the device, one might question whether this is another degradation mechanism or not. The decreasing slopes at low voltages might indicate that the aluminum oxidation is not entirely stopped. However, the electric conduction in phthalocyanine thin films is also influenced by the morphology of the material and we cannot exclude bulk degradation to be the origin of the remaining current loss. Such a bulk degradation might be due to recrystallization from the $\alpha-$ to the more stable β-phase of ZnPc. At room temperature evaporated thin films of ZnPc are usually in the α-phase [58] which shows higher conductivities than the β-phase [60]. However, the β-phase of ZnPc is thermodynamic stable at room temperature. X-ray diffraction measurements would be necessary to answer the question if recrystallization is the origin of the remaining degradation mechanism.

3.2.4 Discussion and Conclusions

In chapter 3 we investigated the charge transport in ZnPc thin film devices with different electrode geometries and materials. It has been demonstrated that at low voltages (0 - 50 V) coplanar gold contacts provide ohmic contacts to ZnPc, whereas at higher voltages SCL currents dominate the transport mechanism. However, even at high voltages (V = 150 V) the device is still in a transition regime between ohmic and SCLC behavior. The IV-temperature dependence indicates an exponential trap distribution in the bandgap of ZnPc and a Fermi-level position 0.3(1) eV above the HOMO. In combination with the rather high conductivity value $\sigma = 2 \times 10^{-7} \Omega^{-1}\mathrm{cm}^{-1}$, this could be evidence for doping due to oxygen related impurities in the sample, which is frequently reported for phthalocyanine thin films [65, 66, 60, 6]. Under illumination, the device current increases by a factor of approximately $J_{ill}/J_{dark} \approx 2.4$. In general, it is assumed that the photoexcitation in organic materials leads to rather strongly bound excitons that have to be separated by intense electric fields, which can only be provided by hetero interfaces or space charge regions. However, the clearly enhanced photoconductivity in the coplanar device indicates that photoinduced excitons can dissociate into free carriers without the strong electric fields of a rectifying contact. This type of charge carrier generation can be explained by the interaction of excitons with impurity- or defect sites in the bulk material, as proposed by A. J. Twarowski [104]. The presence of trap levels and enhanced photoconductivity in the coplanar Au/ZnPc/Au devices leads to the conclusion that this charge carrier generation model is applicable for these samples.

In the ITO/ZnPc/Al sandwich devices, a Schottky barrier at the aluminum contact can satisfactorily explain the rectifying behavior of the dark current and the generation of the photocurrent. Here it is assumed that the electric field of the Schottky barrier accelerates the charges towards the electrodes. Whether this electric field also leads to exciton separation depends on its strength. In order to determine the electrical field strength the width of the space charge region has to be known. If we assume $N_V = 10^{27} m^{-3}$ for the density of states in the valence band [92], we can calculate the acceptor density N_A in the material via the simple relation [105]:

$$N_A = N_V exp\left(\frac{E_F - E_V}{k_B T}\right) \tag{3.10}$$

With E_F - $E_V \approx$ - 0.3 eV we get $N_A \approx 10^{22}$ m^{-3} for the acceptor density, which is in adequate agreement with the reported trap densities of 10^{18}-10^{26} m^{-3} [6]. Inserting this density value in the equation for the width of the depletion region,

$$W = \sqrt{\frac{2\varepsilon_0\varepsilon_r V_{bi}}{eN_A}} \tag{3.11}$$

we get an extended space charge region at zero applied bias of W $\approx$ 156 nm. Here we used a dielectric constant ε_r = 3 [63] and V_{bi} = 0.74 V, see § 3.2. The consequence of this result is that the space charge region is spread over the whole ZnPc layer, resulting in rather low electric fields in the order of 10^6 V/m. Since the exciton binding energies in phthalocyanine are approximately 0.6 eV [106], and typical electron hole distances in excitons are in the order of 1.5 nm [107], field strength of 10^8 V/m would be required for efficient exciton splitting. We can assume from these results that charge carrier generation probably occurs at defects or impurities throughout the whole bulk material of the ZnPc-film. The rather steep slope of the photocurrent indicates strong differences in the mobilities of electrons and holes. It is therefore assumed that some of the photogenerated electrons are not able to reach the extracting aluminum electrode within their lifetime, which may lead to trapped charge carriers throughout the ZnPc layer. At higher voltages, SCLC with exponential trap distribution is observed, which also supports the results from the coplanar Au/ZnPc/Au devices.

The degradation studies show that even in nitrogen atmosphere with 0.3 ppm residual oxygen the aluminum contact starts to oxidize within minutes. The oxidation leads to a Schottky emission behavior of the dark IV-curve and a kink in the IV-characteristics under illumination combined with a remarkable loss in the short circuit current. Both effects can be prevented by an effective encapsulation against the residual gas by using UV-glue and a glass plate.

Chapter 4

Spin Dependent Transport in ZnPc

This chapter is supposed to gain first insight in the spin-dependent transport in phthalocyanine by means of continuous wave (cw) EDMR. To our knowledge, EDMR measurements in phthalocyanine material have been done so far only by Hiromitsu et al. in H_2Pc/C_{60} and $CuPc/C_{60}$ solar cells [20, 32]. Two EDMR signals were found that were both attributed to spin-dependent recombination of exchange-coupled electron-hole pairs at different recombination centers. One of the components showed spin flip satellites that were assumed to stem from the protons in phthalocyanine [32]. However, in a later publication the same EDMR signal with spin flip satellites was observed in pure C_{60}-devices[20]. It is not clear whether either of the EDMR-signals found in H_2Pc/C_{60} solar cells originates from phthalocyanine.

The chapter begins with a confrontation between the cw EDMR results of the coplanar and the sandwich type ZnPc device. In a first step the bulk transport dominated coplanar device is analyzed. Further studies in the sandwich type ITO/ZnPc/Al sample concentrate on the influence of barriers and degradation on the EDMR signal. In the following discussion a model based on spin-dependent recombination is proposed to explain the results. This model is further supported by saturation measurements and voltage dependent measurements. Furthermore the influence of exchange coupling on the EDMR lineshapes will be analyzed with the help of a phase analysis. In the last section, a magnetoresistance effect in ZnPc is discussed on the basis of the EDMR results.

4.1 Bulk Transport vs. Injection Limited Transport

4.1.1 EDMR in Coplanar Au/ZnPc/Au Devices

The coplanar device permits the investigation of spin-dependent processes without transport dominating barriers. As a result the assumption can be made that the EDMR probes the processes in the ZnPc bulk material.

The Au/ZnPc(300 nm)/Au coplanar device contains of a 34 finger interdigitated electrode array with 30µm gaps. Details about the device fabrication are given in § 2.3.1. Furthermore it was found in § 3.1 that coplanar gold electrodes provide ohmic contacts to the ZnPc layer, showing ohmic IV-characteristics at low voltages that change to space charge limited currents in the high voltage regime. We performed continuous wave EDMR at the coplanar sample using a Keithley 230 voltage source and a Femto DLPCA-200 current amplifier (10^5 V/A). The current changes through the device under resonant microwave conditions are displayed in Fig.4.1 a) and show a current quenching. The EDMR signal is exclusively observed under illumination, which is supported by the light intensity study shown in Fig.4.1 b), where the EDMR signal amplitude varies almost linearly with the light intensity.

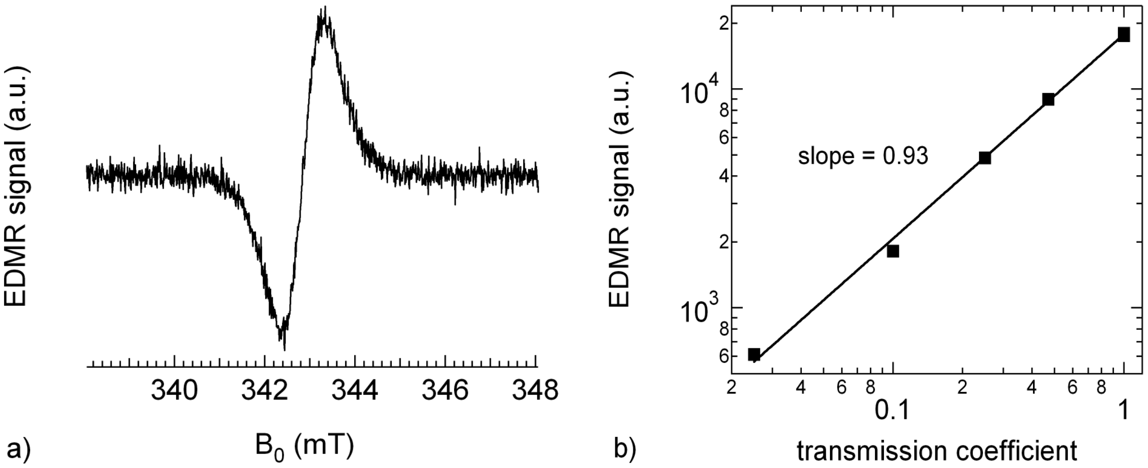

Figure 4.1: *a) EDMR spectrum of an Au/ZnPc/Au device under illumination with a halogen lamp (LOT Oriel, P ≈ 100W). During the measurements a voltage of V = 100 V was applied to the sample and the modulation amplitude and frequency of the magnetic field were* A_{mod} *= 0.7 mT and* f_{mod} *= 10 kHz respectively. The signal shows a current quenching.* b) *Light intensity dependence of the EDMR signal amplitude in the Ohmic IV-regime (V = 50 V) . The halogen lamp (LOT Oriel, P ≈ 200W) was attenuated by neutral glas filters (Schott NG) with different transmission coefficients. The EDMR signal intensity varies almost linear with the light intensity.*

Discussion of The Spin Dependent Transport

The most prominent spin dependent processes that influence the current in organic devices are polaron recombination and bipolaron formation. In general, the rates of these processes are enhanced during resonant microwave excitation and it is therefore assumed that recombination leads to a current quenching because of the annihilation of charge carriers associated with this process. Since Bipolarons are assumed to be less mobile than polarons the bipolaron formation is also assumed to be a current quenching process. We want to discuss the EDMR results of ZnPc in the picture of spin-dependent recombination for the following reasons. The Au/ZnPc/Au sample is supposed to be a hole-only device, since the workfunction of the Au electrodes (ϕ_{Au} = 5.2 eV) is similar to the ionization energy of the hole conducting ZnPc layer (E_{Ion} = 5.28 eV [63]) and therefore supports hole injection. Here we refer to the device characterization given in chapter 3. Without illumination, the electron concentration in this device is thus very low. However, upon illumination electrons from the HOMO are excited into the LUMO and recombination becomes crucial. From this argument, we can understand why the EDMR signal is only present under illumination, whereas bipolaron formation should be readily observed in the dark current EDMR. Since recombination is a limiting process for the photocurrent it is also evident that the EDMR signal is current quenching in this device.

4.1.2 EDMR in ITO/ZnPc/Al Sandwich Devices

In chapter 3 the dramatic influence of the electrodes and the degradation to the current transport in sandwich type ITO/ZnPc/Al devices was demonstrated. Whereas the coplanar ZnPc device is dominated by bulk transport, the current in the sandwich device is controled by a Schottky barrier. Upon degradation an additional oxide barrier limits the transport of the electrons and holes in the device. In this section the correlation between the EDMR signal and the transport limiting barriers will be investigated in the sandwich type ZnPc device.
The sample preparation and encapsulation was carried out as described in § 2.3.2. The parameters for the physical vapor deposition of ZnPc and aluminum can be found in Table 4.1. We used 200 nm ZnPc layer thickness for the EDMR samples, in order to avoid short circuits from metal diffusion into the organic material. EDMR experiments were performed with a Stanford Research Systems battery voltage source SR SIM928 and a SR 570 current amplifier (1V/µA), details are given in § 2.4.2. The EDMR signal of the ITO/ZnPc/Al device is shown in Fig.4.2 together with the signal of the coplanar device. The signal amplitudes and signs were matched for better comparison. Line width, line shape and g-value of the signals coincide and lead to the assumption that both signals have their origin in the ZnPc layer. Interestingly, the signs of the two EDMR signals do not coincide and had to be matched in Fig.4.2. In the following a possible origin for this sign reversal will be discussed in the context of current limiting space charges.

Table 4.1: *fabrication parameter for ITO/ZnPc/Al-EDMR-samples*

Material	thickness [nm]	rate [Å/sec]	temp. [°C]	vacuum p. [mbar]
ZnPc	200	1.0	450	2 x 10^{-7}
Al	50	$\approx$ 2.5	1350	3 x 10^{-6}

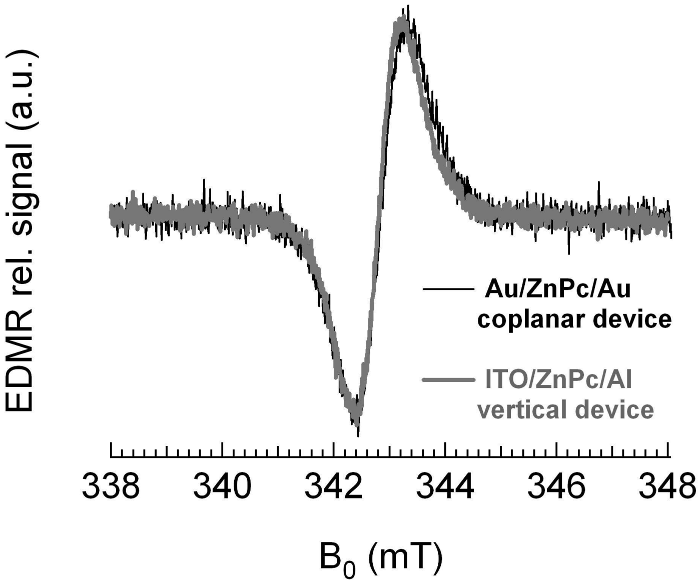

Figure 4.2: *EDMR signals of the Au/ZnPc/Au coplanar device and the ITO/ZnPc/Al sandwich device. The amplitudes and signs are matched for comparison. Both signals where recorded under illumination (P $\approx$ 100 W) with a microwave intensity of P_{mw}= 20 mW and modulation frequency of f_{mod}= 10 kHz.*

Discussion of the Spin-Dependent Transport

In general polaron recombination leads to a current quenching EDMR signal, as mentioned in § 4.1.1. However, under specific circumstances, this process can show the opposite sign. Solomon [108] found that spin-dependent recombination in a forward biased p-n diode may lead to a current enhancement, when recombination limited currents are assumed. Furthermore Lips and Fuhs [109] and Brandt [19] found that in the presence of space charge limitted currents a spin-dependent recombination signal can reverse it's sign from negative to positive. The IV-analysis in chapter 3 has shown that space charges play a minor role in the coplanar ZnPc device if moderate voltages ($V < 150V$) are applied to the sample. This situation changes dramatically in the ITO/ZnPc/Al-Schottky-device. Here space charges may play an important role in the vicinity of barriers that control the current in this device. We recorded IV-curves of the samples after preparation in the glovebox-setup (§ 2.4.1) and before the EDMR experiment in the Bruker spectrometer (sec 2.4.2). The dark and photocurrent of a typical EDMR sample is shown in Fig.4.3 a). The diode-like IV-curve in the dark and the photocurrent can be explained by a Schottky-barrier at the aluminum contact, as discussed in sec 3.2. The inset shows that the dark current becomes space charge limited above V = 0.8 V. The device presented in Fig.4.3 b) already degraded prior to the EDMR measurements. The dark current shows Schottky-emission behavior as illustrated in the log J vs. $V^{1/2}$ presentation of the inset and the photocurrent is very weak. The S-shaped behavior shown in § 3.2.2 has vanished during further degradation. From these results we can assume that the resistance of the oxide

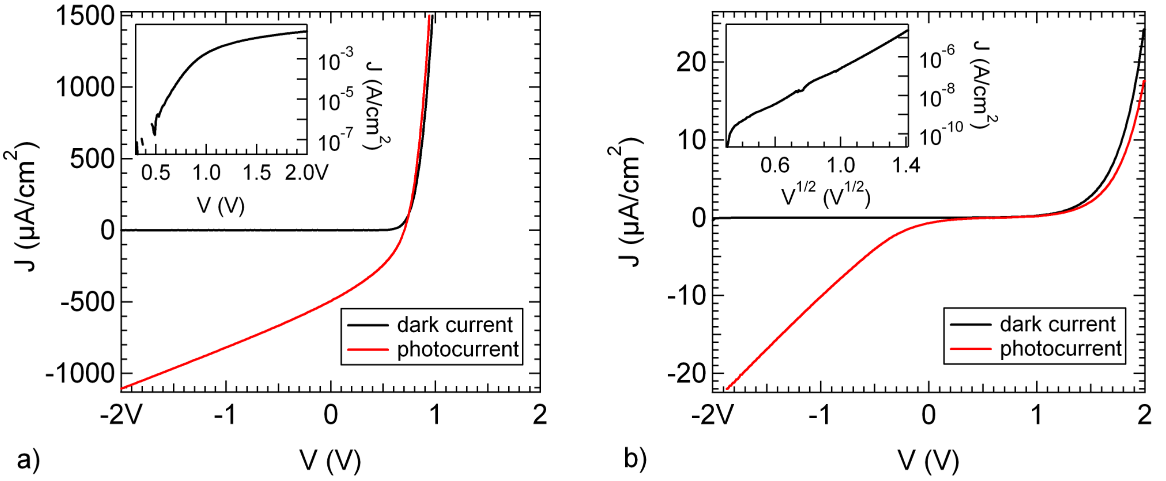

Figure 4.3: *a) IV-characteristics under illumination with a halogen lamp (P ≈ 100 W) and in the dark of a typical ITO/ZnPc(200nm)/Al EDMR-sample directly after preparation.* A voltage of V = -2 V was applied in reverse bias direction. *The inset shows the dark IV-curve in a semilogarithmic plot. b) IV-characteristics directly before EDMR-measurement (similar illumination conditions), the inset shows the dark IV-curve in Log J vs. $V^{1/2}$ presentation.*

layer plays a dominant role in the device. Since the EDMR sample had suffered degradation

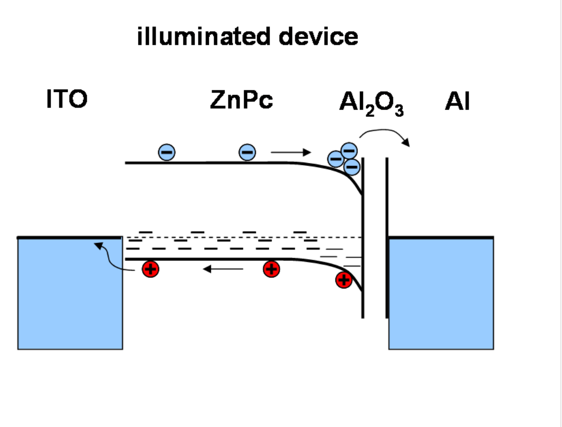

Figure 4.4: *Proposed Energy level diagram of an illuminated ITO/ZnPc/Al_2O_3/Al device in equilibrium. The aluminum oxide barrier causes the electrons to pile up at the ZnPc/Al_2O_3 interface and electron extraction is reduced. Enhanced recombination near the ZnPc/Al_2O_3 interface might reduce these accumulated space charges and thus enhance the photocurrent.*

we can expect a situation as depicted in Fig.4.4. It has been found in §3.2.2, that during degradation an oxide barrier is formed at the aluminum electrode. This oxide layer may cause an extraction barrier for the electrons in reverse bias as well as under short circuit conditions. If the electrons pile up at the ZnPc-insulator interface, they build up a space charge that alters the electric field of the Schottky barrier. As a result the carrier extraction will be further reduced by the electric field of the accumulated space charge and thus the photocurrent will be limited. In this situation, recombination of trapped electrons with holes near the oxide layer would reduce these limiting space charges. As a result the enhanced recombination during EDMR would lead to an increasing photocurrent as observed in the experiment. This model will be further supported by voltage dependent EDMR measurements in § 4.3.

4.2 EDMR Signal Saturation

In this section, the EDMR signal saturation of the ZnPc sandwich device will be discussed in the theoretical frame of the polaron encounter model, developed by T. Eickelkamp [21]. The EDMR signal saturation differs significantly from the one observed in EPR. In magnetic resonance experiments the microwave radiation tends to equalize the population of the spin levels whereas the spin-lattice relaxation tries to maintain the thermal equilibrium. If the microwave field is too strong, the population of the levels are equalized and the sample does not absorb anymore, which means that the EPR signal vanishes. Since in an EDMR experiment we do not measure the absorption of the sample, but the relative singlet to triplet ratio of a spin pair ensemble, high microwave power does not lead to a decrease of the signal. However, the EDMR signal still saturates with a characteristic saturation behavior given by [21]:

$$S(P_{mw}) = \frac{AP_{mw}}{1+BP_{mw}} \tag{4.1}$$

where P_{mw} is the microwave power and A and B are parameters that depend on recombination- and dissociation-rates as well as the spin relaxation time T_1. The saturation behavior of the EDMR signal was investigated in ITO/ZnPc/Al devices. Fig.4.5 shows that the EDMR signal strength vs. the microwave power reflects the saturation behavior expected in the polaron encounter model as calculated by T. Eickelkamp et al. [21]. The model is based on the assumption that non geminate polarons form a radical pair state with considerable lifetime before they dissociate or recombine spin-dependently. Light excitation will lead to excitons in the organic film that can be split into positive and negative polarons. These polarons may migrate through the film and reencounter to form a polaron pair with a random spin state that may be a singlet (S = 0) or a triplet state (S = 1). The polaron reencounter model is in agreement with our previous assumptions, that the origin of the signal is due to a recombination mechanism (see § 4.1.1).

4.3 EDMR at Different Voltages

Voltage dependent EDMR measurements can be used for probing the recombination model of accumulated charges discussed in § 4.1.1 at different working conditions in the device. This can provide insight into the nature of the process and at which conditions it is active. The voltage dependence of the EDMR signal is investigated in the ITO/ZnPc/Al device introduced in

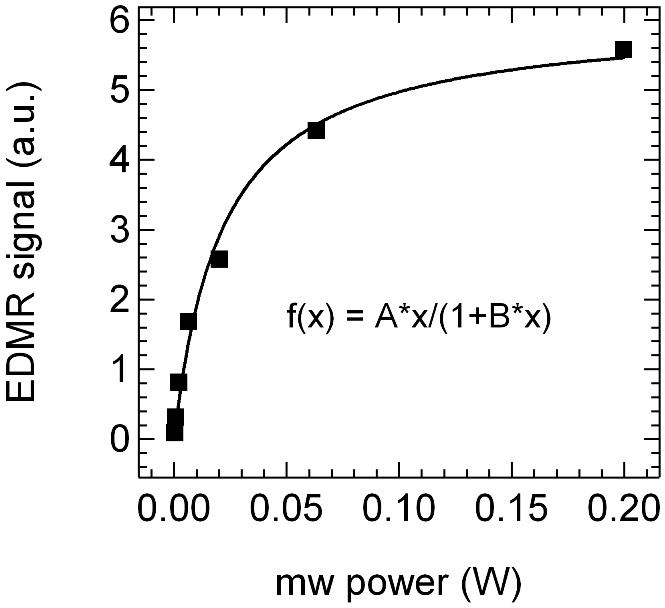

Figure 4.5: *EDMR saturation of an ITO/ZnPc/Al device. The signal was recorded under illumination of a halogen lamp ($P \approx 100$ W) and an applied voltage of V = -1 V, in reverse bias. The fit function reflects the expected behavior in the polaron encounter model.*

§ 4.1.2. In Fig.4.6 the EDMR amplitude is shown together with the IV-characterization under the same illumination conditions. We used a modulation frequency of f_{mod} = 10 kHz and amplitude of A_{mod} = 0.5 mT in all measurements and varied the voltage randomly, in order to reduce the influence of degradation as a systematic error. The chronological order of the measured data points is indicated by the numbers. We measured the EDMR signal at V = -2 V three times to gain an estimate for the error during the measurement. Obviously the EDMR amplitude is not proportional to the photocurrent in the device, but is nearly constant over a voltage range from V = -2 V to V = +1 V. The signal is current enhancing in this voltage regime but changes to a current quenching at higher forward biases.

We can explain this behavior by taking into account the influence of the oxide barrier discussed in § 4.1.1. This barrier hinders the extraction of electrons as long as the current flow of the electrons is directed towards the aluminum electrode, which means from negative biases up to V_{OC}. Under these conditions electrons will pile up at the oxide layer as shown in Fig.4.7 a) and further reduce the extraction. The effect of magnetic resonance enhances the recombination and reduces the amount of accumulated space charges. As a consequence the current enhances in the EDMR experiment. At higher forward biases the current will change it's direction and the LUMO becomes flat, as illustrated in Fig.4.7 b). Under these conditions there is no sink where the electrons can pile up and when magnetic resonance is applied to the sample enhanced recombination will only reduce the charge carriers and thus the current in the device. This means that under under high forward biases, the sample is comparable to the Au/ZnPc/Au device were also a quenching EDMR signal was found.

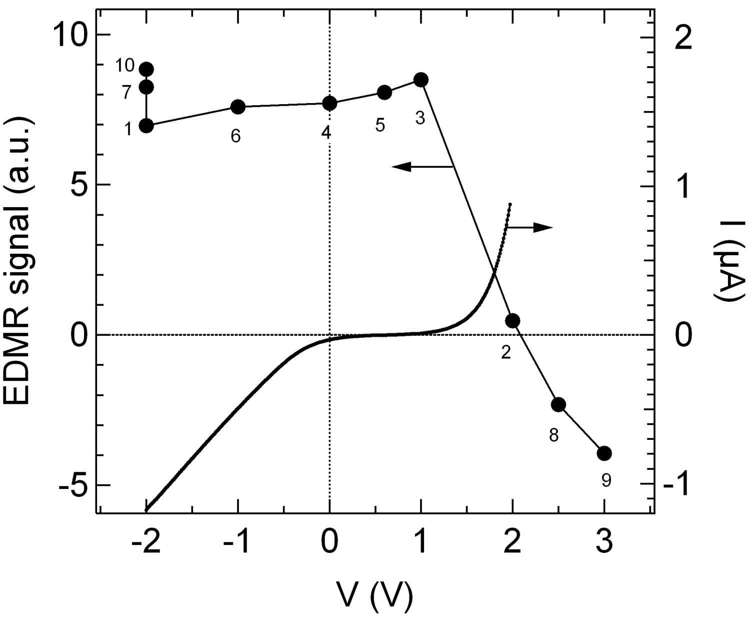

Figure 4.6: *voltage dependent EDMR amplitudes (ΔI) of an ITO/ZnPc/Al device under illumination of a halogen lamp ($P \approx 100$ W). To exclude degradation dependent signal changes, the chronological order of the measurements is indicated by the numbers. For comparison the IV-curve under the same illumination conditions is plotted in the graph.*

4.4 The Role of Exchange Coupling in ZnPc

In this section continuous wave EDMR spectra of ZnPc thin film devices are discussed in the context of exchange coupling. Since in general the EDMR method is sensitive solely to processes that involve pairs of spins that react with another in a specific way (recombination, bipolaron formation, ...), it is intuitive to expect also two resonances in the spectrum. However, it is frequently observed that the spectrum consists only of one peak [20, 110, 111] and the following explanations can hold for this:

1. The resonance positions of the two spins are almost the same and cannot be resolved in the spectrum.
2. One of the two resonance lines is extremely broadened and therefore only one of the species can be manipulated effectively by EPR.
3. The exchange interaction between the spins of the pair leads two a new spin state basis with four energy levels. In the case of strong exchange coupling, the resulting spectrum contains a strong center peak and two very weak satellite lines and may thus look like a single resonance line.
4. The Radical triplet quenching mechanism [112] may lead to a spectrum with one strong spin 1/2 peak and a weak triplet pattern. If the triplet pattern is only observed at low temperatures, this would also lead to one resonance line at room temperature.

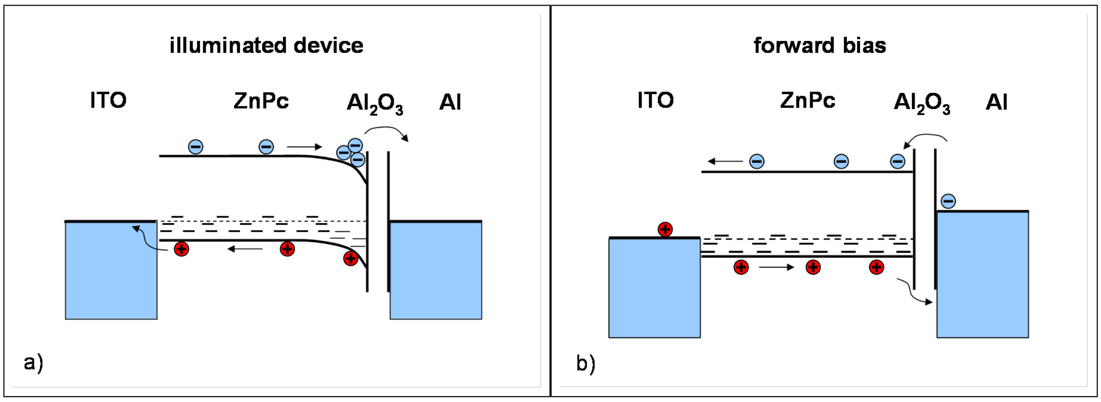

Figure 4.7: *a) energy level diagram suggested for an illuminated ITO/ZnPc/*Al_2O_3*/Al in equilibrium. Electrons pile up near the ZnPc/*Al_2O_3 *interface. b) Forward bias near the flatband condition. The accumulated electrons are released.*

The following discussion of the cw EDMR-results for Au/ZnPc/Au devices will focus on the aspects No. 1 and 3, whereas the possibilities No. 2 and 4 will be treated in the context of the pulsed EDMR results.

4.4.1 Discussion of The Lineshapes

The EDMR lineshapes will be discussed with respect to the signal of the coplanar device introduced in § 4.1.1, where also the experimental conditions are described. In this device the photocurrent quenches when the resonance condition is fulfilled, as can be seen in Fig.4.8 c). A careful analysis shows that it is insufficient to fit the spectrum with a single Gaussian or Lorentzian line, indicating that the resonance contains more than one component. As mentioned above, from the spin-pair model one would expect the two resonances of the pair.

In a first approach we can assume a simple superposition of two resonance lines, which would mean that the spectral positions and therefore the g-factors of the components are almost the same (according to explanation No. 1). This situation is illustrated in Fig.4.8 a). A fit function composed of two Gaussian lines in fact fits the experimental data sufficiently, as can be verified in Fig.4.8 c) (red line). However if exchange coupling is assumed within the spin pair, the spectrum will contain four transition lines. When the coupling constant J is larger than the Larmor separation $\delta\omega$, the two inner lines become equal, whereas the outer lines are very weak and equally spaced by J. The resulting lineshape looks like a single Gaussian line which is broadened at the foot of the resonance due to the weak satellites, see § 1.4.2. Since we cannot exclude exchange coupling at this stage the spectrum was fitted with a function composed of a centre line and two equally spaced satellites according to explanation

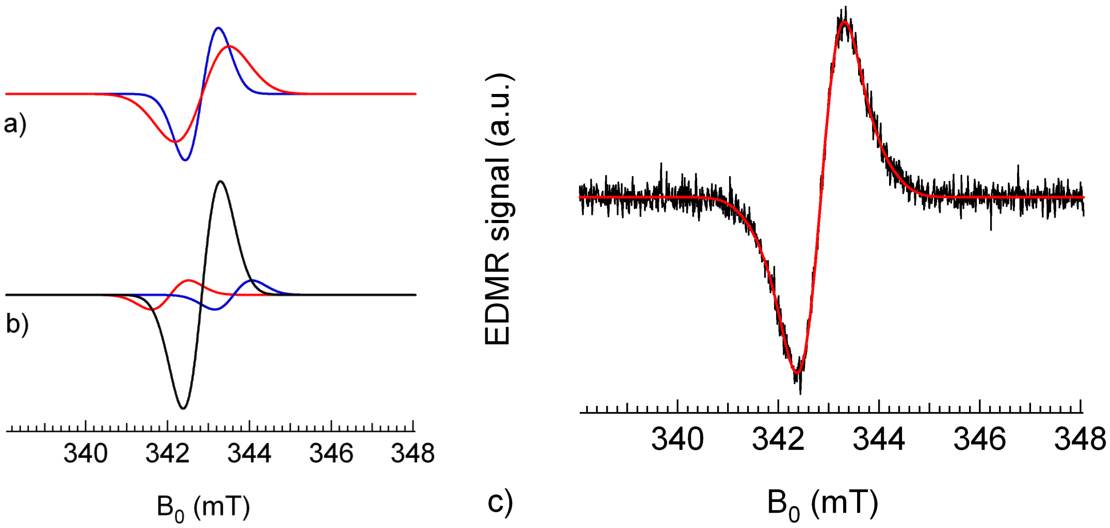

Figure 4.8: *a) decomposition of the fit function in the case of exchange coupling. b) fit function in the absence of exchange coupling composed of two Gaussian lines. c) EDMR signal (open circles) at a microwave power of $P_{mw} \approx$ 20 mW in an ITO/ZnPc(200 nm)/Al device at V = -2 V under illumination (P ≈100W). A lock-in modulation frequency of f_{mod} = 10 kHz and A_{mod} = 0.5 mT modulation amplitude were used in this experiment. Both cases, a) with and b) without exchange coupling, lead to indistinguishable good fit results indicated by the red line.*

No 3. The fit function indicated in Fig.4.8 b) reads:

$$f_{exchange} = \underbrace{-\frac{2A(x-C)}{\Delta B^2} \quad exp\left[\frac{-(x-C)^2}{\Delta B^2}\right]}_{center}$$
$$\underbrace{-\frac{2B(x-C+J)}{\Delta B^2} \quad exp\left[\frac{-(x-C+J)^2}{\Delta B^2}\right] - \frac{2B(x-C-J)}{\Delta B^2} \quad exp\left[\frac{-(x-C-J)^2}{\Delta B^2}\right]}_{satellites}$$

where A and B are the amplitudes of the center line and the satellites respectively, C is the resonance position of the center line and ΔB is the line width of all components. J denotes the exchange coupling constant as introduced in Eq.1.20. The resulting fit (red line in Fig.4.8 c)) cannot be distinguished from the fit function with two Gaussian lines. All the

Table 4.2: *cw EDMR fit results for the ITO/ZnPc/Al device in Fig.*4.8.

fit function	FWHH ΔB (mT)	FWHH ΔB (mT)	g_a	g_b	J (mT)
a) exchange coupl.	ΔB = 1.07	ΔB = 1.07	2.0009(5)	2.0034(5)	0.77
b) no exchange coupl.	ΔB_a = 0.95	ΔB_b = 1.56	2.0022(5)	2.0021(5)	0

fit-parameters can be found in Table 4.2. The g-value g_a and g_b can be calculated from the ratio A/B of the center line amplitude to the satellite amplitude which yields the value of $\varphi = 1/2 \quad arctan(J/\delta\omega)$. In general the EDMR g-values measured in ZnPc varied from sample to sample by $\approx 5x10^{-4}$, however the separation of two g-values in one measurement are much more precise. Since the presence of exchange coupling cannot be clarified from the spectra alone a phase analysis will be attempted in the following section.

4.4.2 Lock-In Phase Analysis

In this section the decomposition of the EDMR signal with respect to the role of exchange coupling will be investigated with the help of a phase analysis. When using a phase sensitive lock-in detection, the EDMR signal contains in addition to its amplitude a signal phase, that is the signal is rather a vector than a scalar. Under specific circumstances it is possible to extract the components of an EDMR signal by varying the lock-in detection phase. If the components of the signal have different phases with respect to the detection phase, as illustrated in Fig.4.9, there will be a detection phase setting at which the components have different signs and can thus be separated.

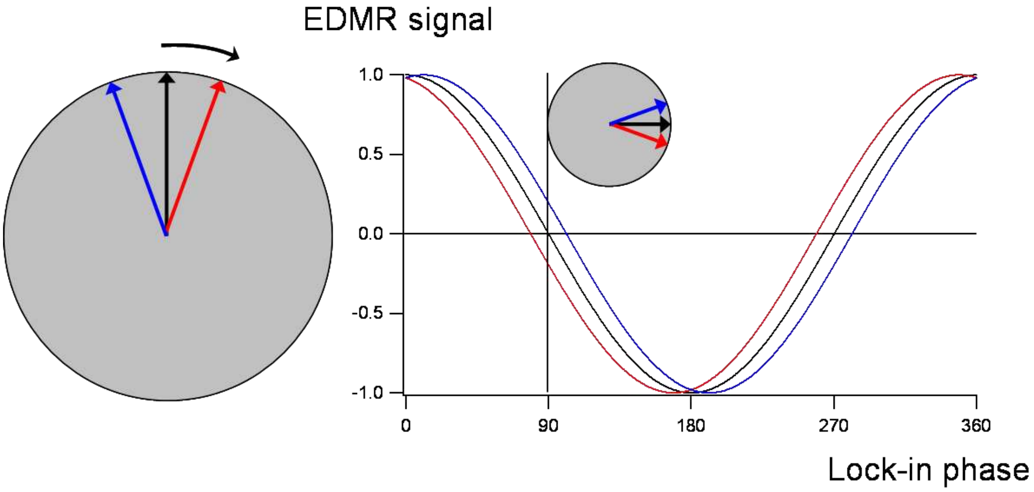

Figure 4.9: *Illustration of the lock-in phase in an EDMR experiment. If the components (red, blue) have different phases with respect to the detection phase (black). It is possible to find a lock in phase (here 90°), where the components have different signs, or where one of the components has zero amplitude.*

We applied EDMR at 90° lock-in phase to the coplanar Au/ZnPc/Au device. The resulting spectrum shown in Fig.4.10 indeed shows two signals with opposite sign. A fit function composed of two Gaussian lines with almost identical resonance positions could sufficiently reproduce the spectrum, where the negative signal exhibits a broader linewidth than the positive. Note that the different signs of the components originate from the lock-in phase and cannot be interpreted as signs in the current changes. The fit parameters can be found in Table

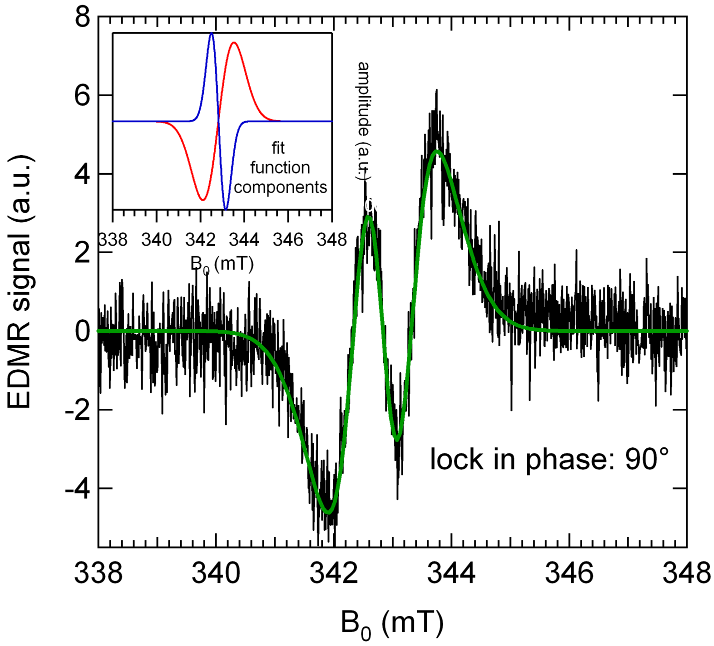

Figure 4.10: *EDMR at 90° lock-in phase at the coplanar Au/ZnPc/Au device in Fig.4.2. The spectrum was recorded under illumination (halogen lamp, $P \approx 100$ W) and a voltage of $V = 100$ V was applied to the sample.. A microwave power of $P_{mw} \approx 20$ mW was combined with a modulation amplitude $A_{mod} = 0.5$ mT and frequency $f_{mod} = 10$ kHz in this experiment.*

Table 4.3: *fit parameters of the 90° phase EDMR signal in Fig.*4.10.

90° phase EDMR signal	g-factor	FWHH ΔB (mT)	sign at 90°
component a	2.0022(5)	0.8	positive
component b	2.0022(5)	1.7	negative

4.3 and are similar to the ones in Table 4.2 from the 0° phase measurement [1].

The cw EDMR linewidth of the two components was measured as a function of microwave power. The result is illustrated in Fig.4.11. The cw EDMR signal was taken at a lock-in phase where the components were separated. This particular phase had to be readjusted for each measurement. The signal was recorded at two slightly different phases for each mw-power and the difference can thus be taken as an indication of the absolute error. The experiment shows that whereas the linewidth of component A is almost constant, that of component B increases with increasing mw-power. This result indicates different dynamics of the two signal components.

---

[1] Further lock-in phase studies on bilayer ZnPc/C_{60} are reported by S. Saremi [129].

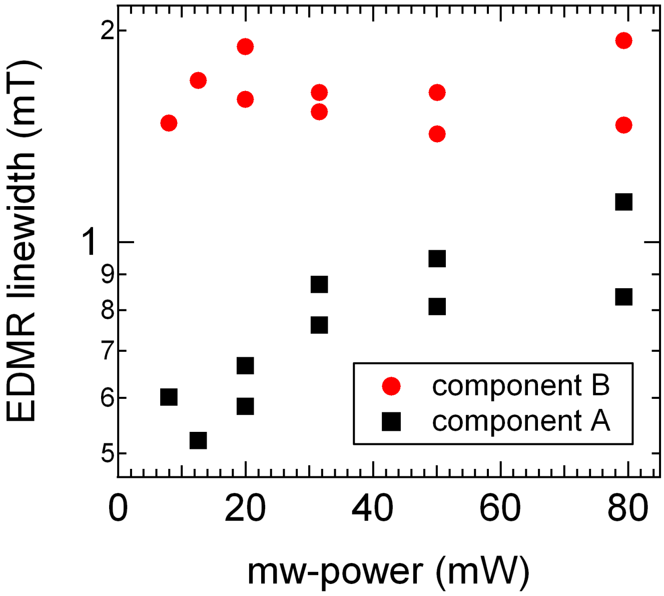

Figure 4.11: *C.w. EDMR linewidth of a coplanar Au/ZnPc/Au signal measured at different microwave powers. The components were separated at a particular lock-in phase that had to be readjusted for each measurement. At most mw-powers, two signals at a slightly varied lock-in phase were recorded, so that the difference can be taken a measure of the absolute error.*

Discussion

From the phase analysis we can conclude that the fit function including exchange coupling in § 4.4.1 is not adequate to describe the EDMR-spectrum in ZnPc. Consequently the EDMR spectrum consists of a simple superposition of two resonance lines, which could be attributed to the positive and negative carrier in a recombination process. In any case, in order to draw the right conclusion about this experimental result, we have to discuss the origin of the phase shift. Two possible explanations are considered in the literature, which refer to either different spin relaxation times (T_1) [22, 113] or to different reaction times (hopping or recombination times) [18, 19, 114]. The former explanation offers the possibility, that the spins in a pair have different relaxation times. As consequence of this, the components could be attributed to the oppositely charged carriers of a recombining spin pair, as proposed by Graeff [22]. However, the latter explanation would exclude the possibility of separating the spin partners of a single spin pair, because the pair spins should have a common recombination time. In this case the possibility must be taken into account that the two components are due to different spin-dependent processes. In this case, each component comprises a pair of spins and no conclusion about the exchange coupling can be drawn. The distinct powerbroadening of the components linewidth indicates different dynamics of the two signals, see Fig.4.11. In the polaron reencounter model, the EDMR signal linewidth depends on the parameter

$$\frac{1}{T_c} = \sqrt{\left(\frac{1}{T_s} + d + \frac{r_s}{4}\right)\left(\frac{1}{T_s} + \frac{d^2 + d\frac{r_s}{2}}{d + \frac{r_s}{4}}\right)} \qquad (4.2)$$

where T_s is a relaxation time that comprises a spin-lattice relaxation (T_1-process) as well as coherence decay (T_2-process) in the spin pair. Note, that a common relaxation time is proposed for both spins. Since T_c is a function of the recombination rate r_s, the dissociation rate d and T_s, it is an expression of the reaction dynamics and relaxation of the spin-dependent recombination. Following this model, the distinct $\frac{1}{T_c}$ rates of the EDMR signals are tentatively ascribed to different spin-dependent processes. The g-factors of the components are equal (g_a= g_b= 2.0022(4)) and near to the lower g-values in Table 2.2 that is ascribed by some authors to the cation in ZnPc, see § 2.2. However, if exchange coupling is weak, we have to consider equal g-values for the positive and the negative polarons in ZnPc to explain the spin-dependent recombination.

4.5 Magnetoresistance in ZnPc

Currently magnetoresistance measurements in organic materials gains more and more interest [1, 33, 115, 116]. A large magnetoresistance effect in the order of % can be observed even without ferromagnetic contacts. This effect cannot be explained by the classical magnetoresistance process, which assumes that the magnetic field causes periodic cyclotron orbits for the electron transport path [117]. Different models have been proposed so far for the magnetoresitance in organic devices and they are based on the magnetic field effects on either electron-hole pair recombination- or dissociation-rates [116, 118], or on bipolaron formation-rates [119, 120]. Arguments for the bipolaron model are magnetoresistance effects measured in unipolar devices [121, 122], where only one type of carrier (either the electron or the hole) is present. On the other hand, magnetoresistance was found to be only present under illumination in solar cell devices [123], which requires the electron hole pair model. Here we want to investigate the correlation between EDMR and magnetoresistance, since the effects are based on similar assumptions. In this context we do not want to rule out one of the models in general, but rather find out if one of them is applicable to our results. The magnetoresistance measurements were carried out on the coplanar Au/ZnPc/Au device under illumination of a halogen lamp (P $\approx$ 100 W). A voltage of V = 50 V was applied to the sample and since the current was drifting slowly, we recorded current transients for background subtraction. In order to exclude further systematic errors, the magnetic field was swept forward (from 0 to 100 mT) and backward, as illustrated in Fig.4.12 by the black and red lines. In magnetoresistance a negative effect is defined as a decrease of the resistance and therefore as an enhanced current as observed in Fig.4.12 for higher magnetic fields. In the field range from 0 to 12 mT a weak

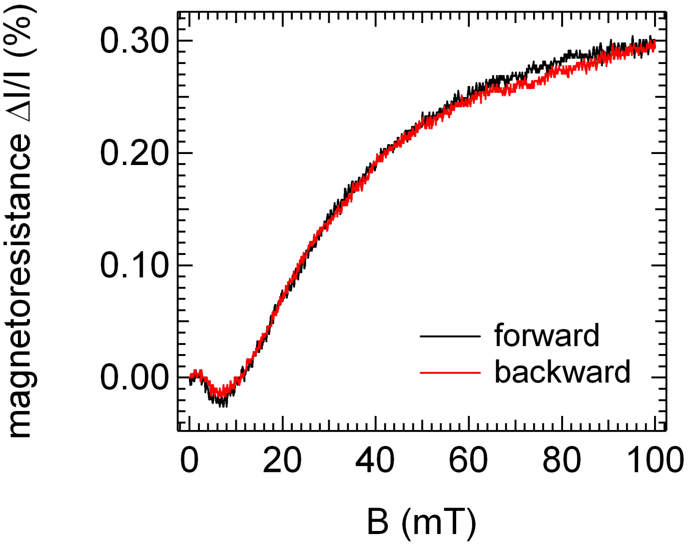

Figure 4.12: *magnetoresistance in the coplanar Au/ZnPc/Au device under illumination with a halogen lamp (P ≈ 100 W) and an applied voltage of V = 50 V. The magnetic field was swept forward and backward indicated by the black and red lines to reduce systematic errors. For background substraction the measurement was repeated without an applied magnetic field. The magnetoresistance effect is only observed under illumination.*

positive effect is observed, whereas at B = 100 mT the negative signal saturates at approximately 0.3 % which is a rather small effect. The signal is only present under illumination, which is similar to the situation observed in the EDMR measurements.

Discussion

Magnetoresistance in organic materials is generally explained by a change in the intersystem crossing rate between the triplet-level $T_{0,+,-}$ and the singlet state S_0. Two mechanisms may lead to an intersystem crossing. The exchange energy [116] and the hyperfine interaction [124]. Since the pEDMR results in § 6.4 indicate rather small exchange coupling in the ZnPc signal we will follow the model of Prigodin et al. [124] assuming hyperfine interaction as origin for the intersystem crossing rate. In the absence of a magnetic field the three triplet levels are degenerated as indicated in Fig.4.13. The model of Prigodin assumes a mixing of all four spin states in this case, induced by the influence of the hyperfine interaction. As a result the intersystem crossing rate is rather large. By applying an magnetic field to the spin system the triplet level split up by ΔE_B. In this case intersystem crossing is only possible between the states $|S_0\rangle$ and $|T_0\rangle$ which reduces the overall intersystem crossing rate. Prigodin assumes electron hole recombination to be the origin for the magnetoresistance effect in organic materials. Keeping this picture in mind, we want to adopt the polaron reencounter model [21], introduced in § 4.2, to explain the experimental results. The EDMR signal in the coplanar Au/ZnPc/Au device was observed to quench the current as a result of enhanced polaron pair

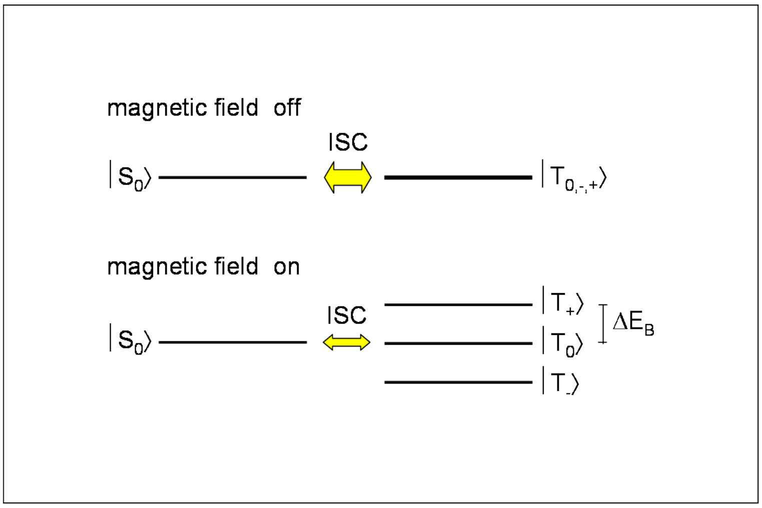

Figure 4.13: *Field induced changes in the intersystem crossing rate (ISC) are believed to be the origin for magnetoresistance in organic materials. .*

recombination under magnetic resonance conditions. The recombination enhancement could be understood by the conversion of triplet to singlet pairs during ESR, where the singlet pairs have a much higher recombination rate. This triplet to singlet conversion has a similar effect as the intersystem crossing rate (ISC) in magnetoresistance. With the magnetic field switched on, we can assume similar conditions as in an EDMR experiment before the microwave is switched on, namely a large surplus of triplet pairs due to their low recombination rate and few singlet pairs because of their strong recombination. Switching off the magnetic field enhances the ISC rate from the triplet to the singlet states and thus leads to a higher recombination associated in this device with a reduced current. This is exactly what is observed in our

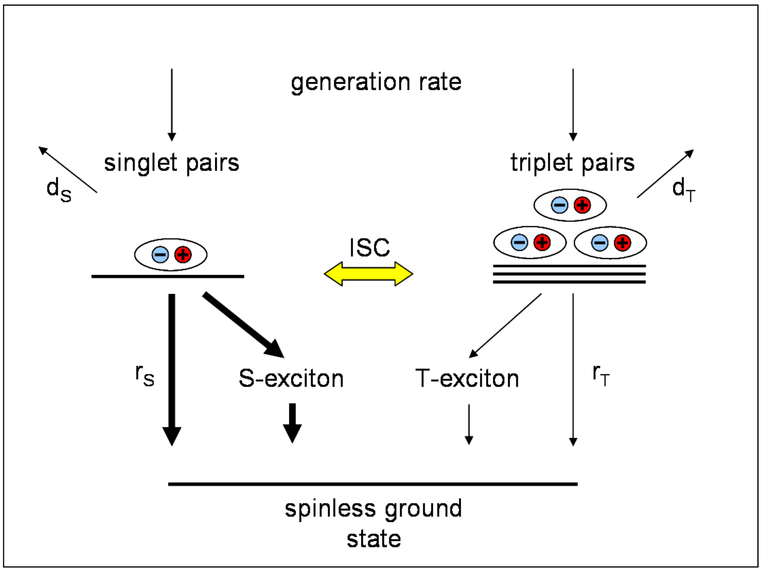

Figure 4.14: *spin-dependent polaron recombination as origin for magnetoresistance.*

experiments, switching off the magnetic field leads to a reduced current. The proposed spin-dependent recombination model for magnetoresistance and EDMR is illustrated in Fig.4.14. It is assumed that recombination can proceed directly or via excitonic states. In general the dissociation rates are also spin-dependent, but we assume that they are less dominant in our devices. In conclusion the polaron recombination model is capable of explaining the EDMR measurements, as well as the magnetoresistance effect in ZnPc devices and therefore suggests a common origin for both measurement techniques. As consequence, combined EDMR and magnetoresistance measurements can help to get a better understanding of the underlying spin-dependend mechanism.

Chapter 5

Spin Dynamics in ZnPc

In this chapter two types of pulsed EDMR experiments on ZnPc thin-film devices are presented and compared to cw EDMR results. In the first of these experiments the photocurrent transient after a short microwave burst is monitored as a function of the magnetic field B_0. This experiment yields a pulsed EDMR spectrum (signal vs. B_0), which is comparable to the cw EDMR spectra, and the recombination dynamics (signal vs. time). In section 5.2, a second type of experiment is introduced, in which the photocurrent is integrated over time after microwave bursts of various pulse lengths. This experiment provides information about the coherent spin nutation of the spin pairs during the microwave excitation. The consequences of selective and non-selective excitation on the spin nutation are discussed with respect to the phenomenon of spin-locking observed in radical pairs. At the end of the chapter conclusions about the spin-dependent transport-models will be drawn from the pulsed EDMR results.

5.1 Pulsed EDMR in ZnPc Layers

Pulsed EDMR measurements were performed on the ITO/ZnPc(200 nm)/Al device characterized in sec 4.1.2. A Stanford Research systems SR570 current amplifier was used together with a Stanford SR SIM928 battery voltage source, further setup information is given in § 2.4.2. In Fig.5.1 a) the photocurrent change after a microwave pulse is plotted vs. magnetic field B_0 (vertical axis) and vs. time t after the pulse (horizontal axis). The recorded photocurrent reflects the recombination behavior after the microwave pulse and has a signal peak strength of $\Delta I/I \approx 3 \text{ x } 10^{-4}$. The signal shows a photocurrent enhancement and therefore confirms the positive sign found in the cw EDMR measurements (§4.1.2). The signal relaxes back to the steady state with a mono-exponential decay. Fig.5.1 b) shows a 2D-fit of the EDMR signal that comprises a Gaussian function for the magnetic field dependence and a mono-exponential decay for the time axis. Since in the time interval from 0 µs to the yellow marker at 11 µs the signal is strongly affected by the response time of the current amplifier,

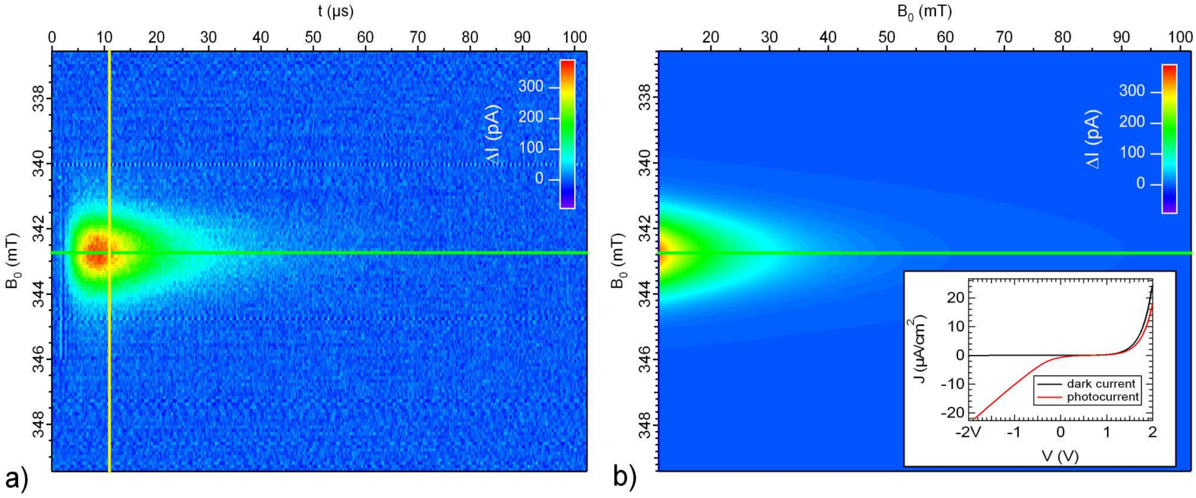

Figure 5.1: *a) transient photocurrent change* ΔI *of an ITO/ZnPc(200 nm)/Al device after a microwave pulse of 320 ns length (microwave power attenuation 10 dB,* $P_{mw} \approx$ *1kW at 0 dB). The sample was illuminated by a halogen lamp (P* $\approx$ *100 W) and a voltage of V = -2 V in reverse bias was applied to the sample. The current increases in resonance and relaxes back to the steady state value. The signal strength is in the order of* $\Delta I/I \approx 3 \times 10^{-4}$*. The yellow and green lines are markers for the line profiles given in Fig.5.2. b) 2D-fit function (from 11 to 102 µs) comprising a Gaussian function for the magnetic field dependence and an exponential decay in the time domain. Since the transient signal is dominated by the response time of the current amplifier in the time interval from 0 to 11 µs, this period was left out in the fit. The inset shows the IV-characteristics of the sample.*

this part was not included in the fit. The fit function reads:

$$f(B_0,t) = A \quad e^{-(B_0-B_{res})^2/C^2} e^{-Dt} + E \tag{5.1}$$

where the parameters C and D are related to the linewidth and the decay time of the signal. The fitparameters are summarized in Table 5.1. The g-factor (g = 2.0023(5)) is close to the

Table 5.1: fit results of the pEDMR signal in Fig.5.1 b) for an ITO/ZnPc/Al device.

lineshape	g-factor	FWHH (mT)	decay time 1/D (µs)
Gaussian	2.0023(5)	1.90	11.8

one observed in cw EDMR, whereas the linewidth ΔB = 1.90 mT is powerbroadened. The lineprofile at 11 µs (yellow marker) in Fig.5.2 a) shows that the signal can be adequately represented by a single Gaussian line, which is in contrast to the c.w. spectra. In Fig.5.2 b) a line profile at the resonant magnetic field (green marker in Fig.5.1 a)) shows the decay of the signal. The exponential decay has only one time constant, indicating that the signal is dominated by single process.

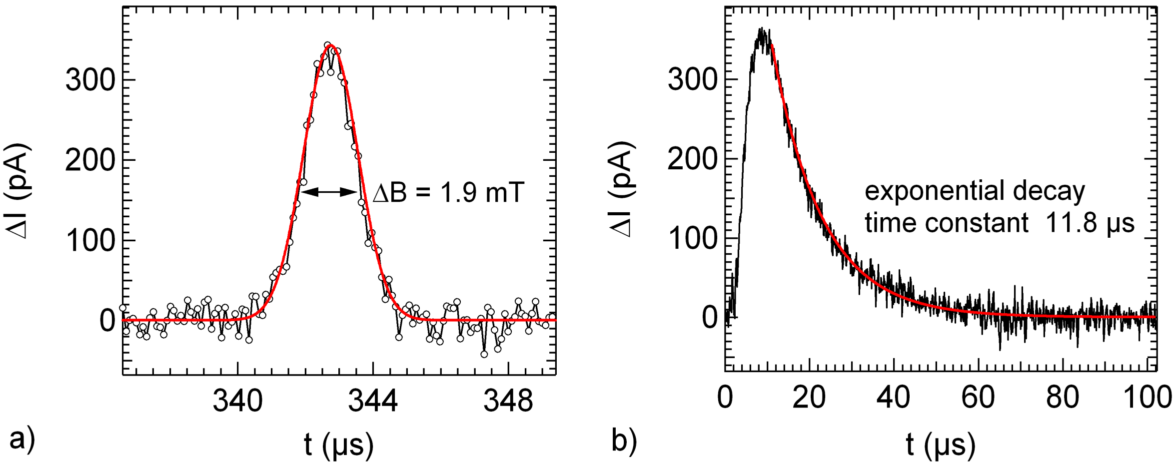

Figure 5.2: *a) line profile (open circles) at the yellow marker at 11 µs in Fig.5.1 a). The red line is the corresponding profile, at 11 µs, of the 2D fit function in Fig.5.1 b). b) line profile (black line) at the green marker (resonant B_0) in Fig.5.1 a) with the corresponding fit function.*

Discussion

The pEDMR signal lacks the second component observed in continuous wave measurements. One might speculate that the components have different saturation behavior due to different spin lattice relaxation times and, therefore, that at high microwave powers one of the components is much stronger than the other one. A second possibility is that the components have similar linewidth due to the line broadening at high microwave powers and hence cannot be resolved in the spectrum. This was already demonstrated in a cw EDMR linewidth study in § 4.4.2, where the linewidth of the components tend to become equal with increasing mw power. Since much higher mw-powers are used in the pulsed EDMR, we can assume that the linewidths become equal and the components cannot be resolved in the spectrum. The mono-exponential decay of the pEDMR signal leads to the assumption that only one spin-dependent process is observed under these conditions, which is in contradiction to the findings of the phase analysis, where two processes were assumed. However, if there is a second spin-dependent process one would have to assume that it is strongly decoherent or too weak for detection.

The observed EDMR signal strength of $\Delta I/I \approx 3$ x 10^{-4} is larger than the limit of $\Delta I/I \approx 10^{-6}$ expected for the theory of D. J. Lépine [14], which is based on thermal polarization of the spin ensemble, see § 1.4. Thus, the polaron reencounter model [21] is more applicable, which is based on the assumption that the recombining carriers form a pair state with considerable lifetime before they dissociate or recombine. Hence, spin-dependent processes that involve free charge carriers, like spin dependent scattering or trapping, can be ruled out here.

5.2 The Phenomenon of Spin-Locking

The pulsed EDMR measurements performed in the previous section reveal the transient photocurrent after a resonant microwave pulse. In order to obtain the spin nutation during the microwave pulse another method is needed, namely the variation of the pulse length. In this type of experiment, the transient photocurrent changes observed in Fig.5.2 b) are integrated over time for various pulse lengths, which yields a signal in the units of charge. Such a measurement was performed in the ITO/ZnPc/Al device and is depicted in Fig.5.3. Under illumination with a halogen lamp (P ≈ 100 W) the integrated photocurrent at V = -2 V shows coherent spin Rabi oscillations for 200 ns at room temperature. The size of the spin ensemble can be estimated, from the signal amplitude in elementary charges, to be in the order of 20000 spins. The Fourier transform of the spin oscillation (Inset of Fig.5.3) shows that the signal contains two frequency components with Ω_1 = 19.3 MHz and Ω_2 = 39.8 MHz $\approx 2\Omega_1$. The data points of the Fourier transform could be fitted with two Lorentzian lines of similar amplitude and width. The expected theoretical behavior of spin Rabi oscillations in the spin-dependent recombination model is given by Eq.1.52 (introduced in § 1.5), which expresses the state density changes in the spin pair ensemble. The oscillation frequency doubles when both spin partners in a pair are excited at the same time (non-selective excitation). In order to

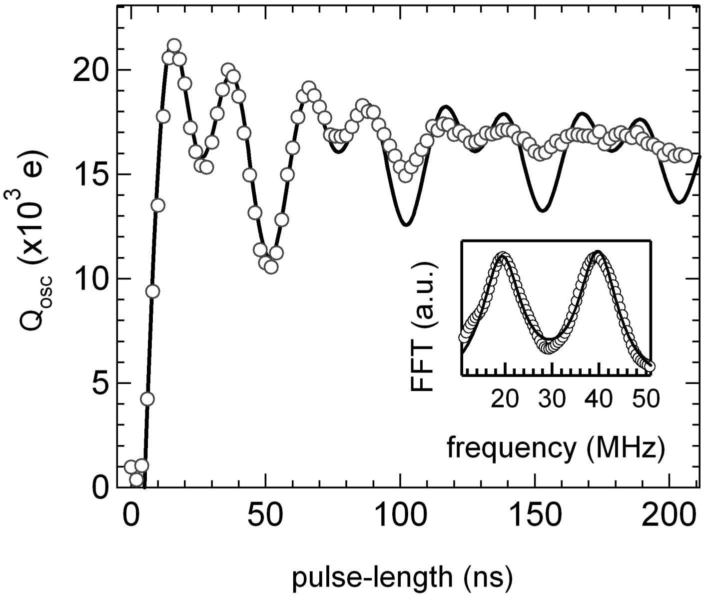

Figure 5.3: *Integrated photocurrent change (in elementary charges) of an ITO/ZnPc/Al device after resonant microwave pulses (power attenuation: 3dB), integration window: 5 - 16 µs. The microwave pulses were varied in 2 ns steps. The sample was illuminated by a halogen lamp (P ≈ 100 W) and a voltage of V = -2 V was applied in reverse bias direction. The signal (open circles) shows coherent spin Rabi oscillations up to 200 ns with two frequency components. The expected theoretical behavior is indicated in the plot (line). The Fourier transform (open circles) with a two-component Lorentzian fit (line) is shown in the inset.*

reproduce the signal in Fig.5.3 we used the simplified function T(α):

$$T(\alpha) = \pi \int_0^{\alpha} J_0(2x)dx \tag{5.2}$$

Here $\alpha = \kappa\gamma B_1\tau$ is the turning angle. For short enough pulses the aperiodic function $T(\alpha)$ contains a single frequency, which is given by $\Omega = \sqrt{(\gamma B_1)^2 + (\omega_{mw} - \omega_L)^2}$ for selective excitation ($\delta\omega \gg \gamma B_1$) or by 2Ω for the non selective case ($\delta\omega \ll \gamma B_1$). Thus a single $T(\alpha)$ - function cannot reproduce the alternating nutation behavior in Fig.5.3 where two frequency components are observed. In this case the fit function has to be a superposition of two $T(\alpha)$ - functions. The best result was attained, by using the following function:

$$f(\alpha) = T(\alpha) + 1.5T(2\alpha) \tag{5.3}$$

Fig.5.3 shows that the initial part of the Rabi-oscillation is reproduced by this function but that the experimental data show a stronger decay. This is due to the fact that spin relaxation times were not included in the derivation of $T(\alpha)$ [29]. The fact that the signal shows both, selective and non-selective excitation is the result of a Larmor distribution of ω_a and ω_b, which entails a distribution of $\delta\omega$. This situation is illustrated in Fig.5.4 for the case where both spins share a common Larmor-distribution. Fig.5.4 is oversimplified, since the condition $\delta\omega \ll \gamma B_1$ is

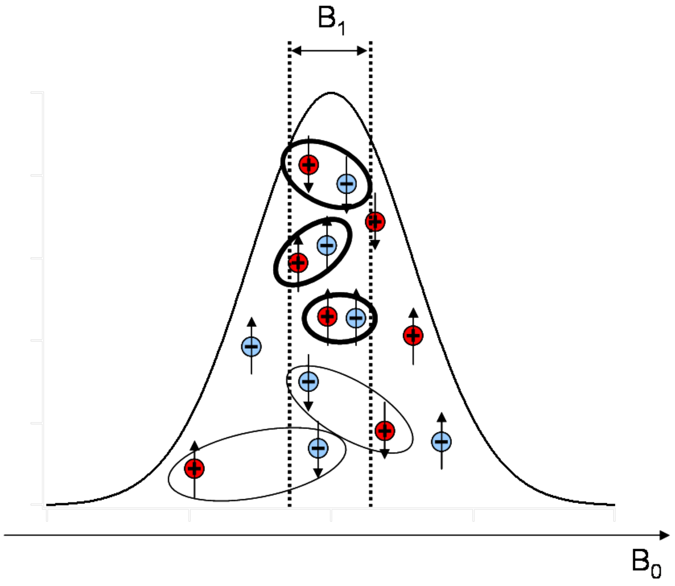

Figure 5.4: *Illustration of a Larmor distribution of spin pairs with different $\delta\omega$. The dashed lines mark the excitation width corresponding to the microwave driving field B_1. The spin pairs with $\delta\omega \ll \gamma B_1$ marked by thick ovals are excited non selectively and show the doubled frequency nutation. Note that pairs are formed in the spin ensemble bared on their spacial correlation, which does not imply a similar resonance frequency for both pair partners.*

not an exact measure for the transition between selective and non selective excitation and provides no information about the case when $\delta\omega = \gamma B_1$. However, it becomes clear that in such a Larmor distribution there are spin pairs with different Larmor separations $\delta\omega$, some of which fulfill the condition for non selective excitation $\delta\omega \ll \gamma B_1$ while others have $\delta\omega \gg \gamma B_1$ and are therefore excited selectively. It is clear that larger microwave fields B_1 will increase the fraction of non-selectively excited spin pairs.

The doubled Rabi frequency was also observed in absorption-detected magnetic resonance (ADMR) of radical pairs [36, 37], where the chemical reaction yield of a radical precursor pair is controlled by manipulating the population of spin sublevels in the radical pair. The double frequency beats were only observed under spin-locking conditions. The observed spin nutation was attributed to the spin dynamics in the triplet manifold (S = 1, m_S = +1, 0, -1), which is assumed to be decoupled from the singlet state (S = 0, m_S = 0) due to the spin-locking effect. The two spins precess together and are therefore assumed to be parallel all the time; they appear to be locked. The spin-locking effect in radical pairs is thus equivalent to the description of spin dependent recombination in items of the non selective excitation, and therefore the expression “spin-locking” will be used in further discussions. Fig.5.5 shows

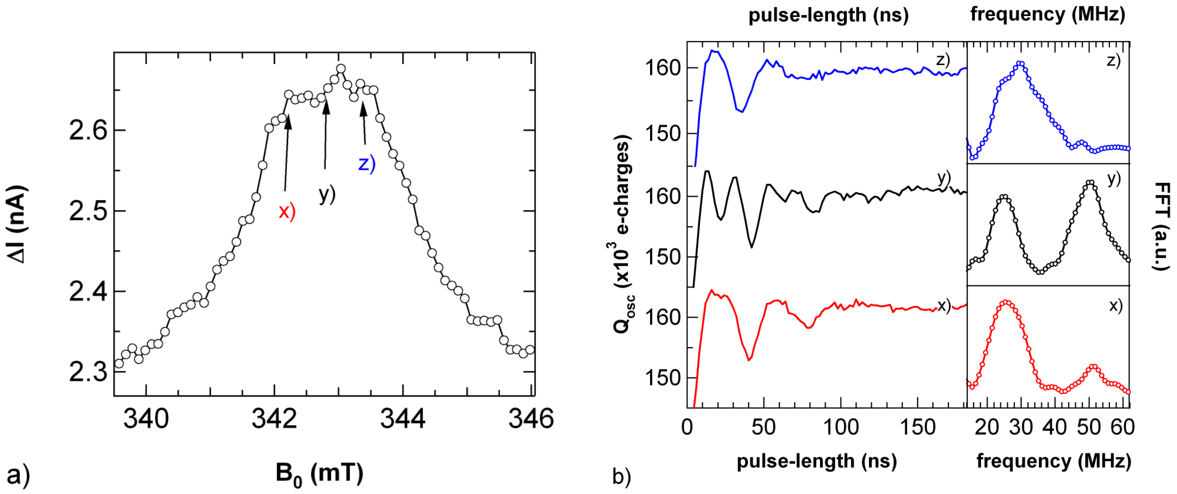

Figure 5.5: *a) pulsed EDMR spectrum of an ITO/ZnPc(200nm)/Al device after a microwave pulse with a pulse length of* τ *= 320 ns (power attenuation 1 dB). The sample was illuminated by a halogen lamp (P* $\approx$ *100 W) and a voltage of V = -2 V (reverse bias) was applied. b) Rabi oscillations recorded under the same conditions at different magnetic fields* B_0 *indicated by the arrows in a). The Fourier transforms are shown in the right part of the graph. The doubled Rabi frequency is only observed at the center field at point y).*

Rabi oscillations and their Fourier transforms at three different magnetic fields B_0 within the resonance line. However, the doubled Rabi frequency occurs only at the center field. This results from higher probability for pairs with small Larmor separation in the overlap region of the Larmor distributions of the two spins in the pair. If the spins share the same Larmor distribution as illustrated in Fig.5.4, the spin-locking occurs exactly at the resonance center. The combination of the single and the doubled Rabi-frequency leads to pronounced lineshapes in pulsed EDMR spectra, exspecially for short pulse lengths. This will be investigated in the next section.

5.2.1 Line Shapes Under Spin-Locking Conditions

The pEDMR lineshapes are strongly influenced by the effect of spin-locking. At pulse lengths longer than the coherence time of the spin nutation, the spectrum will become more or less M-shaped because the EDMR signal strength is weaker in the case of spin locking. Since the spin-locking regime is located at the resonance center, this part will be reduced in amplitude. For pulse lengths shorter than the coherence time of the spin nutation the pEDMR lineshape is strongly influenced by the two frequency components of the non-selectively (locked) and the selectively excited spin pairs. This behavior is illustrated in Fig.5.6, where the pEDMR spectra are shown for different pulse lengths. A pronounced M-shaped spectrum is observed after a π -pulse with respect to the doubled frequency, here attained at pulse length τ = 26 ns. At this pulse length the high frequency component has a minimum whereas the low frequency nutation shows a maximum.

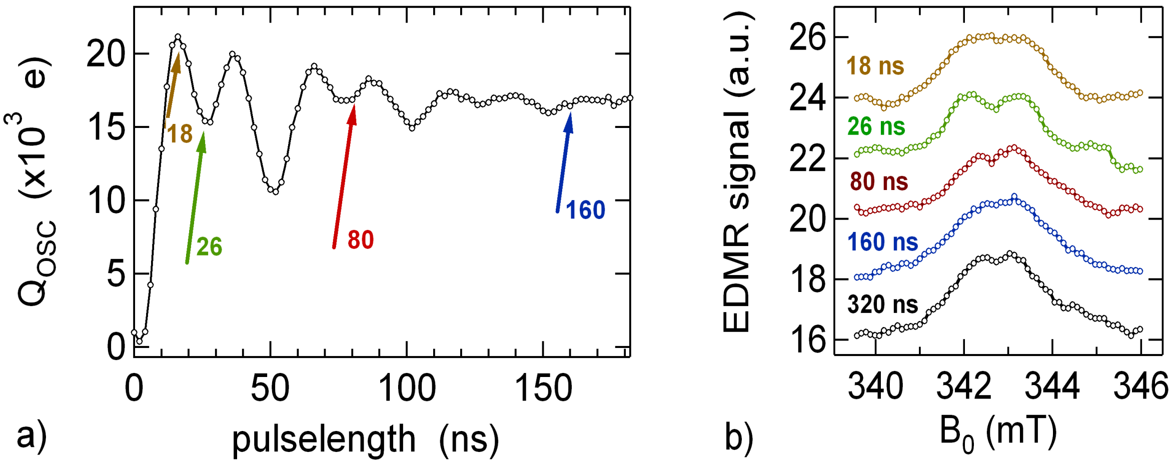

Figure 5.6: *a) coherent spin-Rabi oscillation of Fig.5.3 (power attenuation: 3 dB). b) pulsed EDMR spectra taken at different pulse lengths, recorded under the same conditions as the Rabi oscillation in a). The pulse lengths are indicated in a) by arrows.*

5.2.2 Beat Oscillations at different MW-Powers

In this section the microwave power dependence of the spin-locking effect in ITO/ZnPc/Al devices is investigated. Fig.5.7 shows the spin Rabi oscillations at three different microwave powers and the corresponding Fourier transforms. The Fourier analysis shows that the double frequency component is weak at low microwave powers (6 dB) and becomes dominant at high powers (1 dB). The opposite effect is observed for the low frequency component, which decreases at high microwave powers.

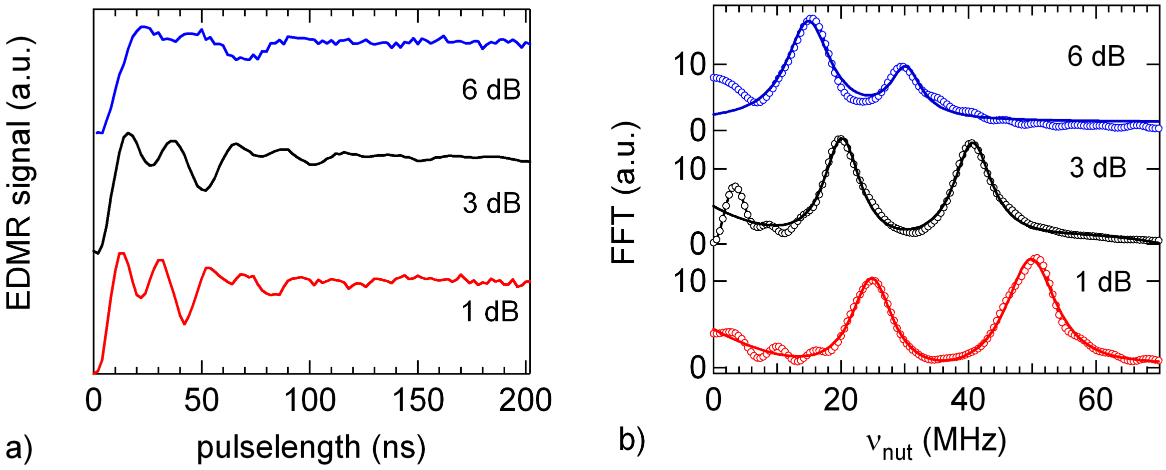

Figure 5.7: *a) Spin Rabi oscillations in an ITO/ZnPc(200nm)/Al device at three different microwave powers. A voltage of V = -2 V was applied to the sample, illumination was done by a halogen lamp (P ≈100 W). b) Fourier transforms of the data in a). The fraction of the double frequency component increases with increasing microwave power.*

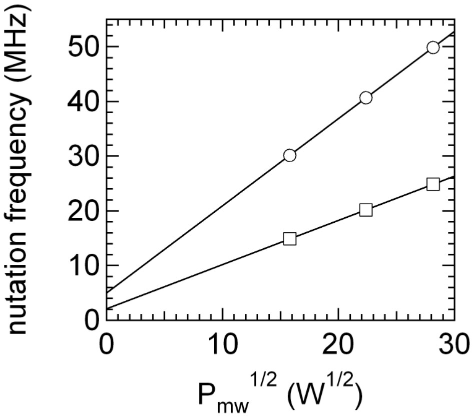

Figure 5.8: *Nutation frequencies of the spin Rabi oscillations in Fig.5.7 vs. square root of the microwave power. The nutation frequency components are proportional to the microwave driving field B_1.*

Since B_1 is proportional to the square root of the microwave power P_{mw} this behavior can be well explained in a spin pair ensemble with different Larmor separations $\delta\omega$. Since the condition for non selective excitation of the transitions in a spin pair is $\delta\omega \ll \gamma B_1$, the fraction of spin-locked pairs must increase with increasing microwave driving field B_1. As a result, the number of remaining spin pairs that are selectively excited shrinks. Furthermore, the nutation frequency at resonance is given by $\nu_{nut} = \frac{1}{2\pi}\gamma B_1$ and should thus be proportional to the square root of the microwave, which is shown in Fig.5.8 for both frequencies.

5.3 Pulsed EDMR in Au/ZnPc/Au Coplanar Devices

The cw EDMR signals of the coplanar Au/ZnPc/Al device and of the sandwich ITO/ZnPc/Al device have opposite signs. The cw EDMR spectra presented in § 4.4 however include a lock-in phase, which can alter the sign of the signal. The pulsed EDMR spectra were recorded with a direct technique and are therefore more reliable. Since the EDMR signal of the coplanar ZnPc device was rather weak, we used a Femto DHPVA-200 voltage amplifier in addition to the SR 570 current amplifier for this sample. Fig.5.9 a) shows the transient photocurrent

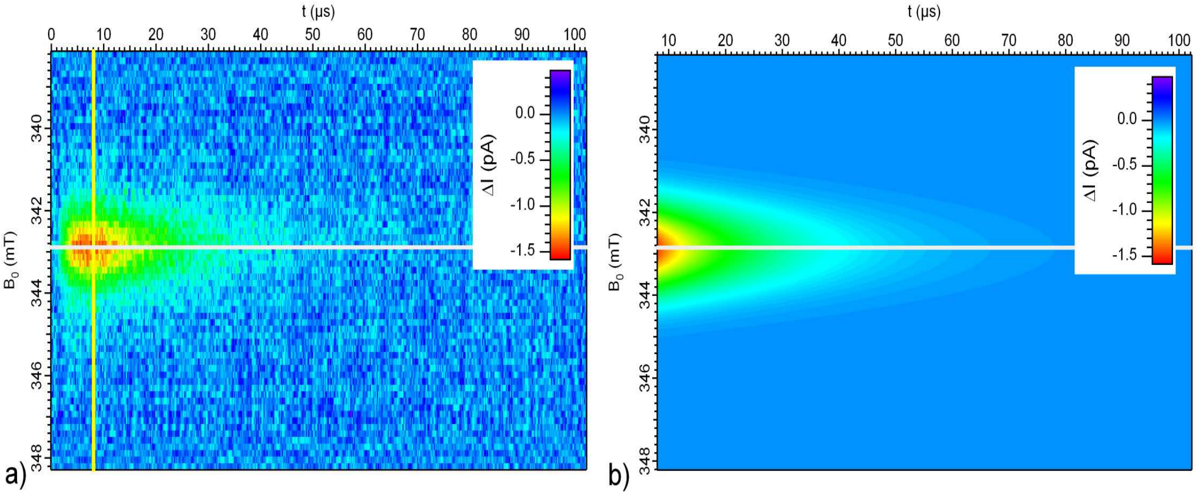

Figure 5.9: a) *Transient photocurrent change ΔI of a coplanar Au/ZnPc/Au device (30 M electrode spacing) after a microwave pulse of 320 ns length (microwave power attenuation 10 dB, $P_{mw} \approx$ 1kW at 0 dB, Illumination ($P \approx$ 100 W)). A voltage of V = 100 V was applied to the sample. The current quenches in resonance and relaxes back to the steady state value. The yellow and white lines are markers for the line profiles given in Fig.5.10. b) 2D-fit function (from 8 to 102 µs) comprising a Gaussian function for the magnetic field dependence and a mono-exponential decay in the time domain. Since the signal is dominated by the response time of the current amplifier in the time interval from 0 to 8 µs, this period was left out in the fit.*

changes of a coplanar Au/ZnPc/Au device after a resonant microwave pulse (τ = 320 ns) vs. time (horizontal axis) and vs. magnetic field (vertical axis). The photocurrent is quenched in resonance at g = 2.0018(5) and therefore supports the negative sign in cw EDMR measurements, (see § 4.1.1). The signal could be fitted with the 2D-fit function given in Eq.5.1. The result is illustrated in Fig.5.9 b) and shows that the signal is composed of a Gaussian lineshape for the spectral part (see Fig.5.10 a)) and a mono exponential decay along the time axis (see Fig.5.10 b). Lineshape and width (ΔB = 1.7 mT) are similar to those observed in the ITO/ZnPc/Al sample (ΔB = 1.9 mT). However, since the pulsed EDMR spectra are broadened due to high microwave excitation intensities the linewidth can differ from one experiment to another due to different microwave intensities. The exponential decay shows a time constant of 1/D = 16.4 µs which is larger than in the ITO/ZnPc/Al device (1/D ≈ 11.8 µs). Since the EDMR transients depend not only on recombination and relaxation rates but also on capacitances and impedances of the sample and the setup, the distinct time constants can be

Table 5.2: *2D-fit results of the pEDMR signal in Fig.5.9 for a coplanar Au/ZnPc/Au device.*

lineshape	g-factor	FWHH (mT)	decay time 1/D (µs)
Gaussian	2.0018(5)	1.7	16.4

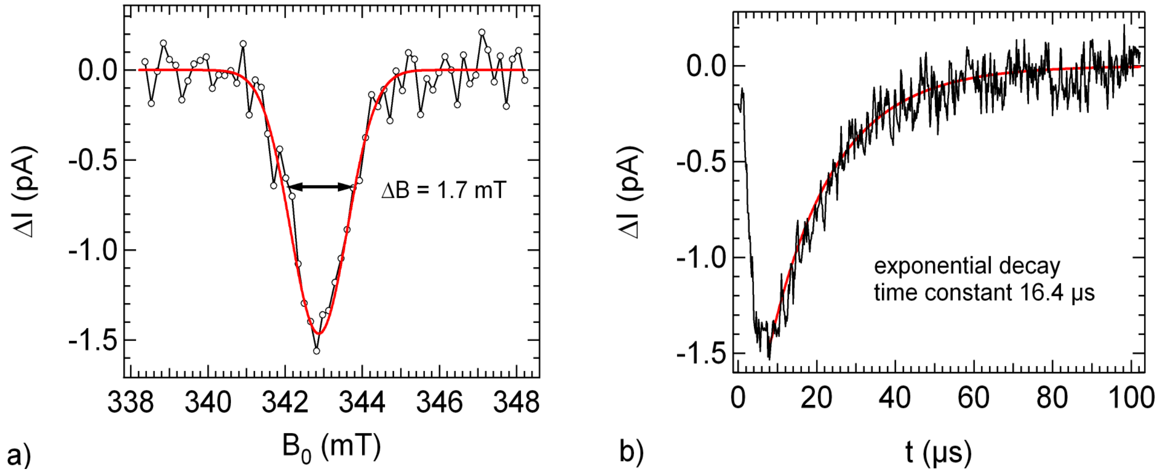

Figure 5.10: *a) Pulsed EDMR spectrum (open circles) at the yellow marker at 8 μs in Fig.5.9 with the corresponding 2D-fit function line profile at 8 μs (red line). The lineshape is Gaussian with a linewidth of* $\Delta B = 1.7$ *mT. b) Time trace of the photocurrent at the center field indicated by the white marker in Fig.5.9. Line profile of the fit function at the center field (red line) showing a mono-exponential decay with a time constant of* $1/D = 16.4$ *μs.*

explained not only by the rather different device architectures of the two samples, but also from the different transport mechanisms. The signal of the coplanar device is thus attributed to polaron recombination, as in the cw EDMR measurements (§ 4.1.2).

5.3.1 Decoherence in Au/ZnPc/Au devices

Spin nutation experiments were carried out on the coplanar Au/ZnPc/Au device in order to investigate the spin-locking behavior observed in the ITO/ZnPc/Al samples. The integrated photocurrent through the device was recorded as a function of the microwave pulse length at resonant magnetic field, but the experimental data shown in Fig.5.11 show strongly damped oscillations. The decay of the spin nutation could be either caused by impurity- or defect-related spins adjacent to the spin pairs or by distorted microwave magnetic fields (B_1) due to the coplanar electrode array. Since a direct measurement of the spin nutation (Fig.5.11) provides no conclusive information about the presence of spin-locking in the Au/ZnPc/Au device, we used more sensitive method of lineshape analysis, introduced in § 5.2.1.

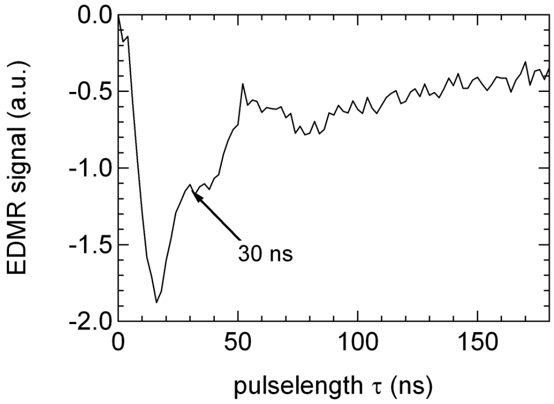

Figure 5.11: *Integrated photocurrent change of a coplanar Au/ZnPc/Au vs. microwave pulse length (power attenuation: 3 dB) at resonant magnetic field, integration window: 4 - 14 μs. The sample was illuminated by a halogen lamp (P ≈ 150 W) and a voltage of V = 100 V was applied. (The pulse length at which the pEDMR spectrum in Fig.5.12 was recorded is indicated by the arrow.)*

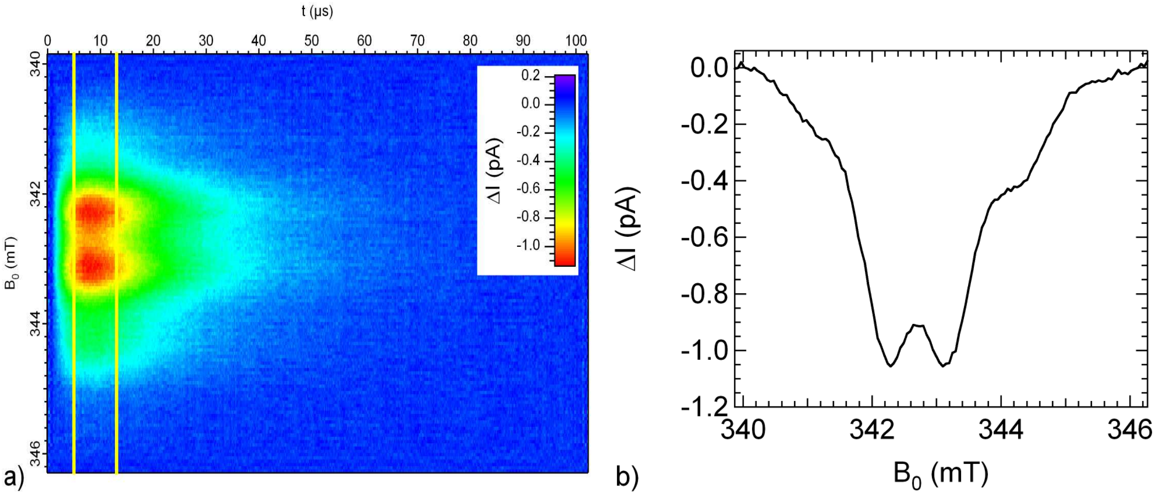

Figure 5.12: a) *transient photocurrent change ΔI of a coplanar Au/ZnPc/Au device (30 μm electrode spacing) after a microwave pulse of 30 ns length (microwave power attenuation 3 dB, Illumination (P ≈ 100 W)). A voltage of V = 100 V was applied to the sample. The current quenches in resonance and relaxes back to the steady state value. b) Pulsed EDMR spectrum integrated over the time interval indicated in a) by the yellow markers. The spectrum shows a W-shaped resonance line expected for spin-locking.*

Pulsed EDMR spectra were investigated under high microwave powers (3dB) and at short pulse length (τ = 26 ns) to reveal the typical spin-locking lineshapes. The result, depicted in Fig.5.12, indeed shows a W-shaped resonance line as expected for spin-locking, which is very similar to the spectrum at τ = 26 ns in the ITO/ZnPc/Al device (Fig.5.6). In both cases, the line shapes are asymmetric and show an extra structure on the high field side. This might in principle due to a second superimposed signal. A Comparison to the cw EDMR spectrum in § 4.4 shows that the broad component in the cw spectrum is also at the high field side, although it is shifted by less than 0.1 mT from the narrow signal. This shift is much higher in the pulsed spectrum and it is therefore the signals seem not to be correlated.

5.4 Discussion and Conclusions

In this chapter we presented pulsed EDMR measurements on sandwich ITO/ZnPc/Al devices and on coplanar Au/ZnPc/Au samples. The pulsed EDMR spectra showed that the two devices exhibit signals of similar lineshape but opposite signs. The sign change confirms the findings of the cw EDMR study (§ 4.1.2), where the coplanar Au/ZnPc/Au device showed a photocurrent quenching, ascribed to spin-dependent polaron recombination, while the ITO/ZnPc/Al device showed a photocurrent enhancement, which was tentatively assigned to the same process altered by charge accumulation at the oxidized Al electrode. In the pulsed EDMR spectra, the two signals found in the cw EDMR spectra could not clearly be resolved, probably due to the broadening of the resonance lines. However, at high microwave powers or short pulse length, an extra signal seems to be superimposed on the resonance, but it could not be identified with one of the cw EDMR signals. The transient behavior of the EDMR signal shows a mono-exponential decay for both types of ZnPc devices, which supports the assumption that only one spin-dependent process is observed. Hence, the origin of the second component remains unclear. The EDMR spin nutation experiments revealed coherent spin Rabi oscillations under spin-locking conditions for the ITO/ZnPc/Al device. The observation of spin-locking is a direct proof for the spin nutation of a spin pair, which means that we can exclude all spin 1/2 processes like radical triplet quenching and a broadening of the one of the spin pair partners in the EDMR spectrum. Furthermore the spin-locking behavior requires a long lived pair state, which is also required for the polaron reencounter model introduced in § 1.4. As a result we can rule out all processes including free charge carriers like spin-dependent scattering or trapping, which confirms our previous assumption, that polaron recombination accounts for the EDMR signals in ZnPc.

Chapter 6

Spin-Dependent Transport in ZnPc/C_{60} Solar Cells

In this chapter we will apply the methods of the previous chapters to more complex multilayer devices. The knowledge about the EDMR signals of ZnPc, gained from the previous sections and about those of C_{60} obtained in former work [2, 4] turns out to be an adequate basis for the assignment of the EDMR signals. After introducing the IV-characteristics of the first solar cell device "solar1new" (§ 6.1), continuous wave and pulsed EDMR measurements are presented and interpreted in the context of the known ZnPc and C_{60} signals (§ 6.2). In § 6.3, a second solar cell device "solar2new" is introduced where two EDMR signals can be separated by using different light intensities. In § 6.4, the nutation behavior under spin-locking conditions is discussed in detail for the device solar1new. Conclusions are drawn for the exchange interaction of the spin pairs and the underlying process. Finally, Rabi beat oscillations of the two EDMR signals are compared in § 6.5 and the origin of the signals is discussed.

6.1 IV-Characteristics of Solar1new

Organic multilayer devices are very complex systems, since not only the charge transport in the bulk material is of great importance but also the interfaces between the layers and the organic metal interfaces. The ITO/ZnPc/C_{60}/BCP/Al-solar cells investigated in this work contain a bathocuproine (BCP) buffer layer between the fullerene C_{60}-layer and the top-aluminum contact. The use of bathocuproine generates an Ohmic contact at the C_{60}/Al interface and reduces interface recombination [70]. Therefore, the organic metal contacts at the ITO/ZnPc- and C_{60}/BCP/Al-interfaces seem to be uncritical in this device. The layer structure of the ITO/ZnPc(30 nm)/C_{60}(30 nm)/BCP(17 nm)/Al device is illustrated in Fig.6.1 a), whereas the substrate geometry and encapsulation is specified in § 2.3.2. The organic layers were deposited onto the cleaned ITO substrate by vacuum sublimation, with preparation parameters summarized in Table 6.1. The aluminum top contact was added by the same technique. The

Table 6.1: *Preparation parameters of the ITO/ZnPc/C_{60}/BCP/Al device "solar1new"*

Material	thickness [nm]	rate [Å/sec]	temp. [°C]	vacuum p. [mbar]
ZnPc	30	1.0	455	2.5×10^{-7}
C_{60}	30	0.5 - 0.9	510	2.1×10^{-7}
BCP	17	1.0 - 1.5	225	5×10^{-6}
Al	50	≈ 2.5	1350	3×10^{-6}

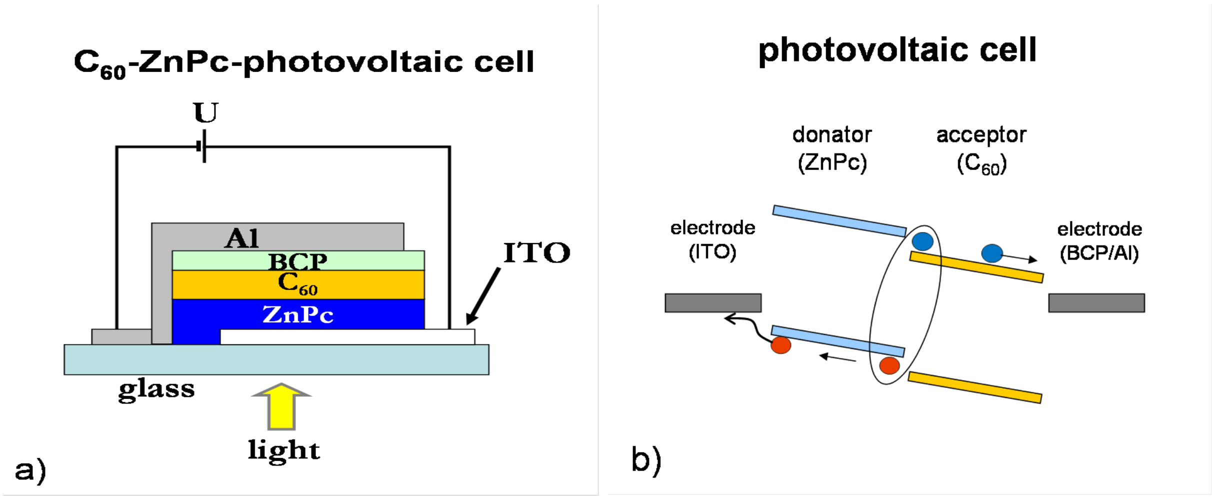

Figure 6.1: *a) Layer system of the ITO/ZnPc(30 nm)/C_{60}(30 nm)/BCP(17 nm)/Al solar cell. The organic layers and the metal were brought onto the ITO substrate by physical vapor deposition. b) Working principle of an organic solar cell under equilibrium conditions (V_{ext} = 0 V). Light-generated excitons, that reach the donor-acceptor interface will be separated into positive and negative charge carriers, which are accelerated towards the extracting electrodes by an inner electric field. In this case the donor and acceptor are ZnPc and C_{60} respectively.*

photocurrent generation in bilayer heterojunction solar cells is different from that in the Schottky devices discussed previously. Excitons are generated in the photoactive layers ZnPc and C_{60} by absorption of light. Some of these excitons may reach the ZnPc/C_{60}-interface, where a highly efficient charge transfer takes place [125, 126]. As a result, mobile and immobile charge carriers (polarons) are generated at the organic hetero-interface (see Fig.6.1 b)). The negative polarons drift through the fullerene layer towards the aluminum electrode whereas the positive polarons move in the ZnPc layer towards the ITO contact. Charge carrier drift is promoted by an inner electric field of the heterojunction and the contacts, accompanied by diffusive charge transport. Furthermore bulk carrier generation has to be considered. However, since exciton splitting at the molecular hetero-interface is much more efficient than in the bulk, the charge carrier generation is dominated by the interface. For the same reason higher efficiencies are usually observed in heterojunction cells. The IV-characteristics of the ITO/ZnPc/C_{60}/BCP/Al device "solar1new" depicted in Fig.6.2 a) shows that the rectification behavior is rather poor in the dark and under illumination. The open circuit voltage V_{oc} (= 0.42 V) and fill factor are small and as a result the efficiency is low (see Table 6.2). After

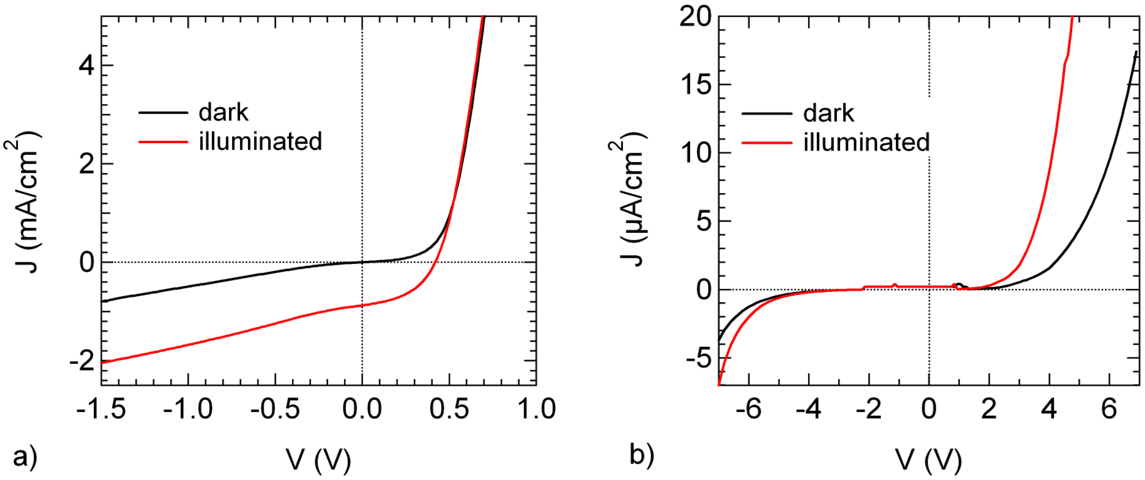

Figure 6.2: *a) IV-characteristics of the ITO/ZnPc/C_{60}/BCP/Al solar cell "solar_1new" in the dark and under white light illumination (halogen lamp, $P \approx 100$ W). The IV-curves of the as prepared sample were recorded under nitrogen atmosphere (0.3 ppm oxygen). b) IV-curves of the same sample during the EDMR measurements. The sample shows strong degradation.*

Table 6.2: *IV-parameters of the ITO/ZnPc/C_{60}/BCP/Al device (solar1new) under illumination (halogen lamp, $P \approx 100$ W) in nitrogen atmosphere*

J_{sc} (mA/cm^2)	V_{oc} (V)	η (%)	ff (%)
0.8	0.42	0.16	44.7

preparation, the device was encapsulated under nitrogen atmosphere without intermediate exposure to air. The IV-characteristics, recorded during the EDMR measurements one day later however show strongly reduced currents in the dark and under illumination. This degradation can be explained by the influence of residual oxygen and can be prevented by a more effective encapsulation as described in § 3.2.3. Whereas the conductivity of ZnPc is increased during oxygen exposure due to a p-type doping effect, the conductivity of C_{60} is reduced by several orders of magnitude in the presence of oxygen. The degradation of CuPc/C_{60}-solar cells due to oxygen was systematically investigated by M. Rusu et al. [127] who showed that oxygen mostly affects the photoelectrical properties of the fullerenes and induces new recombination levels that accelerates the degradation process. In conclusion the degradation of the ZnPc/C_{60} -solar cell is assumed to stem from the decreased conductivity of the fullerene layer due to the influence of residual oxygen.

6.2 Spin Dependent Processes in Bilayer Cells

6.2.1 Continuous Wave EDMR

The investigation of a bilayer organic solar cell is a step further towards complex organic devices. However, in a previous work, we performed pulsed EDMR in C$_{60}$ single layer devices [2, 4] and the EDMR signal of ZnPc devices is known from this work. This allows us to identify those EDMR features in the bilayer solar cells that originate from the constituent materials and to distinguish them from new effects related to the heterojunction interface or, more generally, its architecture. An ITO/ZnPc/C$_{60}$/BCP/Al device (solar1new) was investigated with c.w. EDMR under illumination, using the setup described in § 2.4.2. At an applied voltage of V = -1 V (reverse bias) the photocurrent enhances in resonance, as depicted in Fig.6.3 a). The EDMR resonance line could be fitted with a superposition of two Gaussian lines with similar parameters as for the ZnPc device; the fit parameters are listed in Table 6.3.

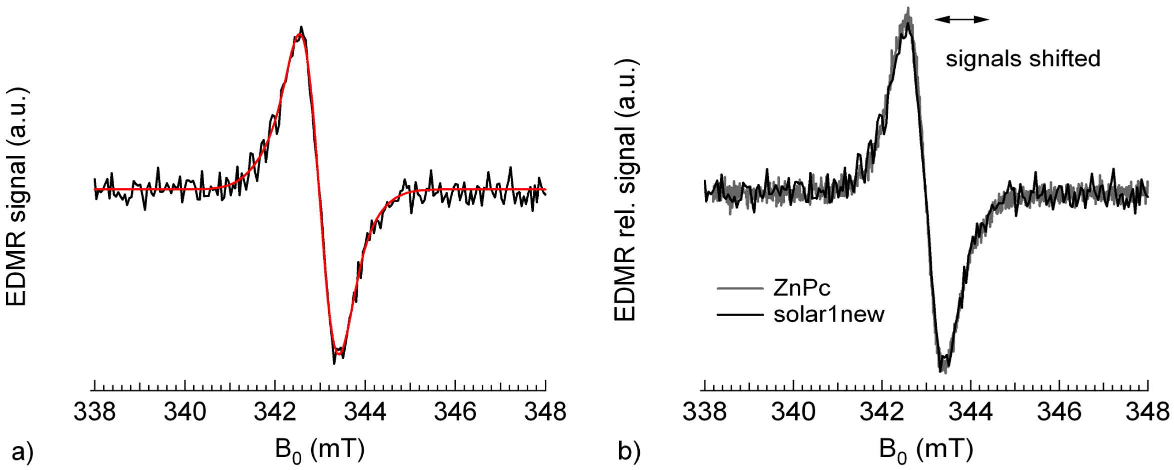

Figure 6.3: *a) cwEDMR signal of an ITO/ZnPc/C$_{60}$/BCP/Al device (solar1new) under illumination (halogen lamp, $P \approx 100$ W) with an applied voltage of V = -1V. A microwave power of $P_{mw} \approx 20$ mW was applied and the magnetic field was modulated with an amplitude A_{mod} = 0.7 mT and a frequency f_{mod} = 10 kHz. The data (black line) were fitted with a superposition of two Gaussian lines (red line). b) EDMR signals of ZnPc and solar1new. The resonance position and amplitudes were adjusted for better comparison of the lineshapes.*

Table 6.3: *EDMR fit parameters of the Au/ZnPc/Au device (§ 4.4.1) and the ITO/ZnPc/C$_{60}$/BCP/Al (solar1new) solar cell in Fig.*6.3

sample	FWHH ΔB_a (mT)	FWHH ΔB_b (mT)	g_a	g_b
ZnPc	0.95	1.56	2.0022(5)	2.0021(5)
solar1new	0.9	1.6	2.0020(5)	2.0025(5)

6.2.2 Discussion

A direct comparison of the lineshapes of the solar cell and the ZnPc sample shown in Fig.6.3 b), reveals almost equal resonance lines. Surprisingly, the g-factor of the broad feature is now at a higher g-value. A priori, this could be due to a different environment of the spins or different paramagnetic species. Since the EDMR signal measured in C_{60} exhibits a Lorentzian lineshape with a much smaller linewidth (0.3 mT) [2, 4] it cannot account for the broad signal. Therefore, the signal is tentatively attributed to the ZnPc material with an as yet unexplained origin of the broad component.

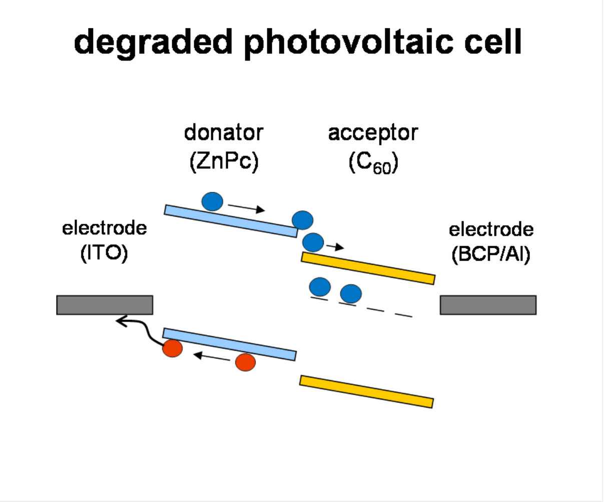

Figure 6.4: *Illustration of a possible charge accumulation process at the hetero interface of the degraded solar cell. Negative polarons generated in the ZnPc bulk material reach the hetero interface. Since the charge transport in* C_{60} *is assumed to be strongly reduced due oxygen related traps, negative polarons accumulate near the hetero interface and block the current.*

Interestingly, the signal is current enhancing, which was previously ascribed to the influence of accumulated charges at the oxidized ZnPc/Al interface, see § 4.1.1. Hence there must be a reason for charge accumulation in the solar cell. The expected interface for the accumulation of negative charge carriers in reverse bias would be the ZnPc/C_{60}-contact. If we assume a "standard" energy level scheme for the solar cell as the one illustrated in Fig.6.1 b) there would be no reason for such a charge accumulation. A possible explanation could be the presence of interface traps that act as recombination centers. This could also explain a different g-value associated with a paramagnetic trap level. However, the IV-characteristics in Fig.6.2 b) indicates that the device performance is strongly degraded which can be attributed to an increased trap density in the C_{60} layer, due to the influence of oxygen [127]. As a consequence the resistance of the C_{60} layer becomes very high and the transport of charge carriers is strongly reduced in this material.

Under these conditions the C_{60} layer acts like an insulator and charge accumulation at the

ZnPc/C_{60} interface becomes a conceivable scenario, see Fig.6.4. This provides a second possible explanation for an accumulation of charges. If this explanation holds, the EDMR signal should become negative at higher forward biases, as observed in the ZnPc devices, since in forward bias negative charges are extracted at the ITO contact where charge accumulation is unlikely. Without the charge accumulation, spin-dependent recombination would lead to a current quenching, due to the annihilation of charge carriers. We will see in the next section that the EDMR signal indeed reverses sign at forward bias.

6.2.3 Pulsed EDMR in ZnPc/C_{60}-Solar Cells

Pulsed EDMR experiments were performed in ITO/ZnPc/C_{60}/BCP/Al devices, introduced in the previous section. In this experiment a Keithley current source was used, which has a response time much longer than the duration of the transient EDMR experiment and therefore does not influence the signal. The photocurrent of the sample solar1new after resonant microwave excitation is illustrated in Fig.6.5 b) under reverse bias conditions. After the expected enhancement the current quenches before it reaches the steady state value again. The data could be fitted with a double exponential function with the time constants $1/D_1$ = 3.9 S for positive part and $1/D_2$ = 9.3 µs for the negative part. The spectra of the quenching and

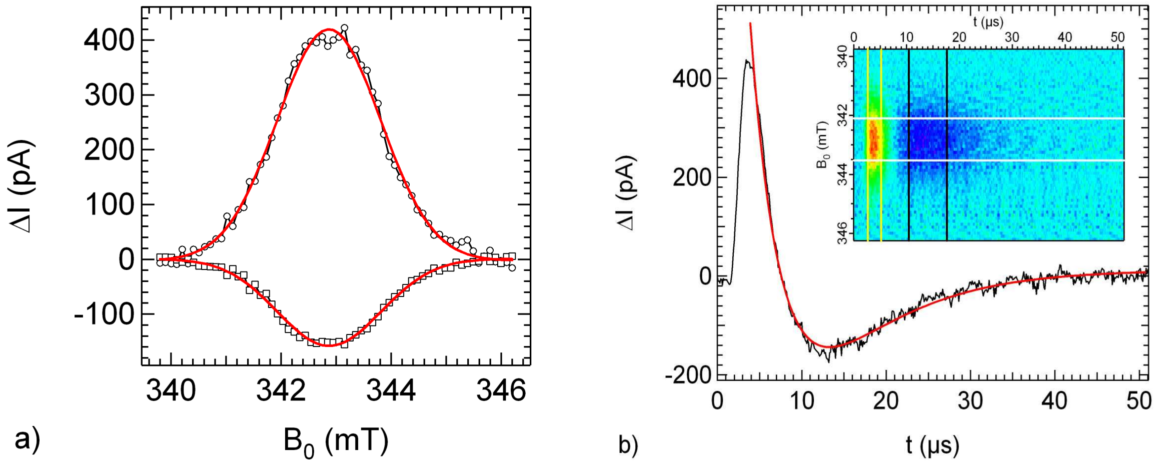

Figure 6.5: *a) Pulsed EDMR spectra of an ITO/ZnPc/C_{60}/BCP/Al device (solar1new) under illumination (halogen lamp $P \approx 100$ W) in reverse bias (I = -1 μA). The spectra were recorded after a resonant microwave pulse (power attenuation: 10 dB) of pulse length τ = 320 ns. The photocurrent first enhances (positive spectrum, integration between the yellow markers) and then quenches (negative spectrum, integration between the black markers) before it relaxes to a steady state value. The spectra were each fitted by single Gaussian function indicated by the red lines. b) Photocurrent change after the resonant microwave excitation at resonant magnetic field. The red line corresponds to a double exponential fit-function. The inset shows the color plot of the signal vs. magnetic field (y-axis) and vs. time (x-axis). The integration windows for the spectra are marked by the yellow (enhancement) and black lines (quenching) whereas the one of the time trace is indicated by white markers.*

the enhancement is shown in Fig.6.5 a). Both resonance lines could be fitted with a single Gaussian function, where equal linewidth ΔB = 2.2 mT and g-factors of g = 2.0026(5) were obtained for the resonances. However, under forward bias conditions the situation changes drastically, as shown in Fig.6.6. At a constant offset current of I = 0.5 μA in forward bias, the EDMR signal is quenching and can be discribed by mono-exponential decay function with a decay constant of 1/D = 8.4 μs. The low microwave power (18 dB) used in this experiment reveals the two components of the signal (fit parameters are in Table 6.4).

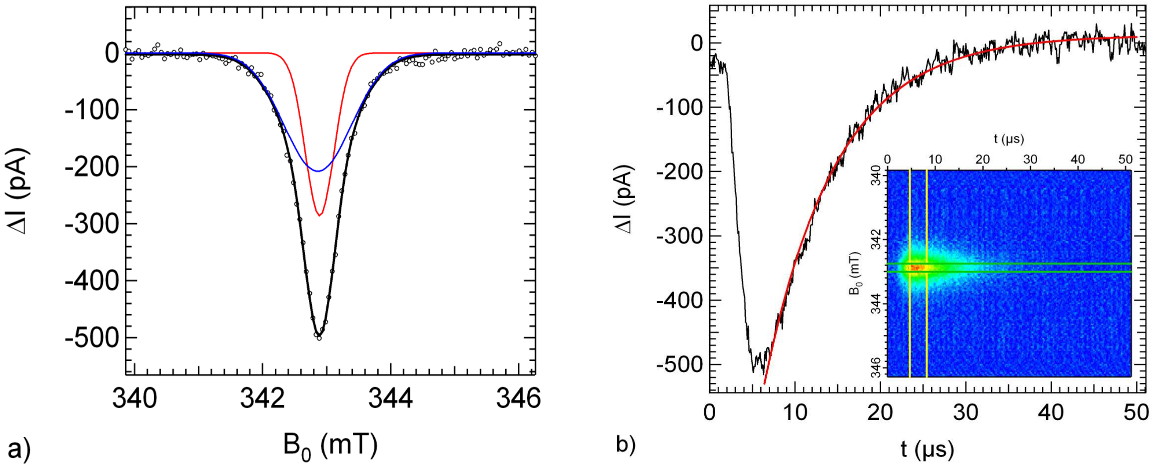

Figure 6.6: *a) Pulsed EDMR spectrum of an ITO/ZnPc/C_{60}/BCP/Al device (solar1new) under illumination (halogen lamp $P \approx 100$ W) in forward bias ($I = 0.5$ μA). The spectrum was recorded after a resonant microwave pulse (power attenuation: 18 dB) of pulse length $\tau = 320$ ns. The integrated spectrum (integration between the yellow markers) was fitted by a superposition of two Gaussian functions indicated by the red and blue lines. b) Photocurrent changes after the resonant microwave excitation at resonant magnetic field. The photocurrent quenches before it relaxes to a steady state value. The red line corresponds to a mono-exponential decay. The inset shows the color plot of the signal vs. magnetic field (y-axis) and vs. time (x-axis). The integration windows for the spectrum is marked by the yellow lines whereas the one of the time trace is indicated by the green markers.*

Table 6.4: *EDMR fit parameters of the ITO/ZnPc/C_{60}/BCP/Al (solar1new) solar cell in forward bias (see Fig.6.6).*

EDMR signal	FWHH ΔB (mT)	g-factor	1/D (μs)
component a	0.53	2.0024(5)	8.4
component b	1.24	2.0026(5)	8.4

6.2.4 Discussion

The transient behavior of the EDMR signal in reverse bias shows a current enhancement followed by a quenching. This behavior can be either the consequence of the reaction dynamics of a single spin dependent process (non vanishing triplet recombination) or it may be a superposition of two signals. If we follow the interpretation advanced in § 6.2.2, where the positive EDMR signal was assigned to ZnPc, the current quenching must be due to a new spin-dependent process. The origin of this new process will be discussed in following sections.

The EDMR experiment in forward bias shows a quenching signal with a mono-exponential decay. The signal was recorded at low microwave power, to enhance the resolution. Although two components are observed in the spectrum only one decay constant is observed. It would be a natural assumption that the enhancement signal has vanished in forward bias and the negative signal has persisted. This is also supported by the similar decay times of the negative signals in forward and in reverse bias. However, the interpretation of the decay times is difficult, since the impedance of the sample changes strongly from reverse to forward bias, which may have impact on the signal. Further experiments will show that the negative signal in reverse bias exhibits large linewidths (ΔB = 1.08 mT) even at low microwave powers (24 dB) and differs significantly in lineshape from the negative signal in forward bias (see § 6.3.2). Therefore the quenching processes in in forward and reverse bias cannot have the same origin. Therefore we propose an interpretation, where in forward bias the ZnPc signal changes sign and the new spin-dependent process vanishes. The sign reversal of the ZnPc signal was already observed in ZnPc single layer devices investigated in chapter 5. Further EDMR experiments at low microwave power will show, that the lineshapes of the ZnPc signal is very similar to the quenching signal in forward bias. Furthermore the new spin-dependent process associated with the quenching signal in reverse bias will be investigated in the following section, where the quenching and the enhancement signal are separated by variation of the light intensity.

6.3 Signal Decomposition by Light Intensity Control

6.3.1 IV-Characteristic of Solar2new

For further investigations of the positive and negative components in the EDMR signal of C_{60}/ZnPc solar cells a second ITO/ZnPc/C_{60}/BCP/Al - device (solar2new) was prepared. The organic layers were brought onto the cleaned ITO substrate by physical vapor deposition, the preparation parameters are summarized in Table 6.5. The layer structure and thickness is identical to sample solar1new investigated in the last sections. The IV-characteristics of the as-prepared sample shown in Fig.6.7 a) indicate a better rectification behavior and higher short circuit current than in sample solar1new, see Table 6.6. This results in a higher efficiency for solar2new, however degradation could not be prevented during the EDMR measurements, as can be seen in Fig.6.7 b).

Table 6.5: *Preparation parameters of the ITO/ZnPc/C_{60}/BCP/Al device "solar2new"*

Material	thickness [nm]	rate [Å/sec]	temp. [°C]	vacuum p. [mbar]
ZnPc	30	1.3	453	4×10^{-7}
C_{60}	30	1.0	500	2×10^{-7}
BCP	17	1.5	230	7×10^{-6}
Al	50	≈2.5	1350	3×10^{-6}

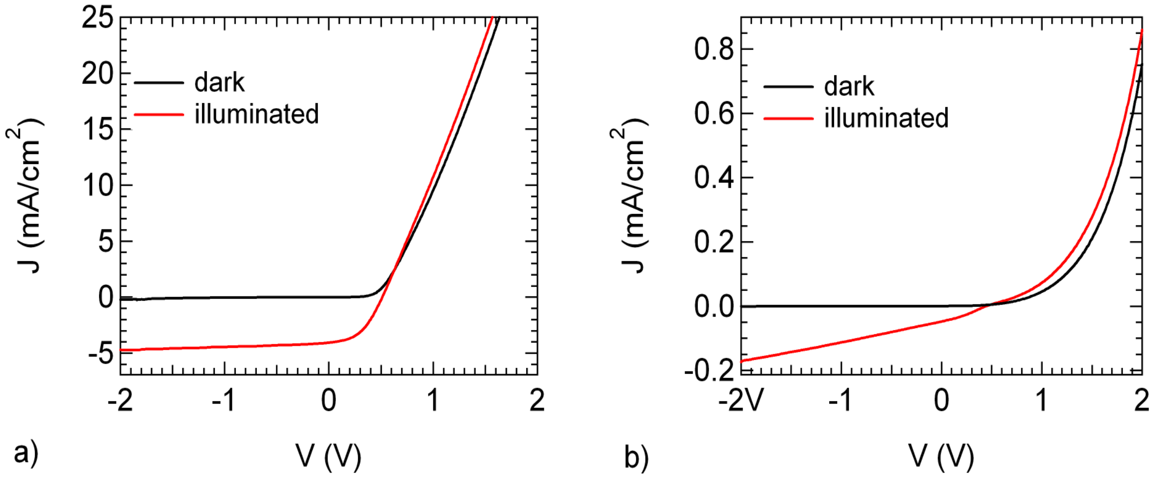

Figure 6.7: *a) IV-characteristics of the ITO/ZnPc/C_{60}/BCP/Al solar cell "solar_2new" in the dark and under white light illumination (halogen lamp, P ≈ 100 W). The IV-curves of the as-prepared sample were recorded under nitrogen atmosphere (0.3 ppm oxygen). b) IV-curves of the same sample during the EDMR measurements one day after preparation. The sample shows degradation.*

6.3.2 Pulsed EDMR Results for Solar2new

In section 6.2.3 the solar cell "Solar1new" was investigated using pulsed EDMR. The transient EDMR signal showed an enhancing and a quenching part, which were tentatively interpreted as two signals, namely a positive ZnPc signal and an unknown quenching one. However, enhancing and quenching components could also stem from the decay dynamics of a single spin-dependent process, which would mean that the EDMR transient is not composed of two signals. In this section the question about the two components of the EDMR signal is decided using a similar device "solar2new". Since high microwave powers (power attenuation: 10dB - 0dB) lead to broadening in the linewidth of EDMR signals, an experiment with low microwave power (24 dB) was performed with the device solar2new. This could be achieved by a higher sensitivity due to an improved amplification. This experiment could reveal the intrinsic lineshape of the signal. Fig.6.8 a) shows the transient photocurrent change vs. time after a microwave pulse of 320 ns (horizontal axis) and vs. the magnetic field (vertical axis). The red and blue areas denote the enhancement and the quenching signal, where the latter is the dominant one under these illumination conditions. The red spot exhibits a nearly triangular

Table 6.6: *IV-parameters of the ITO/ZnPc/C$_{60}$/BCP/Al device (solar2new) under illumination (halogen lamp, P ≈ 100 W) in nitrogen atmosphere*

J_{sc} (mA/cm^2)	V_{oc} (V)	η (%)	ff (%)
4.1	0.51	0.95	45.3

silhouette whereas the blue one is rather heart shaped.

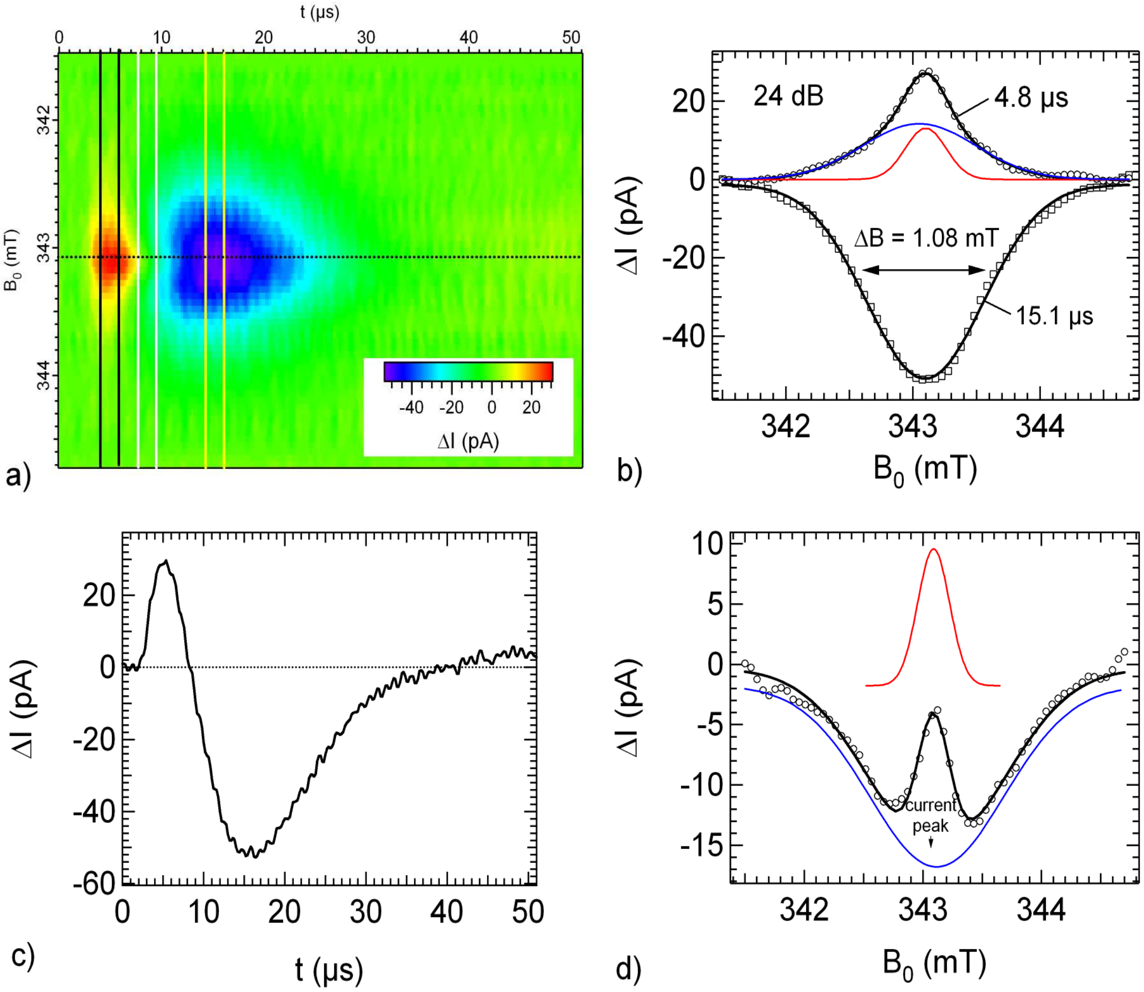

Figure 6.8: *a) Transient photocurrent change ΔI of the ITO/ZnPc/C$_{60}$/BCP/Al - device (solar2new) after a microwave pulse of 320 ns length (microwave power attenuation 24 dB, P_{mw} ≈ 1kW at 0 dB). Illumination was done by a halogen lamp (P ≈ 100 W) and a voltage of V = -1 V was applied in reverse bias direction. The current enhancement is followed by a quenching. The markers indicate the positions of the line profiles shown in b), c) and d). Two lines of the same colour mark the time interval where the spectra are averaged. b) The current enhancing signal according to the black markers is much narrower in linewidth than the quenching signal (yellow markers) and could be fitted with two Gaussian functions. c) The current change ΔI vs. time at the center of the resonance (dotted line). d) A superposition of both signals is observed near the zero crossing of the transient (white markers in a)) and was fitted by two Gaussian lines.*

This is the result of the overlap between a narrow positive signal and a broad quenching one. A cut through the overlap region (Fig.6.8 d)) shows the superposition of the signals. The spectra of both signals are depicted in part b) of Fig.6.8 and reveal the different lineshapes and linewidths of the signals. The positive signal is narrow and could be reproduced by two Gaussian lines, whereas the negative signal is broad and could be fitted by a single Gaussian profile; the fit parameters are summarized in Table 6.7. The overlap of the negative with the positive signal in Fig.6.8 d) as well as the distinct spectral features of the components prove the presence of two distinct EDMR signals in the ITO/ZnPc/C_{60}/BCP/Al device "solar2new". Since both devices (solar1new and solar2new) were prepared in the same manner, it can be assumed that the same holds true for the EDMR signals in solar1new.

Table 6.7: EDMR Fit parameter of solar2new in Fig.6.8 b).

EDMR signal	FWHH ΔB (mT)	g-factor
pos. component a	0.38	2.0023(5)
pos. component b	1.05	2.0026(5)
negative signal	1.08	2.0023(5)

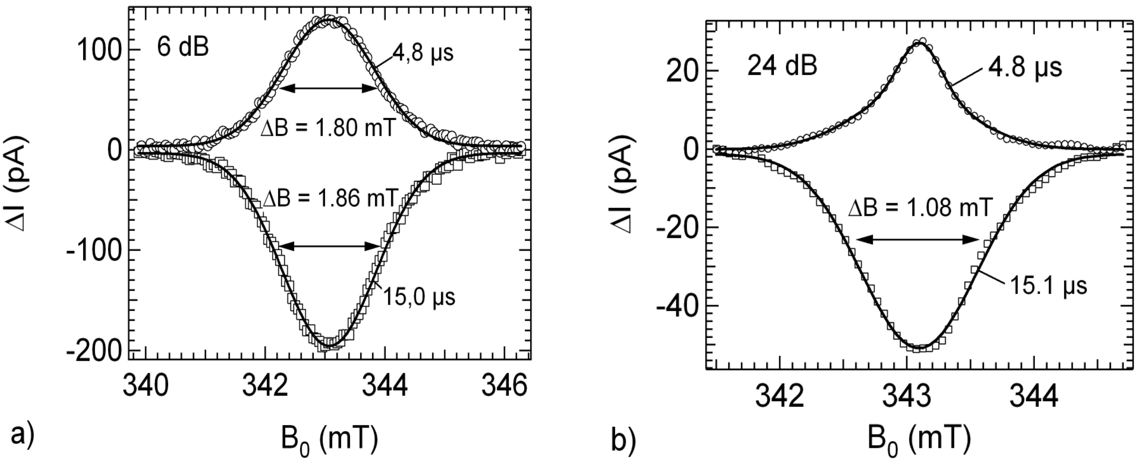

Figure 6.9: Comparison between the negative and positive EDMR spectra of sample solar2new at high microwave power (power attenuation: 6 dB, graph a)) and at low microwave power (power attenuation: 24 dB, graph b)). All spectra were recorded at V = -1V in reverse bias, pulse length: 320 ns, illumination P $\approx$ 100 W.

If this is the case, we have to answer the question why the positive and the negative signal in "solar1new" have similar linewidth (see Fig.6.5 a)), which is not the case in solar2new. Microwave power broadening probably leads to equal linewidth in the EDMR spectra of solar1new, which were recorded at higher microwave powers (power attenuation 10 dB) than in solar2new. A pulsed EDMR experiment performed with solar2new at higher microwave power (power attenuation: 6 dB) indeed reveals that the linewidth of the signals become equal under these circumstances. Fig.6.9 shows the positive and negative EDMR spectra of solar2new at two different microwave powers. In the high microwave power measurement the linewidth of the negative and positive spectra are almost equal, whereas at low microwave power the spectra show distinct linewidth. This result strengthens the assumption that the origin of the EDMR signals in both solar cells is the same. Keeping this in mind we can return to the discussion of the negative EDMR signal under forward bias conditions (§ 6.2.4). A comparison of the negative EDMR signal in Fig.6.8 b) (reverse bias) with the one in Fig.6.6 a) (forward bias) reveals the dissimilarity of both, lineshapes and linewidth, although these signals were both recorded at low microwave power. This supports the earlier attribution of the EDMR enhancement signal to ZnPc, whereas the quenching signal (reverse bias) must be due to a second spin-dependent process. In forward bias, the ZnPc signal changes sign and the quenching signal disappears.

6.3.3 EDMR Light Intensity Dependence

Fig.6.10 shows the transient EDMR signals of the ITO/ZnPc/C_{60}/BCP/Al - device “solar2new” at three different light intensities. The current transients are fitted with three exponential functions, with parameterswhere listed in Table 6.8. At low light intensities the current enhancement is stronger than the quenching, whereas at high intensities the quenching signal is the dominant one. It is not quite clear whether the intensity dependence stems from different EDMR signal amplitudes or from different recombination dynamics. If constant decay times 1/D are assumed and only the amplitudes are varied the exponential fit leads to unsatisfactory results. As a consequence, the decay times were also varied, assuming that the dynamics of the spin-dependent processes depend on light intensity. This is straight-forward if spin-dependent recombination is assumed to be at the origin of the EDMR signals, since recombination is an intensity-dependent process. Since the generation rate increases with increasing light intensity, an equilibrium is established at higher recombination rates. Eq.1.37 relates the time constants of the exponential signal decay to the dissociation and recombination rates in the spin pair ensemble.

Table 6.8: *EDMR fit parameters for the ITO/ZnPc/C_{60}/BCP/Al - device “solar2new” in Fig.*6.10.

light power	25W			100W			200W		
EDMR signal	a) pos.	a) neg.	-	b) pos.	b) neg.	b) pos.	c) pos.	c) neg.	c) pos.
1/D (µs)	7.1	11.7	-	6.4	9.1	25.0	5.5	7.70	11.1
amplitude (nA)	1.0	-0.5	-	4.8	-3.8	0.2	25.4	-32.6	10.1

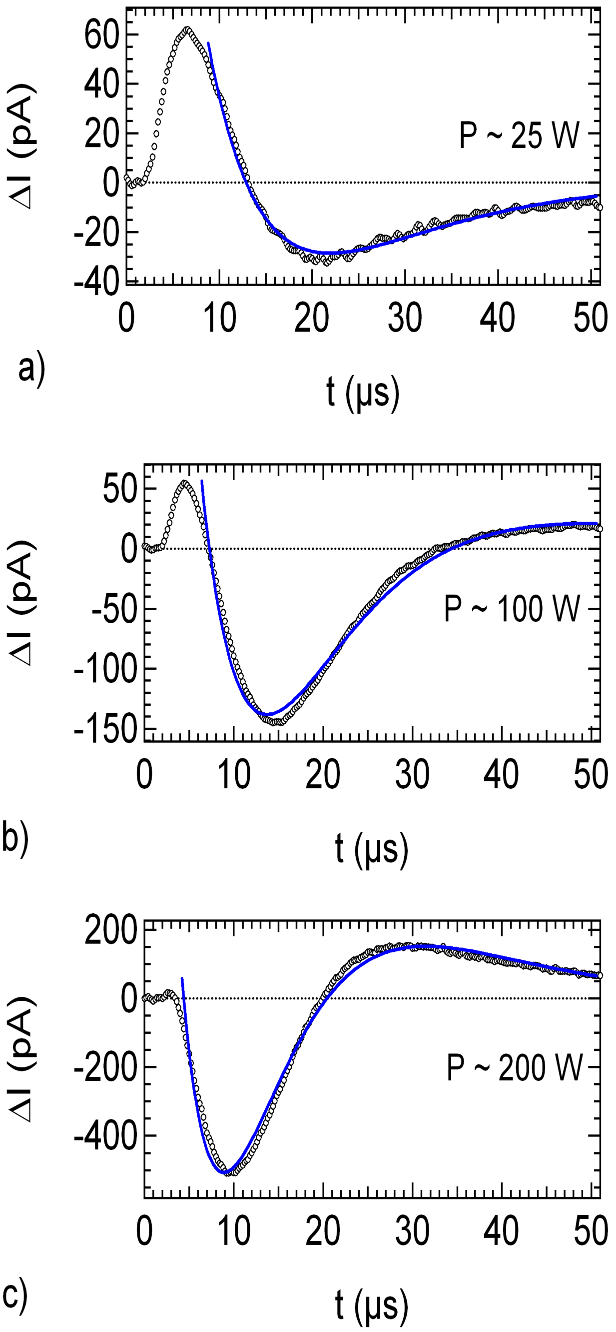

Figure 6.10: *Transient photocurrent changes ΔI of the ITO/ZnPc/C_{60}/BCP/Al - device (solar2new) after a microwave pulse of 320 ns length (microwave power attenuation 9 dB, $P_{mw} \approx$ 1kW at 0 dB). A voltage of V = -1 V was applied in reverse bias direction. The light intensity was varied. a) The power of the halogen lamp ($P \approx 100$ W) was reduced by a neutral filter (Schott NG 4) with a transmission coefficient of $T \approx 25$ %. b) Without filter ($P \approx 100$ W). c) The power of the halogen lamp was increased to $P \approx 200$ W. The blue lines are triple exponential fit functions (parameters see Table 6.8).*

A careful examination of the fit parameters in Table 6.8 shows that the time constants of the positive and negative components decrease from a) to c) and thus with increasing light intensity. The main enhancement signal is almost not observed at the highest light intensity (Fig.6.10 c)), because it becomes faster than the current detection. In contrast, the positive slow component is not observed at the lowest light intensity. As mentioned before, a full decomposition of the signal according to Eq.1.37 is hampered by unknown circuit response times. In future experiments, these might be determined independently by pulsed current measurements. It remains unclear if the slow component is an additional process or if it pertains to the response behavior of the negative signal. However, the intensity study shows quite clearly, that at least two distinct processes are present in the solar cell.

6.4 Rabi Beat Oscillations

Spin nutation experiments are carried out by integrating the current changes after resonant microwave pulses of varied pulse length. In the following experiment these spin nutations were recorded at 32 magnetic fields covering the whole EDMR spectrum of the ITO/ZnPc/C$_{60}$/BCP/Al device solar1new. The integration was carried out over a time interval that covers the current enhancing part of the EDMR signal in Fig.6.5 b) (3 µs - 7 µs). The result is illustrated in the colour plot of Fig.6.11 a1), where the integrated current changes under illumination are plotted vs. the magnetic field (vertical axis) and vs the pulse length τ (horizontal axis). In Fig.6.11 b1), the spin nutation was simulated by an expression that is related to the state density changes given in Eq.1.52. The resulting expression for the state density changes of a spin pair including a Gaussian Larmor distribution $\phi(\omega_L) = exp(-(\omega_{mw} - \omega_L)^2/\Delta^2)$ of linewidth Δ yields:

$$\Delta_{eff}(\tau, \omega_{mw}) = \int_{-\infty}^{+\infty} \sum_{n=1,\ldots,3} A_n e^{-\gamma_n \tau} e^{-\frac{(\omega_{mw}-\omega_L)^2}{\Delta_n^2}} J_0\left(2\kappa_n \tau \sqrt{(\gamma B_1)^2 + (\omega_{mw} - \omega_L)} - \xi\right) d\omega_L \tag{6.1}$$

where A$_n$ is the amplitude, κ_n = 1/2 for spin pairs with large Larmor separation, and κ_n = 1 for those with small Larmor separation. A damping term with damping constant γ_n was added to simulate the dephasing and ξ is a phase shift parameter. In a simple approach, the spin pair ensemble was assumed to have a common Larmor distribution as illustrated in Fig.5.4. This ensemble is discribed by the first term (n = 1) in Eq.6.1. The second term (n = 2) is needed to substract the fraction A_2 of locked spin pairs from those that are not locked ($A_1 - A_2$). It is assumed here for simplicity that they also have a Gaussian Larmor distribution, but a smaller linewidth and amplitude $A_2 = -bA_1$, ($b = 0.84$). The third term (n = 3) finally adds the spin pairs with small Larmor separation ($A_3 = -A_2$) but with the doubled nutation frequency expressed by κ_3 = 1. The second and the third term differ only in value of κ and the sign of the amplitude and therefore replace a fraction of spin pairs with large Larmor separation (κ_2 = 1/2) by the same amount of spin pairs with small Larmor separation (κ_3 =1).

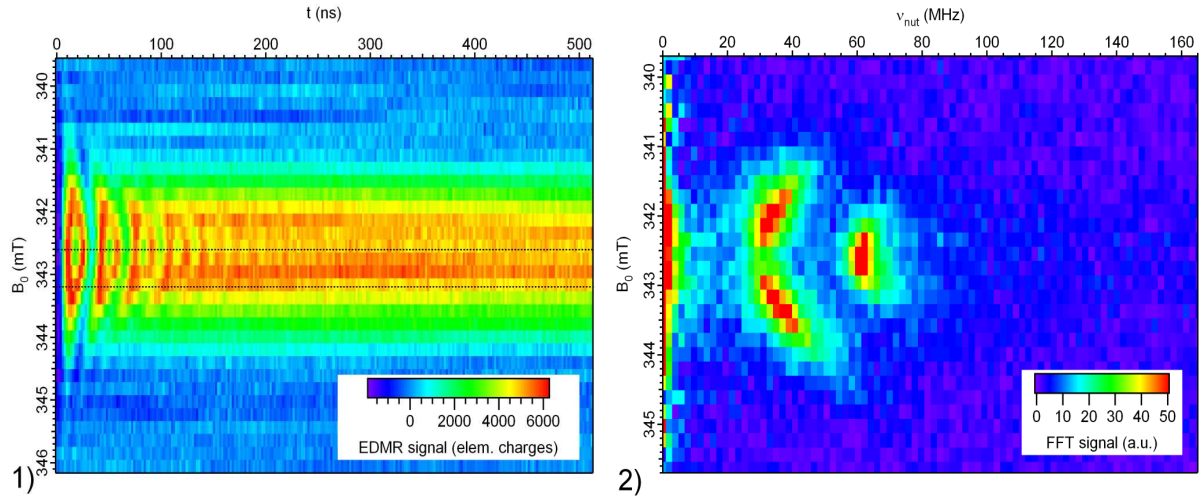

(a) *1) Rabi beat oscillations (power atten.: 3dB) vs magnetic field in an ITO/ZnPc/C$_{60}$/BCP/Al device (solar1new) under illumination with a halogen lamp (P ≈ 100 W). An offset current of I = 500 nA was applied in reverse bias direction. The integrated current changes (integration window: 4 µs - 7µs) are given in elementary charges. The oval shaped pattern is due to the double Rabi-frequency component at the center of the resonance. The dashed lines indicate the line profiles in Fig.6.12. 2) Fourier transform (time domain) of 1).*

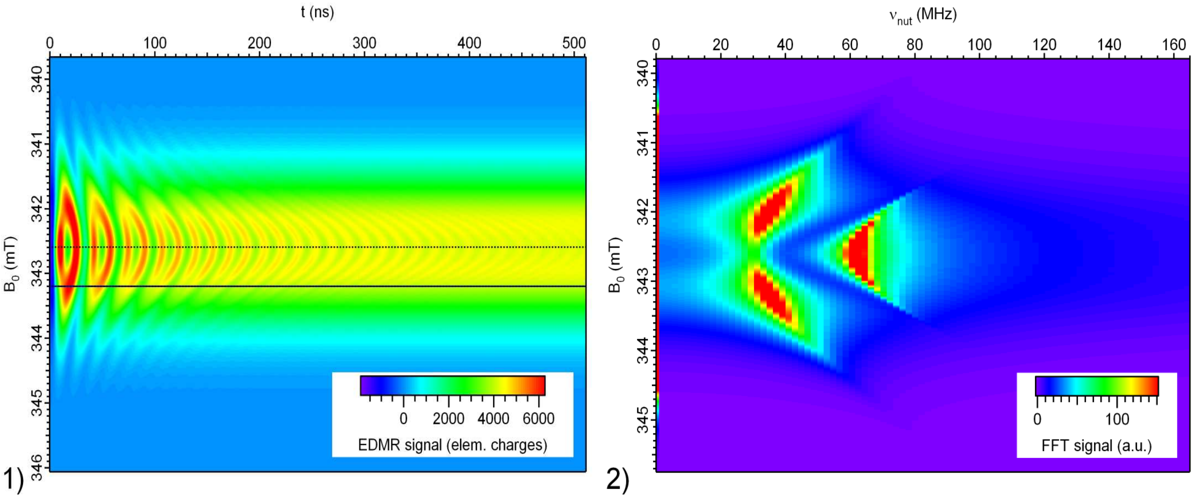

(b) 1) S*imulation of the Rabi-oscillations in a) containing Bessel functions of the first kind and Gaussian shaped spectroscopic functions. The ensemble of spin-locked pairs was simulated by replacing a Gaussian shaped fraction with nutation frequency* Ω *by the same fraction but with nutation frequency of 2* Ω*, details are given in the text. The dashed lines indicate the line profiles in Fig.6.12. 2) Fourier transform of 1).*

Figure 6.11: Rabi beat oscillations

The line profiles in Fig.6.12 show the simulation in comparison to the data for two different magnetic fields B$_0$. The simulation parameters (see Table 6.9) were optimized by fitting the differentiated data with the integrand of Eq.6.1.

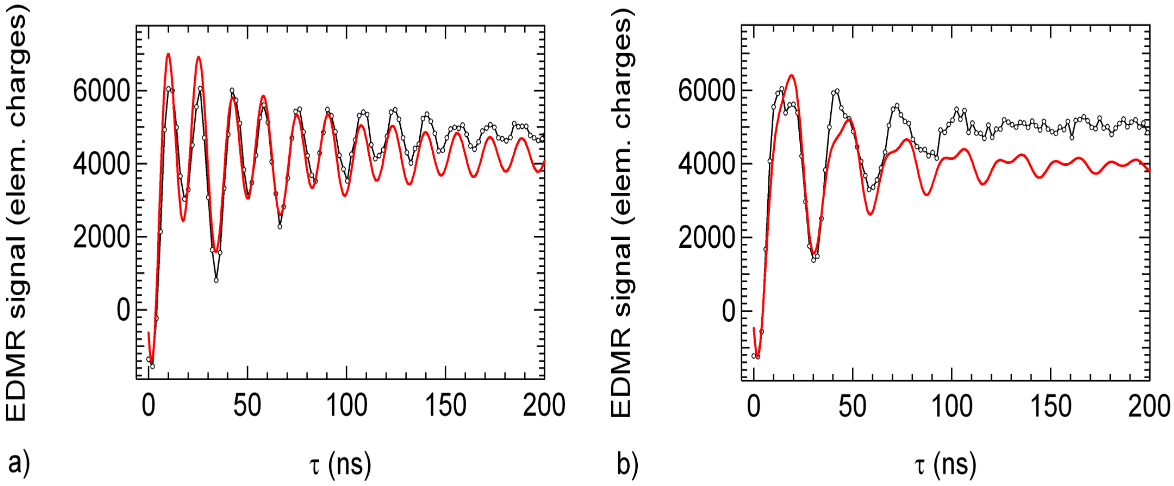

Figure 6.12: *Line profiles indicated in Fig.6.11 by the dashed lines. The data (open circles) is shown together with the global simulation (red lines). a) Signal at center magnetic field* B_0 *= 342.6 mT. The spin nutation exhibits two frequency components. b) Line profile at* B_0 *= 343.2 mT. The spin oscillation shows mainly one nutation frequency. Note that only a single parameter set was used for both curves (see Table 6.9).*

The spin nutation characteristics of the sample is reproduced satisfactorily by the simulation, however the nutation curve in Fig.6.12 b) shows an upward bending that cannot be simulated by Eq.6.1 and that we attribute to background noise. The damping coefficient of the pairs with large larmor separation γ_1 is larger than γ_3 for the spin locked pairs and leads to the conclusion that the oscillation of these spin pairs decays faster than the oscillation of the spin locked pairs.

The Fourier transform of the spin nutations shown in Fig.6.11 a2) have a parabolic shape that stems from the off-resonant contributions of the nutation frequency $\Omega = \sqrt{(\gamma B_1)^2 + (\omega_{mw} - \omega_L)^2}$. There are two parabolas associated with the two frequency components of the spin pairs (small Larmor separation and large Larmor separation). At the resonance center the amplitude of the lower frequency component is weakened by the presence of the high frequency component. The broadened shape of the parabolas is due to damping of the spin nutation by a dephasing process.

Table 6.9: *Simulation Parameters according to Eq.6.1 of the Rabi beat oscillation in Fig.6.11 with* ξ *= 4.9 and* $\frac{1}{2\pi}\gamma B_1$ *= 30.64 MHz.*

A_1	5.87 x 10^{12}	A_2	- 4.93 x 10^{12}	A_3	4.93 x 10^{12}
Δ_1 (mT)	1.12	Δ_2 (mT)	0.54	Δ_3 (mT)	0.54
κ_1	1/2	κ_2	1/2	κ_3	1
γ_1 (sec^{-1})	1.5 x 10^7	γ_2 (sec^{-1})	1.5 x 10^7	γ_3 (sec^{-1})	5 x 10^6

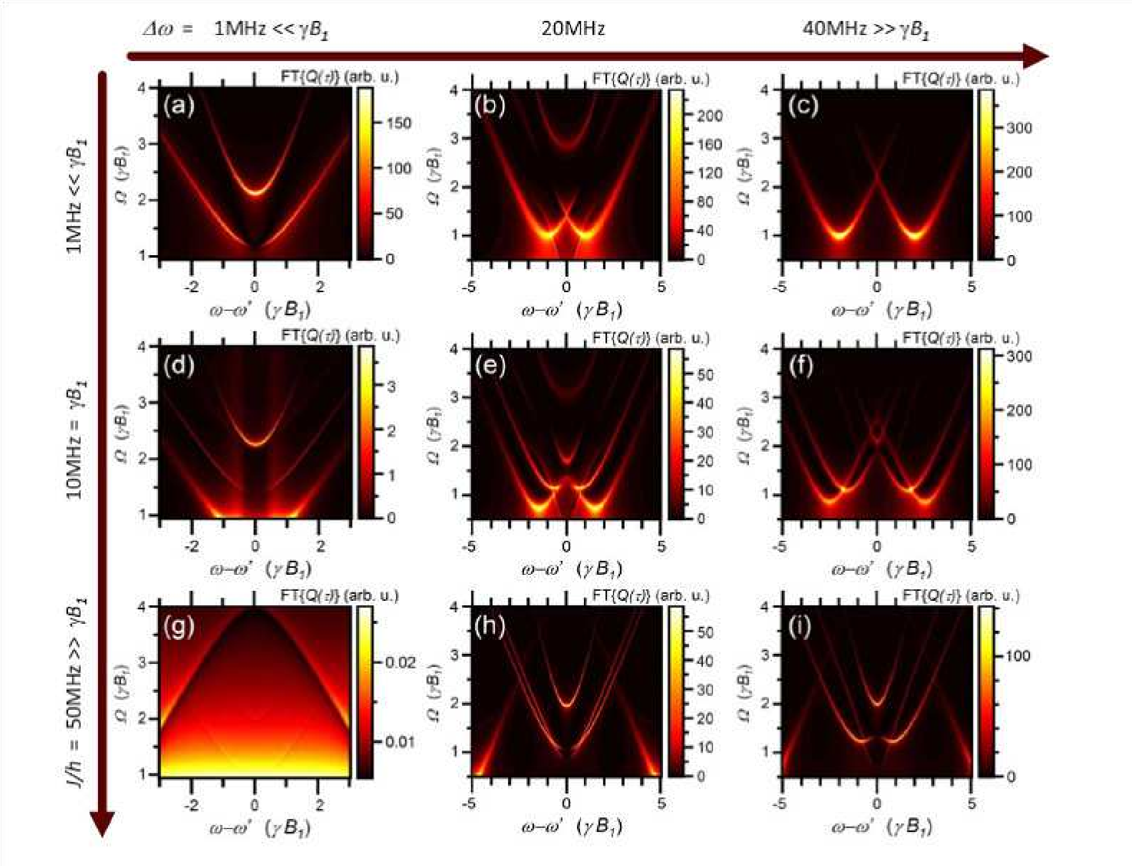

Figure 6.13: *Plots of the Fourier transform FT{Q(τ)} of the observable Q(τ) as a function of the driving frequency normalized resonance offset* $\frac{\omega-\omega'}{\gamma B_1}$ *and the Rabi frequency* $\frac{\Omega}{\gamma B_1}$*, taken from A. Gliesche et al. [128]. Datasets are represented in arbitrary but equal units (see color scale legends) for 3 different Larmor separations* $\Delta\omega$ *and for three different coupling strengths J/h. They were simulated with Larmor separations of* $\Delta\omega$ *= 1 MHz .*

In a theoretical study of A. Gliesche et al [128] the Fourier transforms of spin nutations in pODMR and pEDMR experiments were calculated. The calculations illustrated in Fig.6.13 include different coupling strength and Larmor separations within the spin pair ensemble, which leads to different patterns in Fourier space. A comparison of the EDMR results of the ITO/ZnPc/C_{60}/BCP/Al device (solar1new) given in Fig.6.11 with the calculated patterns of Gliesche reveals similarities between case (a) in Fig.6.13 and the EDMR signal of solar1new. Since damping (dephasing) terms are not included in the simulation of Gliesche et al., their simulations are much narrower than the experimental results of solar1new. In order to exclude the effect of broadening due to the dephasing, the simulation in Fig.6.11 b2) was repeated with all damping coefficients set to zero ($\gamma_1 = \gamma_2 = \gamma_3 = 0$). The result is illustrated in the left graph of Fig.6.14 and now shows a striking resemblance to pattern (a) of Gliesche depicted in the right graph of Fig.6.14. Hence the conclusion can be drawn that the exchange coupling of the spin pairs contributing to the enhancing EDMR signal in solar1new is very small (J/h $\approx$ 1 MHz).

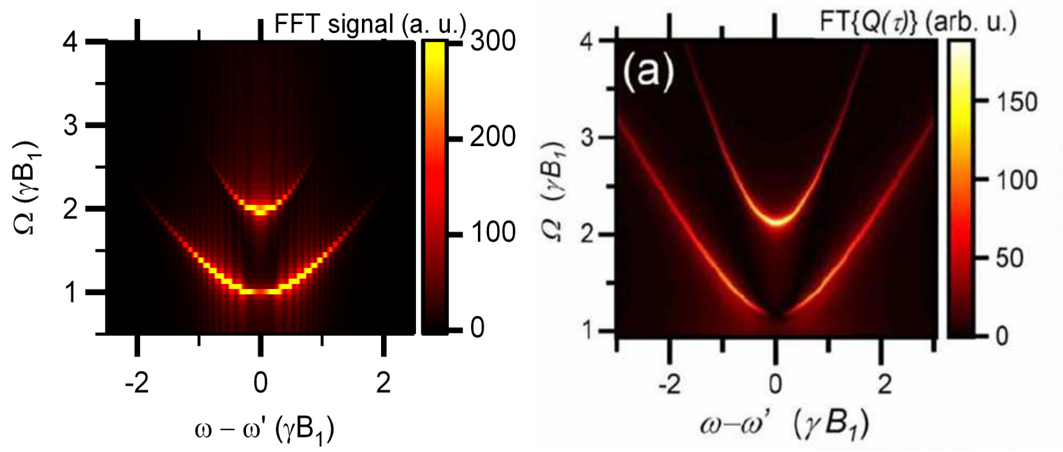

Figure 6.14: *Left graph: Simulation of Fig.6.11 b2) with damping coefficients* $\gamma_n = 0$. *Right graph: Fourier transform FT{Q(τ)} of the observable Q(τ), taken from A. Gliesche et al. [128] (graph (a) in Fig.6.13), simulated with a Larmor separation of* $\Delta\omega = 1$ *MHz and an exchange coupling strengths within the pairs of* $J/h = 1$ *MHz.*

6.5 Rabi Beat Oscillations of the Quenching Signal

Spin nutation experiments contain information about the species observed in an EDMR experiment. The spin-locking behavior of the positive EDMR signal in the device solar1new revealed that the origin of the signal is a spin pair ensemble with close g-values (small Larmor separation) and weak exchange coupling. In order to gain more information about the origin of the negative EDMR signal in the ITO/ZnPc/C$_{60}$/BCP/Al device "solar2new" spin nutation experiments were carried out with an integration window that covers the negative part of the EDMR transient given in Fig.6.15 a) (blue shaded area). The result is depicted in graph c) of Fig.6.15 and shows the presence of the doubled Rabi-frequency associated with the phenomenon of spin-locking. The amplitude of the high frequency component is however much smaller than the one of the low frequency component. This is in contrast to the spin nutation of the positive signal, shown in Fig.6.15 b) where the high frequency component is dominant. Since the frequencies of the components are identical in the negative and the positive Rabi-oscillation (Ω_1 = 15.6 MHz, Ω_2 = 31.2 MHz) an equal microwave magnetic field B_1 can be assumed in both measurements. Therefore the distinct spin-locking behavior of the positive and the negative spin nutation signal is probably caused by different Larmor separations of associated the EDMR signals. The positive EDMR signal in Fig.6.9 b) indeed shows a much smaller linewidth than the negative one, which indicates a narrower Larmor distribution for the positive signal associated with a smaller averaged Larmor separation in the spin pair ensemble.

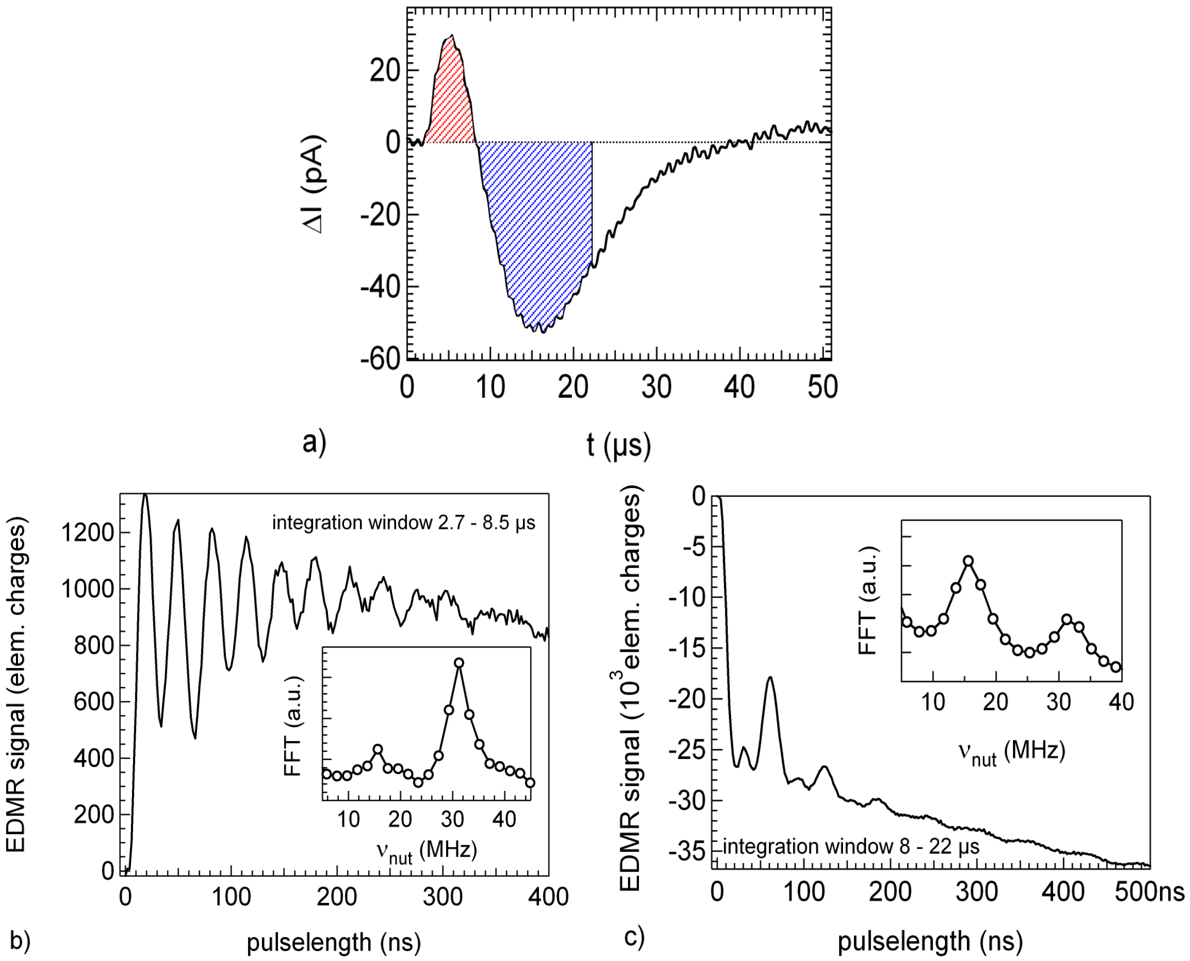

Figure 6.15: *Integrated photocurrent changes of the ITO/ZnPc/C_{60}/BCP/Al device (solar2new) as a function of the pulse length (microwave power attenuation: 3 dB). A voltage of V = -1 V in reverse bias direction was applied to the sample. The integration windows according to the positive and the negative parts are indicated in a) by the red and blue areas. b) Rabi beat oscillations of the positive signal under $P \approx 100$ W white light illumination. c) Rabi beat oscillation of the negative signal under $P \approx 200$ W white light illumination.*

Discussion

The Enhancement Signal

The EDMR experiments in ITO/ZnPc/C_{60}/BCP/Al solar cells reveal two signals, one that enhances and one that quenches the photocurrent. Both signals are absent in dark EDMR measurements and must therefore be photoinduced features. The enhancing EDMR signal has a lineshape and linewidth similar to the ZnPc signal. Furthermore, both signals exhibit spin-locking behavior and reverse their signs in forward bias. From these findings the positive EDMR signal in the solar cell is attributed to the ZnPc material. The positive EDMR signal in ZnPc single layer devices was interpreted in § 4.1.2 as a spin-dependent recombination of accumulated charges at the oxidized ZnPc/Al electrode. A similar charge accumulation in the solar cell could happen at the ZnPc/C_{60} hetero-interface when the conductivity of the C_{60}- layer is strongly reduced upon contact with air. In this case, the high resistance of the C_{60} layer would hinder the electron extraction in reverse bias and under open circuit conditions. The electrons piled up at the hetero-interface would form an additional barrier for the electrons that move towards the C_{60}-layer. Thus recombination would reduce the number of accumulated charges and the photocurrent is enhanced at resonance. Since in forward bias the electrons move towards the ITO contact, no accumulation happens and the spin-dependent recombination leads as usual to a current quenching signal. This would explain the sign reversal of the EDMR signal in forward bias.

The Quenching Signal

The quenching EDMR signal has a light intensity dependence different from the enhancement signal and shows a weaker spin-locking. The lineshape and linewidth, as well as the spin nutation behavior, differ significantly from the EDMR signals measured in C_{60} thin films in previous works [2, 4]. We can therefore exclude the C_{60} bulk material as origin for the quenching signal. Since the ZnPc single layer devices never showed two EDMR signals with opposite sign together in one sample, the quenching signal seems also not to stem from the ZnPc bulk material. The solar cell however has an interface that was not investigated in the single layer devices so far, the ZnPc/C_{60}-interface. At this point it is necessary to take into account the charge generation process, which is assumed to stem from exciton splitting at the hetero interface (ZnPc/ C_{60}). This process ends up with negatively charged C_{60} and a positively charged ZnPc radical. This radical pair could be a precursor for a new spin-dependent recombination mechanism, which explains its absence in the single-layer devices. The spin-dependent recombination of such a radical pair competes with dissociation and thus should quench the current, as observed in the experiment. In solar1new the reverse bias quenching signal vanishes under forward bias conditions. This behavior can also be explained, since in forward bias the dissociation of the radical pair is suppressed by the external electric field and thus spin-dependent recombination of the radical pair has no influence on the photocurrent anymore.

Chapter 7

Summary and Outlook

This work investigates the role of spin-dependent processes in the electrical transport in organic semiconductor devices by means of electrically detected magnetic resonance (EDMR). For this purpose, a systematic IV-characterization and degradation analysis was combined with a detailed continuous wave and pulsed EDMR study. Zinc phthalocyanine (ZnPc) thin film devices with different electrode materials and geometries serve as a model system. Two device structures with different transport and degradation mechanisms were investigated, a coplanar Au/ZnPc/Au sample and a sandwich type ITO/ZnPc/Al device. After correlating the spin-dependent processes with the transport mechanisms in the single layer devices, the EDMR and transport studies were extended to the more complex bilayer ZnPc/C_{60}-solar cells.

Transport and Degradation Study

The transport study begins with a comparison of the coplanar with the sandwich type device. Whereas at low voltages the coplanar ZnPc device is dominated by bulk transport with Ohmic IV characteristics, the transport in the sandwich device is controlled by a Schottky barrier at the aluminum contact. Both samples show SCL-currents with exponential trap distribution in the high voltage limit, revealing the typical bulk transport mechanism of the ZnPc material. The degradation studies show that the sandwich device suffers from an oxidation of the aluminum contact, exhibiting “Schottky emission” IV-characteristics. The additional oxide layer leads to a pronounced rollover (kink) in the photocurrent voltage characteristics that can be explained with an extraction barrier for electrons. The kink moves towards the negative voltage regime with further degradation. If the oxide layer reaches a thickness of approximately 70 Å it completely controls the device current. It was found that the aluminum oxidation can be prevented by using a more effective encapsulation method, using a glass cover plate and a special UV-glue.

EDMR Study

By correlating the IV-characterization with EDMR experiments as a function of the light intensity, the dominant spin-dependent process in the coplanar ZnPc device was determined to be polaron recombination. In the sandwich device, the ZnPc EDMR signal reverses sign but does not otherwise change its spectroscopic signature. This shows that the spin-dependent process is similar in both cases but embedded in a different transport mechanism. EDMR and IV-measurements indicate that negative polaron accumulation at the oxidized ZnPc/Al contact is the reason for an extraction barrier in the degraded device. In order to understand the EDMR sign change, a model is proposed in which recombination can lead to a photocurrent enhancement. The model is verified by voltage dependent EDMR study in the sandwich device, where it explains convincingly different EDMR signs under forward and reverse bias conditions. Furthermore, it was found that the polaron recombination model can also be applied to explain a negative magnetoresistance effect under illumination observed in the coplanar device. The spectroscopic features of the EDMR signal were investigated by detailed lineshape and phase analysis taking into account the effect of exchange coupling among the spin pairs.
In the pulsed EDMR analysis, “Rabi beat oscillations” due to non-selectively excited spin pairs were observed for the first time in EDMR of organic materials. This phenomenon consists of a doubled Rabi-frequency that appears when two pair spins are excited at the same time. The microwave power dependence of the beat oscillations were studied as well as th e effect on EDMR line shapes after short microwave pulses.

Application to Solar Cells

Further EDMR and transport studies concentrated on the more complex bilayer ZnPc/C_{60} solar cells. Two EDMR signals were found in these cells corresponding to an enhancement of the photocurrent in one case and a photocurrent quenching in the other case. In a detailed pulsed EDMR study the two signals revealed different sensitivities to light and distinct power-broadening behavior and could thus be identified as two different spin-dependent processes. The photocurrent enhancing signal could be attributed to polaron recombination in the ZnPc layer. The positive sign of the signal indicated a charge accumulation at the ZnPc/C_{60}-interface, as observed in the single layer device. This charge accumulation was assumed stem from a degradation of the C_{60}-layer due to oxygen, which leads to oxygen related defects, that reduce strongly the C_{60} bulk conductivity. The degradation could be verified by an IV-characterization. The photocurrent quenching EDMR signal was tentatively assigned to a charge transfer complex (ZnPc^{+}, C_{60}^{-}) at the heterointerface. This indicates that spin-dependent recombination happens during the exciton dissociation process at the ZnPc/C_{60} -interface.

Conclusions and Outlook

This work has bridged a gap between transport and degradation and spin-dependent processes. The ability of spectroscopic identification combined with the high sensitivity of the EDMR measurements could help to reveal degradation and transport mechanisms in different kind of organic devices. The attribution of the EDMR signals to the underlying microscopic processes is a difficult task and was supported by a fundamental transport study using mainly current voltage measurements. In general, the combination of EDMR with other characterization techniques as for example ODMR, TOF, electroluminescence or IV-analysis improves the understanding of the microscopic processes observed in EDMR and how they are involved in current transport. If the correlation between EDMR signals and electrical transport is better understood, this technique provides a powerful tool to identify transport and loss mechanisms in semiconductor devices under realistic working conditions. Furthermore, the encapsulation technique shown in §3.2.3 pave the way to further studies on intact ZnPc and solar cell devices, which would be useful to confirm the transport and degradation model developed in this work.

List of Publications

- S. Schaefer, S. Saremi, K. Fostiropoulos, J.Behrends, K. Lips, W. Harneit, Phys. Stat. Sol. (b), **Spin-dependent processes in ZnPc single layer devices**, Phys. Status Solidi B 246, No. 11–12, 2844–2848 (2009)

- S. Schaefer, S. Saremi, K. Fostiropoulos, J.Behrends, K. Lips, W. Harneit, **Electrical detection of coherent spin pair oscillations in ZnPc devices**, Phys. Stat. Sol. (b) 245, No. 10, 2120 (2008)

- S. Schaefer, K. Huebener, W. Harneit, C. Boehme, K. Fostiropoulos, H. Angermann, J. Rappich, J. Behrends, K. Lips, **Thin film engineering for N@C60 quantum computers: Spin detection and device patterning approaches**, Sol. Stat. Science 10, 1314, (2008)

- W. Harneit, K. Huebener, B. Naydenov, S. Schaefer, M. Scheloske, **N@C60 quantum bit engineering**, Phys. Stat. Sol. (b) 244, No 11, 3879, (2007)

- W. Harneit, C. Boehme, S. Schaefer, K. Huebener, K. Fostiropoulos, K. Lips, **Room Temperature Electrical Detection of Spin Coherence in C60**, Phys. Rev. Lett. 98, 216601 (2007)

Zusammenfassung

In einer gemeinsamen IV-Kennlinien- und EDMR-Analyse wurden elektrische Transport- und Degradationseigenschaften in organischen Halbleiter-Bauelementen untersucht. Zunächst wurden Zink-Phthalocyanin(ZnPc)-Einzelschichten mit verschieden Kontakten hergestellt. In einer Probe wurden koplanare Goldkontakte benutzt (Au/ZnPc/Au), während die andere eine Vertikalstruktur aus ITO/ZnPc/Al aufweist. Der Einfluss dieser Kontakte auf den elektrischen Transport wurde dazu genutzt, die Ergebnisse der EDMR in den Transportmechanismus richtig einzuordnen und zu interpretieren. Mithilfe der aus den Einzelschicht-Bauelementen gewonnenen Erkenntnisse wurden in einem zweiten Schritt komplexere ZnPc/C_{60} Zweischicht-Solarzellen untersucht.

Die Transport-Analyse ergab bei niedrigen Spannungen Ohmsche Kennlinien fur die Probe mit koplanaren Kontakten, während in der Vertikalstruktur der Strom durch eine Schottky-Barriere am Aluminium-Kontakt begrenzt ist. Bei hohen Spannungen dagegen zeigen beide Proben raumladungsbegrenzten Transport unter Einwirkung von exponentiell in der Bandlücke verteilten Defekt-Zuständen. Die Degradations-Studien an der ITO/ZnPc/Al Probe zeigen eine Oxidation der Aluminium-Elektrode. Dies drückt sich unter anderem in einer Kennlinie aus, die auf Schottky-Emission hinweist, ein Transport Prozess, der häufig in Metall-Isolator-Halbleiter-Übergängen auftritt. Dieser Degradationsprozess lässt sich durch eine effektive Verkapselung mit einem Glass-Plättchen und UV-Kleber verhindern. Die Ergebnisse der IV-Kennlinien-Analyse der Solarzellen weisen ebenfalls auf eine Sauerstoff-bedingte Degradation hin, bei der der Widerstand der Fullerenschicht durch Sauerstoff-induzierte Defektzustände in der Bandlücke stark ansteigt.

Aus den EDMR Messungen geht hervor, dass wahrscheinlich Polaronen-Rekombination für die Signale in den oben genannten organischen Materialien verantwortlich ist. Diese wirkt sich jedoch verschiedenartig auf den Strom der einzelnen Proben aus. Als Folge wird ein ein negatives EDMR-Signal in der Au/ZnPc/Au Probe und ein positives in der Vertikalstruktur gemessen. Die Ergebnisse der Transport-Studie weisen auf eine Ladungs-Ansammlung an der Al-Elektrode hin. Daher wurde ein Modell vorgeschlagen, bei dem die Rekombination dieser akkumulierten Ladungsträger eine Stromerhöhung bewirkt. Dieses Model wurde in spannungsabhängigen Messungen an der Vertikalstruktur bestätigt, in denen es erfolgreich unterschiedliche Vorzeichen des EDMR-Signals in Durchlass und in Sperr-Richtung erklären konnte.

Die EDMR-Messungen in den Zweischicht-Solarzellen zeigen ein ähnliches Signal, wie in den ITO/ZnPc/Al-Proben. Es wird daher eine ähnliche Ladungs-Akkumulation wie in der Einzelschicht-Probe erwartet, die wahrscheinlich während der Degradation am Heteroübergang zustande kommt. Ein weiteres aber negatives EDMR Signal lässt sich vorerst einer Rekombination innerhalb eines Radikalpaares ($ZnPc^+/C_{60}^-$) am Heteroübergang zuordnen.

In den gepulsten EDMR-Messungen wurden das erste mal “Beat”-Oszillationen durch nicht selektiv angeregte Spin-Paare in organischen Materialien beobachtet. Dabei wird eine doppelte Rabi-Frequenz gemessen, wenn beide Spins eines Paares gleichzeitig angeregt werden. Dieses Phänomen, sowie der Einfluss von Austausch-Kopplung auf das EDMR Signal wurden in der Arbeit ausgiebig untersucht.

Acknowledgements

The device fabrication of all samples used in this work and a part of the IV-measurements were carried out in cooperation with Konstantinos Fostiropoulos in the departement “ Heterogene Materialsysteme” (Head: Prof. Dr. Martha Ch. Lux-Steiner) of the Helmholtz-Zentrum Berlin.
The EDMR experiments were performed in cooperation with Jan Behrends and Klaus Lips in the departement “Silizium-Photovoltaik” (Head: Prof. Dr. Bernd Rech) of the Helmholtz-Zentrum Berlin.

Danksagung

Diese Arbeit ist nicht nur das Ergebnis von emsiger Probenherstellung und ausgiebigen Messkampagnen, sondern auch von fruchtbarer Zusammenarbeit und stundenlangen, wilden, manchmal manischen Diskussionen. Deshalb möchte ich im Folgenden allen danken, die mir bei dieser Arbeit geholfen haben.

- **Wolfgang Harneit** für die beste Betreuung, die man sich vorstellen kann, wirklich manische Diskussionen, und dass er versucht hat, wirklich alles Wissen mit mir zu teilen, auch wenn ich mir nur einen Bruchteil davon merken kann. Ich habe mich jedes Jahr wie ein kleines Kind über die Adventskalender gefreut, die auf einmal auf unseren Schreibtischen standen. Danke für die tolle Zeit!

- **Prof. Martha Ch. Lux-Steiner** für die uneingeschränkte Unterstützung der Experimente und die Übernahme des Erstgutachtens dieser Arbeit.

- **Prof. Robert Bittl** für das Interesse an der EDMR und die Übernahme des Zweitgutachtens.

- **Kosta Fostiropoulos** für die unentberliche Unterstützung nicht nur bei der Probenherstellung und die unzähligen lebhaften Diskussionen und Anregungen bei griechischem Berg-Tee. Es war schöne Zusammenarbeit!

- Ein besonderer Dank geht an **Jan Behrends**, für die grandiose Unterstützung bei den EDMR Messungen und die anschließenden Diskussionen über Technik und Interpretation, sowie die wirklich viel zu seltenen Radtouren.

- Für die exzellente Zusammenarbeit bei den Solarzellen Messungen, möchte ich mich **Somaieh Saremi** bedanken. Ich denke da an lange Labor-Abende mit starkem Kaffee und zerbrechlichen Proben.

- **Nino Hatter**, für die Entwicklung einer phantastischen Verkapselung und **Eser Akinoglu** für noch unveröffentlichte Ergebnisse an N@C_{60} Proben. Beiden danke ich außerdem für die aufreibenden Beach-Volleyball turniere bei glühender Hitze.

- **Wolfgang Tress**, für die exzellenten IV-Kennlinien Simulation und viele erhellende Diskussionen über elektrischen Transport.

- Weiterhin möchte ich meiner Arbeitsgruppe danken, für die tolle Atmosphäre und die große Hilfsbereitschaft. Besonders **Simon Schönfeld**, für so lange und gute Zusammenarbeit und die schwindelerregendsten Gedankenausflüge, die ich je erlebt habe. **Olga Bäßler**, für N@C_{60} in jedweder Konzentration, viel gute Laune und die Betreuung von Anlage 1. **Jens Hauschild, Michael Scheloske, Kati Hübener, Juliane Kniepert, Christoph Oelmüller** und **Boris Naydenov** für die netten Dienstags Runden bei Kaffee und Kuchen und **Rainer Döring** für den technischen Support und das Kaffee-Maß.

- **Wolfram Schindler**, für die Unterstützung bei der Proben-Herstellung und den entspannten Paddelausflug, **Tayfun Mete** für die XRD-Messungen und die gute Stimmung.

- **Klaus Lips** für die Unterstützung bei den EDMR Experimenten und **Marin Rusu** für die Untersützung bei der IV-kennlinien Analyse.

- Bei der **Gruppe von Kosta Fostiropoulos** möchte ich mich besonders für die tolle Zuasmmenarbeit bedanken.

- Ganz besonders möchte ich zum Schluß meiner Frau **Katja** und meinen **Eltern** danken, eure Unterstützung ist von unschätzbarem Wert.

Bibliography

[1] Z.H. Xiong, D. Wu, Z. V. Vardeny, J. Shi, Nature 427, 821 (2004)

[2] W. Harneit, C. Boehme, S. Schaefer, K. Huebener, K. Fostiropoulos, and K. Lips, Phys. Rev. Lett. 98, 216601 (2007)

[3] S. Schaefer, K. Huebener, W. Harneit, C. Boehme, K. Fostiropoulos, H. Angermann, J. Rappich, J. Behrends, K. Lips, Solid State Sciences 10, 1314, (2008)

[4] S. Schaefer, diploma thesis, Freie Universität Berlin, (2006)

[5] Hans Meier, Organic semiconductors, Verlag Chemie GmbH, D-694, Weinheim, 1974

[6] R. D. Gould, Coord. Chem. Rev. 156, 237, (1996)

[7] H. Shirakawa, E.J. Louis, A.G. MacDiarmid, C.K. Chiang, and A.J. Heeger, J. Chem. Soc., Chem. Comm. 578 (1977)

[8] M. A. Lampert, P. Mark, Current Injection In Solids, Academic Press (1970)

[9] C. J. Brabec, A. Cravino, D. Meissner, N. S. Sariciftci, T. Fromherz, M. T. Rispens, L. Sanchez, and J. C. Hummelen, Adv. Func. Mat. 11, 374, (2001)

[10] J. Bardeen, Phys. Rev. 71, 717, (1947)

[11] M. Brodsky, R.S. Title, Phys. Rev. Lett. 23 (1969) 581

[12] Z.Z. Ditina, L.P. Strakhov, H.H. Helms, Sov. Phys. Semicond. 2, 1006, (1969)

[13] M. Stutzmann, S. M. Brandt, and M. W. Bayerl, J. Non Cryst. Sol. 266-269, 1, (2000)

[14] D. J. Lépine, Phys. Rev. B 6, 436, (1972)

[15] D. Kaplan, I. Solomon, and N. F. Mott, J. Physique Lettres 39, L51, (1978)

[16] F. C. Rong, W. R. Buchwald, E. H. Poindexter, W. L. Warren, and D. J. Keeble, Solid-State Electronics 34, 835, (1991)

[17] R. Haberkorn and W. Dietz, Sol. Stat. Commun. 35, 505, (1980)

[18] H. Dersch, L. Schweitzer, and J. Stuke, Phys. Rev. B 28, 4678, (1983)

[19] S. M. Brandt, dissertation, Max-Planck-Institut für Festkörperforschung Stuttgart, (1992)

[20] I. Hiromitsu, Y. Kaimori, and T. Ito, Sol. Stat. Comm. 104, 511, (1997)

[21] T. Eickelkamp, S. Roth, and M. Mehring, Molecular Physics 95, 967, (1998)

[22] C.F.O. Graeff, G.B. Silva, F. Nüesch, and L. Zuppiroli, Eur. Phys. J. E 18, 21-28, (2005)

[23] G. Li, C. H. Kim, P. A. Lane, and J. Shinar, Phys. Rev. B 69, 165311, (2004)

[24] F.A. Castro, G.B. Silva, L.F. Santos, R.M. Faria, F. Nuesch, L. Zuppiroli, C.F.O. Graeff, Journal of Non-Crystalline Solids 338 - 340, 622, (2004)

[25] G.B. Silva, L.F. Santos, R.M. Faria, and C.F.O. Graeff, Physica B 308 - 310, 1078, (2001)

[26] L. S. Swanson, J. Shinar, A. R. Brown, D. D. C. Bradley, R. H. Friend, P. L. Burn, A. Kraft, and A. B. Holmes, Phys. Rev. B 46, 15072, (1992)

[27] F. A. Castro, C. F. O. Graeff, J. Appl. Phys. 101, 083903, (2007)

[28] F. Peeters, J. T. Devreese, J. Math. Phys. 21, 2302, (1980)

[29] C. Boehme, dissertation, Philipps-Universität Marburg, 2002

[30] C. Boehme and K. Lips, Phys. Rev. B 68, 245105, (2003)

[31] Arthur Schweiger and Gunnar Jeschke, Principles of Pulse Electron Paramagnetic Resonance, Oxford University Press (2001)

[32] I. Hiromitsu, Y. Kaimori, M. Kitano, and T. Ito, Phys. Rev. B 59, 2151, (1999)

[33] D. Wu, Q. Y. Xu, F. M. Zhang, X. S. Liu, Y. W. Du, AAPPS Bulletin 18, No. 5, 52, (2008)

[34] S. Pramanik, C. G. Stefanita, S. Patibandla, S. Bandyopadhyay, K. Garre, N. Harth, and M. Cahay,Nature Nanotechnol. 2, 216, (2007)

[35] V. Dediu, M. Murgia ,F. C. Matacotta,C. Taliani, and S. Barbanera, Solid State Commun. 122, 181, (2002)

[36] Y. Araki, K. Maeda, H. Murai, Chem. Phys. Lett. 332, 515, (2000)

[37] V. R. Gorelik, K. Maeda, H. Yashiro, and H. Murai, J. Phys. Chem. A, 105, 8011, (2001)

[38] H. W. Kroto, J. R. Heath, S. C. O´Brian, R. F. Curl, and R. E. Smalley, Nature 318, 162, (1985)

[39] E. Osawa, Kagaku (Kyoto) 25 , 854, (1970)

[40] M. S. Dresselhaus, G. Dresselhaus, P. C. Eklund, Science of Fullerenes and Nanotubes, San Diego, Academic Press 1996

[41] T. L. Makarova, Semiconductors 35, 243, (2001)

[42] A. Hamed, Y. Y. Sun, Y. K. Tau, R. L. Meng, and P. H. Hor, Phys. Rev. B 47, 10873, (1993)

[43] R. W. Lof, M. A. van Veenendal, B. Koopmans, H. T. Jonkman, and G. A. Sawatzky, Phys. Rev. Lett. 68, 3924, (1992)

[44] W. Tress, diploma thesis, Universität Ulm, (2007)

[45] R. Könenkamp, G. Priebe, and B. Pietzak, Phys. Rev. B 60, 11804, (1999)

[46] I. Hiromitsu, M. Kitano, R. Shinto, and T. Ito, Synthetic Metals 121, 1539, (2001)

[47] M. M. Khaled, R. T.Carlin, P. C. Trulove, G. R. Eaton, S. S. Eaton, J. Am. Chem. Soc. 116, 3465, (1994)

[48] M. A. Greaney, S. M. J. Gorun, Phys. Chem. 95, 7142, (1991)

[49] J. Stinchcombe, A. Pénicaud, P. Bhyrappa, P. D. W. Boyd, C. A. Reed, J. Am. Chem. Soc. 115, 5212, (1993)

[50] J. Shinar, Z. V. Vardeny, Z. H. Kafafi, Optical and Electronic properties of Fullerenes and Fullerene-Based Materials, Marcel Dekker Inc. (2000)

[51] J. Partee, J. Shinar, P.A. Lane, X. Wei, and Z. V. Vardeny, Synth. Metals 86, 2305, (1997)

[52] Carlos A. Steren, Hans van Willigen , Marco Fanciulli, Chem. Phys. Lett. 245, 244, (1995)

[53] C. A. Reed and R. D. Bolskar, Chem. Rev. 100, 1075, (2000)

[54] A. Braun, J.Tcherniac, Berichte der Deutschen Chemischen Gesellschaft, 1907, 40, 2709

[55] R. P. Linstead, J. chem. soc., 1016, (1934)

[56] N. El Khatib, B. Boudjema, M. Maitrot, H. Chermette, and L. Porte, Can. J. chem. 66, 2313, (1988)

[57] J. M. Robertson, J. Chem. Soc., 615, (1935)

[58] M. Ashida, N. Uyeda, and E. Suito, J. Chryst. Growth 8, 45, (1971)

[59] H. Peisert, T. Schwieger, J. M. Auerhammer, M. Knupfer, M. S. Golden, J. Fink, P. R. Bressler and M. Mast, J. Appl. Phys. 90, 466, (2001)

[60] J. M. Assour, S. E. Harrison, J. Phys. Chem. Solids 26, 670, (1965)

[61] Kanemitsu Y., Yamamoto A., Funada H., Masumoto Y., J. Appl. Phys. 69, 7333 (1991)

[62] S. Siebentritt, Dissertation, Universität Hannover, (1992)

[63] W. Gao, A. Kahn, Organic Electronics 3, 53, (2002)

[64] J. Blochwitz, T. Fritz, M. Pfeiffer, K. Leo, D. M. Alloway, P. A. Lee, N. R. Armstrong, Organic Electronics 2, Iss 2, 97, (2001)

[65] H. R. Kerp, E. E. van Faassen, Chem. Phys. Lett. 332, 5, (2000)

[66] R. A. Collins, K. A. Mohammed, Thin Solid Films 145, 133, (1986)

[67] H. R. Kerp, E. E. van Faassen, Solar Energy Materials & Solar Cells 63, 15, (2000)

[68] G. D. Sharma, S. G. Sangodkar, and M. S. Roy, Materials Science and Engineering B41, 222, (1996)

[69] A. M. Saleh, A. O. Abu-Hilal, R. D. Gould, Current Applied Physics 3, 345, (2003)

[70] Mirko Vogel, dissertation, Freie Universität Berlin (2005)

[71] I. Hiromitsu, Y. Murakami, T. Ito, Sol. Stat. Commun. 119, 357, (2001)

[72] P. Peumans, A. Yakimov, S. R. Forrest, J. Appl. Phys. 93, 3693, (2003)

[73] R. O. Loutfy and J. H. Sharp, J. Chem. Phys. 71, 1211, (1979)

[74] J. W. Pankow, C. Arbour, J. P. Dodelet, G. E. Collins, and N. R. Armstrong, J. Phys. Chem. 97, 8485, (1993)

[75] A. Twarowski, J. Chem. Phys. 77, 5840, (1982)

[76] M. Martin, J. J. André, and J. Simon, J. Appl. Phys. 54, 2792, (1983)

[77] A. Opitz, M. Kraus, M. Bronner, J. Wagner, and W. Brütting, New J. Phys. 8, 065006, (2008)

[78] J. M. Assour and S. E. Harrison, J. Phys. Chem. 68, 872 (1964)

[79] J. B. Raynor, M. Robson, and A. S. M. Torrens-Burton, J. C. S. Dalton, 2360, (1977)

[80] J. R . Harbour and R. O. Loutfy, Phys. Chem. Solids 43, No. 6, 513, (1982)

[81] J. F. Boas, P. E. Fielding, and A. G. MacKay, Aust. J. Chem. 27, 7, (1974)

[82] H. J. Wagner, R. O. Loutfy, C. K. Hsiao, J. Mater. Sci. 17, 2781 (1982)

[83] C. M. Guzy, J. B. Raynor, L. P. Stodulski, and M. C. R. Symons, J. Chem. Soc. A, 997, (1969)

[84] P. Mu, T. Nakao, M. Handa, K. Kasuga, K. Sogabe, Bull. Chem. Soc. Jpn. 64, 3202 (1991)

[85] J. R. Harbour and M. J. Walzak, Langmuir 2, No. 6, 788, (1986)

[86] T. F. Yen, J. G. Erdman, Analytical Chem. 34, 694, (1962)

[87] D. J. G. Ingram and J. E. Bennett, J. Chem. Phys. 22, 1136, (1954)

[88] R. L. Sasseville, A. R. McIntosh, J. R. Bolton and J. R. Harbour, J. Phys. Chem. 88, 3139 (1984)

[89] T. C. A. Murphy, dissertation, Humboldt-Universität zu Berlin, (1996)

[90] S. G. Kukolich and D. R. Huffman, Chem. Phys. Lett. 182, 263, (1991)

[91] D. Meissner, S. Siebentritt, and S. Günster, Int. Symp. on Optical Materials Technol. for Energy Efficiency and Solar Energy Conversion XI, Toulouse, May 1992

[92] A. Sussman, J. Appl. phys. 38, 2738, (1967)

[93] A. K. Mahapatro, S. Ghosh, Appl. Phys. Lett. 80, 4840, (2002)

[94] F. R. Fan, L. R. Faulkner, J. Chem. Phys. 69, 3341, (1978)

[95] B. L. Sharma, Metal-Semiconductor Schottky Barrier Junctions and Their Applications, Plenum Press, New York (1984)

[96] F. R. Fan, L. R. Faulkner, J. Chem. Phys. 69, 3334, (1978)

[97] M. Castellani, I. Salzmann, P. Bugnon, S. Yu, M. Oehzelt, N. Koch, Appl Phys A 97, 1–9, (2009)

[98] B. P. Rand, J. Genoe, P. Heremans, and J. Poortmans, Prog. Photovolt: Res. Appl. 15, 659, (2007)

[99] S. M. Sze, Physics of Semiconductor Devices, John Wiley & Sons (1981)

[100] J. Antula, Phys. Lett. 25A, No. 4, 309, (1967)

[101] D. Gupta, M. Bag, and K.S. Narayan, Appl. Phys. Lett. 92, 093301-1, (2008)

[102] Y. Roussillon, V. G. Karpov, D. Shvydka, J. Drayton, and A. D. Compaan, J. Appl. Phys. 96, 7283, (2004)

[103] M. Glatthaar, M. Riede, N. Keegan, K. Sylvester-Hvid, B. Zimmermann, M. Niggemann, A. Hinsch, A. Gombert, Solar Energy Materials & Solar Cells 91, 390, (2007)

[104] A. J. Twarowski, J. Chem. Phys. 76, 2640, (1982)

[105] Jasprit Singh, Semiconductor Devices, John Wiley & Sons (2001)

[106] I. G. Hill, A. Kahn, Z. G. Soos, and R. A. Pascal, Jr., Chem. Phys. Lett. 327, 181, (2000)

[107] V. D. Mihailetchi, L. J. A. Koster, J. C. Hummelen, and P.W.M. Blom, Phys. Rev. Lett. 93, 216601, (2004)

[108] I. Solomon, Solid-St. Commun. 20, 215, (1976)

[109] K. Lips, and W. Fuhs, J. Appl. Phys. 74, 3993, (1993)

[110] A. Matsuyama, K. Maeda, and H. Murai, J. Phys. Chem. A 103, 4137, (1999)

[111] V. Dyakonov, N. Gauss, G. Rijsler, S. Karg, W. Rieß, M. Schwoerer, Chemical Physics 189, 687, (1994)

[112] G. H. Goudsmit, H. Paul, and A. I. Shushin, J. Phys. Chem. 97, 13243, (1993)

[113] T. Wimbauer, M. S. Brandt, M. W. Bayerl, N. M. Reinacher, and M. Stutzmann, Phys. Rev. B 58, 4892, (1998)

[114] G. B. Silva, L. F. Santos, R. M. Faria, C. F. O. Graeff, Mat. Res. Soc. Symp. Proc. Vol. 725, P4.18.1, (2002)

[115] C. G. Yang, E. Ehrenfreund, F. Wang, T. Drori, and Z. V. Vardeny, Phys. Rev. B 78, 205312, (2008)

[116] B. Hu, and Y. Wu, Nature Materials 6, 985, (2007)

[117] Ö. Mermer, G. Veeraraghavan, T. L. Francis, Y. Sheng, D. T. Nguyen, M. Wohlgenannt, A. Köhler, M. K. Al-Suti, and M. S. Khan, Phys. Rev. B 72,, 205202,

[118] J. D. Bergeson, V. N. Prigodin, D. M. Lincoln, and A. J. Epstein, Phys. Rev. Lett. 100, 067201, (2008)

[119] P. A. Bobbert, T. D. Nguyen, F.W. A. van Oost, B. Koopmans, and M. Wohlgenannt, Phys. Rev. Lett. 99, 216801 (2007)

[120] F. L. Bloom, W. Wagemans, M. Kemerink, and B. Koopmans, Phys. Rev. Lett. 99, 257201, (2007)

[121] T. D. Nguyen, Y. Sheng, J. E. Rybicki and M.Wohlgenannt, Sci. Technol. Adv. Mater. 9, 024206, (2008)

[122] T. D. Nguyen, Y. Sheng, J. Rybicki, and M. Wohlgenannt, Phys. Rev. B 77, 235209, (2008)

[123] P. Shakya, P. Desai, T. Kreouzis, W. P. Gillin, S. M. Tuladhar, A. M. Ballantyne and J. Nelson, J. Phys.: Condens. Matter 20, 452203, (2008)

[124] V.N. Prigodin, J.D. Bergeson, D.M. Lincoln, A.J. Epstein, Synthetic Metals 156, 757, (2006)

[125] N.S. Sariciftci, Progr. Quant. Electr. 19, 131 (1995)

[126] C.J. Brabec, N.S. Sariciftci, and J.C. Hummelen, Adv. Funct. Mater. 11, 15 (2001)

[127] M. Rusu, J. Strotmann, M. Vogel, M. Ch. Lux-Steiner, and K. Fostiropoulos, Appl. Phys. Lett. 90, 153511, (2007)

[128] A. Gliesche, C. Michel, V. Rajevac, K. Lips, D. Baranovskii, F. Gebhard, and C. Boehme, Phys. Rev. B 77, 245206 (2008)

[129] S. Saremi, diploma thesis, Freie Universität Berlin, (2008)